Aeroelastic Analyses of the SemiSpan SuperSonic Transport (S^{4}T) Wind Tunnel Model at Mach 0.95

Jiyoung Hur
Analytical Mechanics Associates, Inc., Hampton, Virginia

NASA STI Program . . . in Profile

Since its founding, NASA has been dedicated to the advancement of aeronautics and space science. The NASA scientific and technical information (STI) program plays a key part in helping NASA maintain this important role.

The NASA STI program operates under the auspices of the Agency Chief Information Officer. It collects, organizes, provides for archiving, and disseminates NASA's STI. The NASA STI program provides access to the NASA Aeronautics and Space Database and its public interface, the NASA Technical Report Server, thus providing one of the largest collections of aeronautical and space science STI in the world. Results are published in both non-NASA channels and by NASA in the NASA STI Report Series, which includes the following report types:

- TECHNICAL PUBLICATION. Reports of completed research or a major significant phase of research that present the results of NASA Programs and include extensive data or theoretical analysis. Includes compilations of significant scientific and technical data and information deemed to be of continuing reference value. NASA counterpart of peer-reviewed formal professional papers, but having less stringent limitations on manuscript length and extent of graphic presentations.

- TECHNICAL MEMORANDUM. Scientific and technical findings that are preliminary or of specialized interest, e.g., quick release reports, working papers, and bibliographies that contain minimal annotation. Does not contain extensive analysis.

- CONTRACTOR REPORT. Scientific and technical findings by NASA-sponsored contractors and grantees.

- CONFERENCE PUBLICATION. Collected papers from scientific and technical conferences, symposia, seminars, or other meetings sponsored or co-sponsored by NASA.

- SPECIAL PUBLICATION. Scientific, technical, or historical information from NASA programs, projects, and missions, often concerned with subjects having substantial public interest.

- TECHNICAL TRANSLATION. English-language translations of foreign scientific and technical material pertinent to NASA's mission.

Specialized services also include organizing and publishing research results, distributing specialized research announcements and feeds, providing information desk and personal search support, and enabling data exchange services.

For more information about the NASA STI program, see the following:

- Access the NASA STI program home page at *http://www.sti.nasa.gov*

- E-mail your question to help@sti.nasa.gov

- Fax your question to the NASA STI Information Desk at 443-757-5803

- Phone the NASA STI Information Desk at 443-757-5802

- Write to:
   STI Information Desk
   NASA Center for AeroSpace Information
   7115 Standard Drive
   Hanover, MD 21076-1320

Aeroelastic Analyses of the SemiSpan SuperSonic Transport (S^{4}T) Wind Tunnel Model at Mach 0.95

Jiyoung Hur
Analytical Mechanics Associates, Inc. Hampton, Virginia

Summary

Detailed aeroelastic analyses of the SemiSpan SuperSonic Transport (S^{4}T) wind tunnel model at Mach 0.95 with a 1.75° fixed angle of attack are presented. First, a numerical procedure using the Computational Fluids Laboratory 3-Dimensional (CFL3D) Version 6.4 flow solver is investigated. The mesh update method for structured multi-block grids was successfully applied to the Navier-Stokes simulations. Second, the steady aerodynamic analyses with a rigid structure of the S^{4}T wind tunnel model are reviewed in transonic flow. Third, the static analyses were performed for both the Euler and Navier-Stokes equations. Both the Euler and Navier-Stokes equations predicted a significant increase of lift forces, compared to the results from the rigid structure of the S^{4}T wind-tunnel model, over various dynamic pressures. Finally, dynamic aeroelastic analyses were performed to investigate the flutter condition of the S^{4}T wind tunnel model at the transonic Mach number. The condition of flutter was observed at a dynamic pressure of approximately 75.0-psf for the Navier-Stokes simulations. However, it was observed that the flutter condition occurred a dynamic pressure of approximately 47.27-psf for the Euler simulations. Also, the computational efficiency of the aeroelastic analyses for the S^{4}T wind tunnel model has been assessed.

Introduction

Two open-loop wind tunnel tests of the S^{4}T wind tunnel model [Reference 1] were conducted at the NASA Langley Research Center's Transonic Dynamics Tunnel (TDT) [References 2, 3]. Approximately 177 runs were attained to measure steady and unsteady characteristics ranging from Mach 0.6-1.2. In addition to the experimental study, one important element of this project was to support the research via nonlinear aeroelastic analysis by means of numerical method. Prior to the aeroelastic analyses, however, the aerodynamic performance of the S^{4}T wind tunnel model, with the assumption of a rigid structure, was also considered. The current investigations for the steady aerodynamics were focused on strong nonlinear effects at transonic conditions, which were intended to demonstrate using both the Euler and Navier-Stokes equations. One of goals from the steady aerodynamics study was to identify the most critical Mach numbers driving the flow physics about the S^{4}T configuration to strong nonlinearity, such as a sudden change of aerodynamic coefficients that occurs over the flow range of Mach 0.925-0.975. This nonlinearity is caused by the development of local shocks in the vicinity of lifting surfaces on the S^{4}T configuration. For example, the existence of a transonic shock at the lower surface of the inboard wing near the fuselage was observed. Also, the numerical study results show that the S^{4}T wind tunnel model experiences a rapid increase in drag force beyond Mach 0.925. Therefore, Mach 0.95 (in the critical range of Mach numbers where the transonic effect becomes more significant for the aeroelastic analyses of S^{4}T wind tunnel model) was selected for aeroelastic analyses in this work. The experimental data was also compared with the computational results at various angles of attack for Mach 0.95. The study includes the aerodynamic simulation results (at Mach 0.95) on a modified S^{4}T geometry (without engine nacelles), which was intended to reduce the complexity of the block topology in the structured grid. The reduced grid size and simplified model shape was purposed to minimize computational expenses and make the task of deforming the mesh to handle the aeroelastic simulations more efficient. However, the lift and drag produced by the modified S^{4}T geometry must be comparable with the results obtained from

the complete shape of the S^{4}T wind tunnel model in order to maintain the confidence in the accuracy of representing the aeroelastic system. Thus it is of interest to verify whether the simplified S^{4}T wind tunnel model will also produce valid aerodynamic forces, although it is expected that the differences in results between two shapes will be minor. The detailed results of the steady aerodynamic analyses, assuming a rigid structure of the S^{4}T wind tunnel model, are reviewed and summarized in this document.

The S^{4}T wind tunnel model is a flexible structure. When the assumption of rigid aircraft is no longer valid, it is typical to investigate the influence of aeroelastic effects as the aircraft deforms. One of the objectives in this work is to verify the performance of the S^{4}T wind tunnel model by performing static and dynamic aeroelastic analyses. For example, the solutions for aerodynamic variables due to the deformations must be carefully investigated and compared to the results from aerodynamic (rigid) calculations. The assessment of the aeroelastic influence on aircraft performance is a crucial design issue for aircraft manufacturers. This assessment impacts many design factors, such as the thrust-to-weight ratio, cruise range, loiter endurance, and Specific Fuel Consumption (SFC). The prediction of flutter speeds during the transonic regime of the S^{4}T wind tunnel model is of interest as well. In a general sense, the ability to predict the flutter speeds with accuracy is a crucial factor in establishing a TDT testing procedure, such as the operation of tunnel flows to meet the desired dynamic pressures associated with Mach numbers. It is favorable to generate the tunnel conditions as closely as possible to the flutter efficiently. Furthermore, it may not be recommendable to predict the flutter conditions by experimental methods due to the risk of catastrophic events (e.g., a model crash during testing). Therefore, the accurate determination of the dynamic characteristics of the S^{4}T wind tunnel model where flutter may occur, owing to computational methods, would be beneficial to the experimental study at TDT. One of the vital components in transonic flutter study is the analyses technique that utilizes Computational Fluids Dynamics (CFD). The CFD-based method for aeroelasticity has an advantage in that the approach deals with nonlinear flow physics. Furthermore, the aerodynamic nonlinearity can also be resolved efficiently by assuming that the tunnel flow condition is inviscid. From the hypothetical point of view, however, the assumption of no fluid viscosity may lead to erroneous flutter predictions at transonic speeds. For this reason, the use of linear methods is not encouraged for the transonic flow range. One of the constituents for computational aeroelastic analyses is the incorporation of structural dynamics into the nonlinear aerodynamic equations. Then, the integrated system combined by each governing equation needs to be solved simultaneously. The importance of time-accurate simulations (strongly coupled equations) may become more significant as the nonlinearity of flow physics becomes more evident. Also, the deforming mesh as the response of every time marching solution in structural dynamics is another key component for computational aeroelastic analyses. The usual practice of CFD-based aeroelastic analyses involves the construction of smooth CFD surfaces (for deforming aircraft shapes based on the structural solutions) and updating three-dimensional grids.

Often, the complexity of large-scale geometry associated with these applications causes difficulty maintaining grid quality. This is one of the issues degrading the efficiency of CFD-based aeroelastic analysis. For example, the current structured multi-block mesh for the S^{4}T wind tunnel model geometry (without engine nacelles) has a total of 73 grid blocks with over 4.6 million finite-volume cells for both inviscid and viscous flows. Although the computational efficiency of aeroelastic analyses using CFL3D Version 6.4 was greatly improved by employing the NASA Advanced Supercomputing (NAS) cluster [Reference 4], updating the deforming mesh is generally the most time-consuming procedure when aeroelastic calculations are carried out. It is important to examine how deforming grids of the S^{4}T wind tunnel model will affect the efficiency of the overall calculation cycles of static/dynamic aeroelastic

2

analyses, which may well also be beneficial to future applications. More importantly, the ultimate goal of this study is to provide a solid test bed of CFD-based aeroelastic simulations for the S^4T wind tunnel model with full confidence in the computational accuracy and within reasonable cost.

Wind Tunnel Model

The fully assembled shape of the S^4T wind tunnel model is illustrated in Figure 1, and a photo of the model, which was installed at the TDT, is shown in Figure 2. The measured geometry of the S^4T wind tunnel model, including inboard and outboard engines, is presented in Figures 3-5. As shown in Figures 3-5, this model is 197.89-in in length with a model span of 42.65-in and has the planform area of 1475.43-in^2. Thus the model has an aspect ratio of 2.46. The wing chord lengths are 81.92-in and 6.0-in at root and tip, respectively. It is intended that tunnel flow pass through the engines. The model span length includes the distance of the standoff geometry, which is 1.825-in measured from the wind tunnel sidewall. The standoff component was mounted between the vehicle symmetry plane and the tunnel sidewall [References 5, 6] in order to remove the effects of tunnel wall interference on the S^4T wind tunnel model due to the tunnel wall boundary layer. The structural layout of the S^4T wind tunnel model consists of an aeroelastically-scaled wing and flexible fuselage beam. The model has three active control surfaces (Ride Control Vane (RCV)), aileron, and horizontal tail) and a flexible fuselage beam attached to a rigid beam by spring-type nodal mounts. The flexible fuselage beam is located inside the fuselage fairing and only carries aerodynamic loads from the wing, RCV, and horizontal tail. The RCV and horizontal tail are all-moveable, rigid control surfaces attached to the flexible fuselage beam by a shaft allowing them to be rotated remotely via a piston-type actuator. The structural character of the S^4T wind tunnel model is illustrated in Figures 6-7. In Figure 7, the position of the model balance center (pitching moment center) is 125.8-in away from the nose cone. The overall description of the structural parts and layouts are well documented in Reference 1.

Methodology

Computational Aeroelasticity

The flow solver CFL3D has the capability of solving the Reynolds-Averaged Navier-Stokes (RANS) equations of aerodynamics using upwind finite volume method. The latest version of CFL3D Version 6.4 [References 7, 8] includes a new ability to perform aeroelastic analyses solving the coupled aerodynamics and linear structures equations in modal space. CFL3D Version 6.4 solves the aeroelastic system in a simultaneous manner by integrating each governing equation based on the state transition matrix solution. Furthermore, CFL3D Version 6.4 utilizes the Finite Macro-Element Mesh Deformation method, which was developed for a structured multi-block aeroelastic code as a robust and efficient mesh update procedure [Reference 7]. The method is intended to resolve the mesh movements when grids are highly compacted near the computational domain boundary.

One practice of aeroelastic analyses is to seek a static equilibrium state between aerodynamics and structural dynamics. The steady state between pressure load and structural deflections may be achieved efficiently by solving the steady state form of each governing equation and integrating each solution at an

iteration level. For the sake of generality, however, the static analyses of the S^{4}T wind tunnel model are performed in the same manner as the unsteady aeroelastic analyses as suggested by Reference 8. Thus the damping coefficients in the modal equations used for static aeroelastic analyses are defined to be artificially large in order to force convergence. Since accurate solutions are desired, an important task is how to determine the responses of structural modes and transmit the information to the aerodynamic system at the same time level. In other words, the inconsistency of the solutions due to the time lagging between aerodynamic and structural systems need to be removed. Thus CFL3D Version 6.4 applies the concept of a predictor and corrector scheme (accurate to the second order) to the time integration method that will synchronize the structural dynamics equations with unsteady aerodynamics. For dynamic aeroelastic analyses, the damping coefficient is set to a physically realistic value and the flutter onset computations are performed. The static aeroelastic solutions are used as initial conditions (restart solutions) for the dynamic aeroelastic solutions while perturbing modal velocities to excite the dynamic calculations. Then the time accurate aeroelastic calculations are carried out.

The choice of optimal time steps for the unsteady calculations in aeroelastic analyses is not straightforward due to the complexity of the mesh deformation procedure. As far as the maintenance of the grid quality is concerned, for example, a small time step is preferable to prevent a large amount of grid deformation between time steps. However, unreasonably small time steps may significantly reduce the efficiency of the simulations. Throughout this work, the non-dimensional time step of 4.096 was chosen as the optimal time step for the static/unsteady aeroelastic calculations. The selection of this particular time step has resulted after trying out various test runs. The physical time step corresponding to the non-dimensional time step is measured by a fraction of the speed of sound as explained in Reference 8. For example, the speed of sound in the TDT heavy gas (R-134a) test medium [References 9, 10, 11, 12] is 6441.71-in/sec. (536.79-ft/sec.) at a dynamic pressure of 45-psf for Mach 0.95. The equivalent physical time step to the non-dimensional parameter of 4.096 is 0.000636-sec, when the characteristic length of the S^{4}T wind tunnel model is defined as a unit inch.

The aeroelastic inputs utilized by CFL3D Version 6.4 are based on modal analysis of the S^{4}T wind tunnel model using MSC.Nastran [Reference 13]. The first ten natural frequencies were selected from the modal analysis to form the modal data. The structural and modal analyses were performed at the Aeroelasticity Branch, NASA Langley Research Center. The work at the Aeroelasticity Branch included the surface spline analysis to construct CFL3D Version 6.4 input data, which was employed to project the structural modes onto CFD surface grids of the S^{4}T wind tunnel model.

Mesh Deformation

The mesh deformation method implemented in CFL3D Version 6.4 seeks the finite element solution of a selected number of nodes (control points, or macro-element node points) from multi-block structured grids [References 7, 8]. The information on deforming macro-element node points is passed through all grid node points using an algebraic technique, such as Trans-Finite Interpolation (TFI). Thus the construction of the macro-element nodes is important for the Finite-Macro Mesh Deformation method. Although several choices are available for the macro-element nodes in CFL3D Version 6.4, the option for user defined control points for each grid block was applied to the mesh deformation scheme for aeroelastic analyses throughout this work. This option is desirable for manipulating the grid cells/blocks of interest. For example, in general, the volume cells are highly compacted near the grid block boundaries containing solid surfaces. Also, the grid blocks that contain the complex geometry are

4

particularly important in comparison to the blocks far from the solid surface geometry. However, more control points result in a more robust mesh update scheme with more expense in computational cost. The advantage of a mesh update scheme with an inviscid grid is greater computational efficiency due to the restively coarse grid near the solid surfaces. The trade off between accurate results and computational expense can be a crucial decision to be made.

Computational Modeling

The CFD surface mesh and structured multi-block grid topologies of the S^4T wind tunnel model near the symmetry plane are presented in Figures 8 and 9. The engine nacelles are omitted from the original shape of the S^4T wind tunnel model in Figure 9. The purpose of omitting the engine nacelles is to reduce the complexity of the geometry, since a continuous surface geometry is desired as much as possible. Figures 10-11 illustrate the computational domains wrapping the computational shapes of the S^4T wind tunnel model. For both Figure 10 and Figure 11, an h-type volume grid fills the space between the model surfaces and far-field boundaries, including symmetry plane. The outer boundaries of the computational domains in the figures stretched out as much as 5-10 times the model length. The cross-sectional area of the computational spaces in the figures is about 54 times lager than the test section area at TDT.

Free stream values are assigned in far-field boundary conditions except the out-flow boundary that extrapolates the values of the fluid variables from inside computational domain. The boundary conditions that utilize mirrored ghost cells are imposed to symmetry plane. No-slip condition is applied to the model surface meshes in Figures 8 and 9. When the boundary conditions for the original shape of the S^4T wind tunnel model are considered, however, special treatments of the boundary conditions at inlet and outlet of the engines are imposed [Reference 14]. For example, a pressure ratio is specified at the engine outlet, while inflow Mach number, the total pressure ratio, the total temperature ratio, and flow directions (angles) are specified at engine inlet. The reason is that the wind tunnel flow passes through the engines. The details of the surface grid of the engines, which emphasize the boundary conditions at inlet and out surfaces, are shown in Figure 12.

For both configurations (with and without engines), the coordinate system convention is based on the traditional right-handed coordinate system of the aircraft [Reference 14]. The positive direction of x-axis is identical to the free stream flow direction, and z-axis is perpendicular to the x-axis and positive pointing upward. Meanwhile, the direction of y-axis is positive toward the wing. The rotation of the S^4T wind tunnel model against the flow direction, using a shaft mounted on the tunnel wall (shown in Figure 7), generates the effect of an angle of attack. However, it is a prevalent exercise to manipulate the free stream flow velocity vector to represent the angle of attack in CFD applications. Therefore, the sign convention of the angle of attack follows the right-hand rule in the x-z plane when y-axis is outward along the span. Ignoring the sideslip angle (flow angle defined in x-y plane) effect, for example, the free stream flow direction with a 90°angle of attack will be in the positive z-axis direction [Reference 14].

Figures 8-12 present computational domains for viscous flow. It is noted that the grid topology in Figure 9 and Figure 11 resulted in a 27.7% reduction of grid quantities in blocks and cells, when the engine nacelles are dropped. The characters of inviscid grids for the S^4T wind tunnel model are same as the viscous grids, except that the impermeable wall boundary conditions on the computational surfaces of the model are imposed with coarse grid cells near the model surfaces. For viscous flow simulations, fully developed turbulent flow was assumed. Throughout this work, the Spalart-Allmaras turbulence modeling was employed to the Reynolds-averaged Navier-Stokes equations [Reference 14].

Computational Properties of Heavy Gas

Since the S^{4}T wind tunnel model operates in compressible flow, the changes in aerodynamic properties of the heavy gas (R-134a) due to compressibility are significant and greatly influence the dynamic stability. Thus the actual flutter speed at a selected Mach number (Mach 0.95 in this study) is very dependent on the compressibility of the gas. For this reason, the dynamic pressure is an important characteristic quantity that defines flutter conditions at TDT. It is important to make realistic assumptions of the aerodynamic operating condition in order to define typical CFL3D input parameters such as static temperature, flow speed, Prandtl number, specific heat ratio, or Reynolds number. Hence the properties of the R-134a for aeroelastic analyses have been calculated based on the open loop wind tunnel test data (TDT Test No. 600, January 2008). That is: Three sets of tunnel test conditions from Test No. 600 are available for Mach 0.95 for three dynamic pressures: 47.27, 51.24, and 61.23-psf. Linear interpolations of thermodynamic properties for the heavy gas were carried out to create heavy gas properties at desired dynamic pressures (especially for high dynamic pressures in order to perform the analyses beyond flutter margin, which may be rarely tried in tunnel testing). However, the ideal gas equations were implemented in order to obtain parameters such as the speed of sound, flow speed, and Reynolds number for a desired dynamic pressure. Thus the same Mach number is maintained. The key properties of the heavy gas and flow conditions for Mach 0.95 at various dynamic pressures, including wind tunnel demonstrated dynamic pressures, are summarized in Tables 1 and 2. The relationship of the flow speeds and dynamic pressures used in the aeroelastic analyses presented in this report is shown in Figure 13.

Results

The simulation cases depend on the structural flexibility of the S^{4}T wind tunnel model. For the rigid structure assumption, only steady aerodynamic modeling has been performed. The steady aerodynamics was evaluated over a range of Mach numbers at a 2º angle of attack and over a range of angles of attack at Mach 0.95. The sensitivity of angle of attack was also modeled with and without engines. Dynamic pressure is fixed for every case of steady aerodynamic simulations. On the other hand, the aeroelastic simulations have been performed with the flexible S^{4}T wind tunnel model shape (without engines). The cases for aeroelastic simulations have been carried out with a fixed Mach number and angle of attack over a range of dynamic pressures from 47.27-180-psf. The cases are summarized in Table 3.

Aerodynamics

Simulations of steady aerodynamics at various Mach numbers (0.3-1.5) were performed to investigate the influence of transonic flow on the S^{4}T wind tunnel model. The original configuration of the S^{4}T wind tunnel model with engine nacelles was applied to these simulations. The results in terms of aerodynamic coefficients, obtained using both the Euler and Navier-Stokes equations of aerodynamics, are presented in Figures 14 and 15. Figure 14 shows the plot for lift coefficient vs. Mach number, and the plot for drag coefficient vs. Mach number is shown in Figure 15. The results in Figures 14 and 15 were obtained with a 2° angle of attack. As the presented results implies, the significant influence of the transonic effect on the S^{4}T wind tunnel model is observed in the flow range of Mach 0.9-1.1.

Thus the aerodynamic performance of the modified S^4T wind tunnel model (without engines) was investigated at Mach 0.95. For Mach 0.95, Figures 16 and 17 present the results from Navier-Stokes simulations for lift and drag coefficients respectively for the range of angles of attack from -1.5° to 2.5°. The plot of lift/drag ratio is shown in Figure 18. The data resulting from the experimental study (Run No. 009 at TDT Test No. 600) are included in Figures 16-18 for reference. Figures 16-17 indicate that lift coefficient produced by the S^4T wind tunnel models with engine nacelles shows better agreement with experimental data, especially at the higher end of this angle of attack range. Meanwhile, the drag coefficient produced by model shape without engines has better agreement. Since lift is the dominant factor dictating an aeroelastic effect, the results shown in Figure 16 are of particular interest. It was observed that the wind tunnel testing produced greater lift than the CFD calculations. Also, there was a slight increase in the difference of the engine vs. no-engine modeling as angle of attack increased. The difference between wind tunnel testing data and computational results in lift coefficient was expected, since a rigid structure for the S^4T wind tunnel model was assumed in order to obtain the steady aerodynamic CFD. Furthermore, the fluctuation of the movable control surfaces (flap, horizontal tail, and RCV) with respect to deflection angles during tunnel testing affects the result (the difference in slope between experimental and computational data). In contrast, the positions of those control surfaces during the steady aerodynamic simulations (CFD calculations) remained fixed. For example, the higher flap deflections at lower angles of attack may have contributed to the larger increase in lift coefficients at the lower angles of attack (See Figure 19).

When the computationally obtained lift coefficients, as shown in Figure 16, are compared, the S^4T wind tunnel model without engine nacelles produces slightly less lift than the original shape. For further investigation, the wing profiles that form the basis of the pressure coefficient comparison were selected at inboard (before the engines), mid-span (between the engines), and outboard (after the engines) locations of the original model shape (with engines). The wing profiles are illustrated in Figure 20. Figures 21 and 22 present the pressure coefficient plots on the wing profiles of the models (with and without engines respectively) for different lateral positions along the span and an angle of attack of 2º. The lateral positions for the pressure coefficients and wing profiles in Figures 20-22 are at 8.5, 18.6, and 32.8-in. Even though the pressure coefficient of the lower profiles (especially at the lateral position of 18.6-in) is different, the overall difference in lift coefficient between shapes with and without engines is small.

Considering the rigid (un-deformed) wing profile shapes of the S^4T wind tunnel model shown in Figure 20, the profiles at inboard and mid-span wing portions exhibit relatively thick airfoil shapes with rounded leading edges. On the other hand, the profiles at outboard wing position become thinner toward the wing tip and have discontinuous leading edges. Also, the wing profiles tend to have nose-down shapes as the y-coordinate increases toward the wing tip, which shows the typical feature of washout in aerodynamic wing design. For example, in Figure 20, the angles of incidence defined by the angles between the extension of airfoil chord lines and longitudinal axis (x-axis) for inboard, mid-span, and outboard wing portions are -0.125º, -0.972º, and -1.804º respectively. The profiles of the horizontal tail and RCV have similar shapes as the profiles near the wing tip.

Static Aeroelastic Analyses

The static aeroelastic analyses of the S^4T wind tunnel model for Mach 0.95 were performed using both the Euler and Navier-Stokes equations. The structural damping factor of 0.999 was used in the modal equations. The calculations were performed with a fixed 1.75° angle of attack for the range of

dynamic pressures from 47.27-psf to 180.0-psf. The aerodynamic performance results of deforming the S^{4}T wind tunnel model are summarized in Table 4 and plotted in Figure 23, by showing the computed aerodynamic coefficients of lift. The static aeroelastic results from Euler equations and Navier-Stokes equations agree over this range of dynamic pressures.

As shown in Figure 23 and Table 4, lift coefficients show a tendency to increase as dynamic pressures increase. Also, the trend of lift coefficients using Euler equations is more linear than using Navier-Stokes equations. Furthermore, it is of interest to observe that the structurally flexible model shape, using both the Euler and Navier-Stokes equations, predict a significant increase of lift forces at each dynamic pressure, compared to the results from the structurally rigid shape of the S^{4}T wind-tunnel model.

In general, for a backward swept wing shape, it is expected that an aircraft having a flexible structure will experience the effect of aeroelastic washout and thus develop less lift force when a static aeroelastic equilibrium state is reached. For example, the loss of lift force due to a flexible wing may be severe in transonic flow ranges [Reference 15]. For the S^{4}T wind tunnel model, the deformed wing shape after the static aeroelastic calculations with Navier-Stokes equations have been examined, and the results are plotted in Figures 24-27. Figures 24-26 present the local angles of incidence at the selected lateral positions, such as 8.5, 18.6, and 32.8-in for inboard, mid-span, and outboard wing portions measured from the model symmetry line. As illustrated in Figure 26, it is verified that, for the flexible S^{4}T wind-tunnel model shape, a slight aeroelastic washout is observed as the y-coordinate increases toward the wing tip especially high dynamic pressures (greater than 60.0-psf). However, the structural wing torsion and bending contributed to the fairly large increase of local angles of incidence as the y-coordinate decreases toward the wing root, diminishing the aeroelastic washout effect, which are shown in Figures 24-25. It must be noted that wing root is permitted to move vertically as well as horizontally. The increase and decrease of local angles of incidence due to the aeroelastic wing bending and torsion with respect to rigid positions are compared and plotted in Figure 27. The results plotted in Figures 24-27 are summarized in Table 5. For the purpose of illustration, non-dimensional pressure contours on the S^{4}T wind tunnel model obtained by the static aeroelastic calculations at a dynamic pressure of 90.0-psf using the Navier-Stokes equations is presented in Figure 28. In Figure 28, the section surfaces for contours (in the x-z plane) cut the model shape through wing at 8.50, 18.6, and 32.8-in respectively (the same lateral positions in Figures 24-27). The pressure coefficient comparison plots for the rigid and aeroelastic wing shapes at the selected profiles, corresponding to the section surfaces shown in Figure 28, are presented in Figure 29-31.

In addition, pressure coefficient comparison plots for the RCV and horizontal tail are presented in Figures 32-33 respectively, and the location of the profiles are based on the section surface shown in Figure 28. The section surface grid for RCV and HT in Figure 28 cuts the model shape at 7.47 and 8.32-in respectively. Considering the overall deformed shape of the S^{4}T wind-tunnel model at a static aeroelastic equilibrium state, the computational results indicate that the wing and RCV are aeroelastically deflected upward while the horizontal tail is aeroelastically deflected downward, as is shown in Figure 34. The deformed shape shown in the figure was obtained by aeroelastic calculations at a dynamic pressure of 150.0-psf using the Navier-Stokes equations. Mach contours on the symmetry surface are also shown in the figure at a dynamic pressure of 150.0-psf, and the region of the local supersonic flow was emphasized.

Finally, the aeroelastic solutions in modal space were investigated, and the convergence of static aeroelastic analyses was examined. The non-dimensional time histories of generalized displacement for the first ten modes are presented in Figures 35-40 over selected dynamic pressures. The results of static analyses in Figures 35, 37, and 39 were obtained using the Navier-Stokes equations for dynamic pressures of 61.23-psf, 75.0-psf, and 90.0-psf, respectively. The results obtained using the Euler equations are

8

plotted in Figures 36, 38, and 40 for the same dynamic pressures. As shown in Figures 35-40, the displacements for the first mode using Navier-Stokes equations are larger than the same results using Euler equations. However, the displacements for the second and third modes using Euler equations are larger than the same results using Navier-Stokes equations. The residual histories for the Euler and Navier-Stokes solutions are plotted in Figures 41 and 42, respectively. The static aeroelastic calculations were started at iteration No. 10001 in the figures and carried out until the structural solutions of the generalized displacements were fully stabilized.

Dynamic Aeroelastic Analyses

Once the static analyses are performed, it is straightforward to carry out the dynamic analyses. The dynamic analysis procedures were the same as for the static analysis, except that a damping factor 0.005, which is equivalent to a structural damping of 1.0%, was assumed for the S^4T wind tunnel model. The static aeroelastic solutions were used as the initial conditions for the dynamic calculations, and a perturbing modal velocity (non-dimensional) of 0.1 was set in every mode to excite the dynamic calculations. Thus the current interest is to determine the flow condition at which flutter may occur at Mach 0.95 with a fixed 1.75° angle of attack.

The discussion of the dynamic calculations is based on the time histories of the solutions of the structural dynamic equations in modal space. Hence the first three modes, having lower natural frequencies, were selected for discussion. Figure 43 shows the time histories of the generalized displacement for the first mode at various dynamic pressures (47.27-120.0-psf) using the Navier-Stokes equations. The physical durations for the 47.27, 61.23, and 75.0-psf dynamic pressure cases in Figure 43 were approximately 5.22-sec. This duration includes the static analyses, which is approximately 0.77-sec. Similar results for the second mode are presented in Figures 44. The time histories for the third mode are presented in Figure 45. The investigation of the time histories of aeroelastic solutions using Navier-Stokes equations, presented in Figures 43-45 over numerous dynamic pressures and modes, indicates that flutter may occur near a dynamic pressure of 75.0-psf at Mach 0.95 with a fixed 1.75° angle of attack (a slight dynamic instability is observed at this dynamic pressure). However, a neutral stability of the solutions was observed at a dynamic pressure of 47.27-psf using the Euler equations. The comparison of the time histories of generalized displacement (for the first mode) at a dynamic pressure 61.23-psf for the Euler and Navier-Stokes simulations are shown in Figure 46. The aeroelastic solution exhibits dynamic instability with Euler equations and stability with Navier-Stokes equations in the figure.

Computational Time Assessment

The major factor that drives the computational cost is the frequency that the deforming mesh is updated. Also, it is of interest to investigate the trend of computational cost with respect to analysis methodology, especially when the mesh deforms. Figure 47 summarizes the results of consumed computational time (wall-clock time usage) for static aeroelastic analyses using both Euler and Navier-Stokes equations. The computational usage for steady aerodynamic simulations with rigid model shapes was included in the figure. The computational time usage for static aeroelastic analyses in Figure 47 are based on the duration (non-dimensional) of 5038.08 until the fully converged solutions of structural displacement are achieved as illustrated in Figures 35-40. In Figure 47, it is observed that the computational cost of aeroelastic simulations for viscous flow grew as the dynamic pressures increased.

9

Meanwhile, the result from simulations for inviscid flow shows a steady behavior in computational time usage, although larger mesh deformations are permitted as the dynamic pressures increased. The same topology of macro-element nodes (user specified control points, Reference [8]) has been applied to the mesh update scheme for both inviscid and viscous grids. The comparison of computational usage for dynamic calculations and static calculations is plotted in Figure 48. In Figure 48, the computational time is expressed as wall-clock hours per unsteady iteration. Referring to Figure 46, for example, the wall-clock duration to perform 7270 dynamic cycles (29777.92 in non-dimensional duration with a time-step size of 4.096, which is equivalent to approximately 4.45-sec in wind tunnel duration) at a dynamic pressure of 61.23-psf are 151.12 hours and 130.09 hours for inviscid flow and viscous flow, respectively. Thus the values of computational time per dynamic cycle yield 0.0208 and 0.0179.

Concluding Remarks

A computational study was performed employing CFL3D Version 6.4 for steady aerodynamic and static/dynamic aeroelastic analyses of the S^{4}T wind tunnel model. This study focused on the transonic regime with a heavy gas as the test medium. The transonic nonlinearity was demonstrated, regarding to aerodynamic coefficients, using the rigid shape of the S^{4}T wind tunnel model across Mach numbers. Steady aerodynamic calculations were carried out for Mach 0.95 at various angles of attack, and the results were investigated using the experimental data at TDT. The expectation was that the complexity of flow physics at transonic flow speeds would have an influence on the aeroelastic performance and dynamic stability of the S^{4}T wind tunnel model.

Numerous results of static and dynamic aeroelastic analyses were obtained and investigated at a transonic Mach number of 0.95 with a 1.75° angle of attack using both the Euler and Navier-Stokes equations. The lift coefficients show a tendency to increase as the S^{4}T wind tunnel model deforms in shape with increasing dynamic pressure. Both results showed good agreement in terms of lift coefficient over various dynamic pressures for static aeroelastic analyses. Since Euler equations are intended to solve nonlinear aerodynamics, and have the advantage of computational efficiency over Navier-Stokes equations, the use of Euler equations in static aeroelasticity may be attracted. Concerning the flutter, however, it has been demonstrated that the selection of the aerodynamic methodology is critical in dynamic analyses. The dynamic aeroelastic solutions using the Euler equations showed a tendency to diverge at unrealistically low dynamic pressures.

One of the contributions of this work was that the Finite Macro-Element Mesh Deformation method was successfully applied to the deformation of the three-dimensional grids of the S^{4}T wind tunnel model, particularly for the Navier-Stokes aeroelastic analyses.

Acknowledgements

References

1. Perry, B. III., Silva, W., Florance, J., Wieseman, C., Pototzky, A., Sanetrik, M., Scott, R., Keller, D., Cole, S., and Coulson, D.: "Plans and Status of Wind tunnel Testing Employing an Aeroservoelastic Semispan Model," AIAA 2007-1770, presented at the 48th AIAA/ASME/ASCE/AHS/ASC Structures, Structural Dynamics, and Materials Conference, Honolulu, Hawaii, April 23-26, 2007.
2. Perry, B. III., Noll, T., and Scott, R.: "Contributions of the Transonic Dynamics Tunnel to the Testing of Active Control of Aeroelastic Response," AIAA 2000-1769, presented at the 41st AIAA/ASME/ASCE/AHS/ASC Structures, Structural Dynamics, and Materials Conference and Exhibit, Atlanta, GA, April 3-6, 2000.
3. Cole, S., Noll, T., and Perry, B. III., "Transonic Dynamics Tunnel Aeroelastic Testing in Support of Aircraft Development," *Journal of Aircraft*, Volume 40, Number 5, September-October 2003.
4. Saini, S., Talcott D., Jespersen, D., Djomehri, J., Jin H., and Biswas, R., "Scientific Application-Based Performance Comparison of SGI Altix 4700, IBM POWER5+, and SGI ICE 8200 Supercomputers," NAS Technical Report NAS-09-001, February 2009.
5. Gatlin, G. M., and McGhee, R. J., "Study of Semi-Span Model Testing Techniques," AIAA 96-2386, presented at 14th Applied Aerodynamics Conference, New Orleans, LA, June17-20, 1996.
6. Ghaffari, F., Biedron, R. T., and Luckring J. M., "Numerical Viscous Flow Analysis of an Advanced Semispan Diamond-Wing Model at High-Lift Conditions," AIAA 2002-0846, presented at 40th AIAA Aerospace Sciences Meeting & Exhibit Reno, Nevada, January 14-17, 2002.
7. Bartels, R. E., Rumsey, C., and Biedron, R., "Finite Macro-Element Mesh Deformation in a Structured Multi-Block Navier-Stokes Code, " NASA/TM-2005-213789, July 2005.
8. Bartels, R. E., Rumsey, C. L., and Biedron, R., "CFL3D Version 6.4—General Usage and Aeroelastic Analysis," NASA/TM-2006-214301, April 2006.
9. Cole, S. R., and Rivera, J. A., Jr., "The New Heavy Gas Testing Capability in the NASA Langley Transonic Dynamic Tunnel," Paper No. 4, presented at the Royal Aeronautical Society Wind Tunnels and Wind Tunnel Test Techniques Forum, Churchill College, Cambridge, UK, April 14-16, 1997.
10. Anders, J. B., Anderson, W. K., and Murthy, A. V., "The Use of Heavy Gas for Increased Reynolds Numbers in Transonic Wind Tunnels," AIAA 98-2882, presented at 20th AIAA Advanced Measurement and Ground Testing Technology Conference, Albuquerque, NM, June 15-18, 1998.
11. Corliss, J. M., and Cole, S. R., "Heavy Gas Conversion of the NASA Langley Transonic Dynamics Tunnel," AIAA 98-2710, presented at 20th AIAA Advanced Measurement and Ground Testing Technology Conference, Albuquerque, NM, June 15-18, 1998.
12. Cole, S. R., and Garcia, J. L., "Past, Present and Future Capabilities of the Langley Transonic Dynamics Tunnel from an Aeroelasticity Perspective," AIAA 2000-1767, presented at AIAA Dynamics Specialists Conference, Atlanta, GA, April 5-6, 2000.
13. MSC Software Corporation, "Dynamic Analysis User's Guide: MSC Nastran 2012," Version 2012, MSC Software 2011.
14. Krist, S. L., Biedron, R. T., and Rumsey, C. L, "User's M Manual (Version 5.0)," NASA/TM-1998-20844, June 1998.
15. Newman. J. C., III, Newman, P. A., Taylor, A. C., III, and Hou, G. J.-W., "Efficient nonlinear static aeroelastic wing analysis," *Computers and Fluids*, Volume 28, Number 4, pp. 615-628(14), May 1999.

Dynamic Pressure	Heavy Gas Properties				
	Density	Viscosity	Temperature	Pressure	Prandtl No.
q	ρ_∞	μ_∞	T_∞	p_∞	P_r
psf (lbf/ft^2)	slug/ft^3	slug/(ft·sec)	°F	psf (lbf/ft^2)	–
45.00	0.3479e-03	0.2417e-06	46.4018	89.6881	0.69828
47.27	**0.3624e-03**	**0.2423e-06**	**47.2732**	**94.1179**	**0.69760**
51.24	**0.3877e-03**	**0.2434e-06**	**48.7931**	**101.8446**	**0.69641**
60.00	0.4437e-03	0.2458e-06	52.1517	118.9190	0.69377
61.23	**0.4516E-03**	**0.2461e-06**	**52.6225**	**121.3124**	**0.69340**
75.00	0.5396e-03	0.2499e-06	57.9016	148.1499	0.68926
90.00	0.6355e-03	0.2539e-06	63.6514	177.3808	0.68474
105.00	0.7314e-03	0.2580e-06	69.4013	206.6117	0.68023
120.00	0.8273e-03	0.2621e-06	75.1512	235.8427	0.67571
135.00	0.9231e-03	0.2662e-06	80.9011	265.0736	0.67120
150.00	0.1019e-02	0.2703e-06	86.6509	294.3045	0.66668
165.00	0.1115e-02	0.2744e-06	92.4008	323.5354	0.66217
180.00	0.1211e-02	0.2784e-06	98.1507	352.7663	0.65765

Table 1. Heavy gas R134a properties over various dynamic pressures at the pre-assigned Mach number of 0.95. Wind tunnel conditions for Test No. 600 runs at TDT are indicated in bold characters.

Dynamic Pressure	Heavy Gas Properties				
	Reynolds No.	Specific-heat Ratio	Speed of Sound	Flow Speed	Mach No.
q	Re_L[1]	γ	a_∞	U_∞	M_∞
psf (lbf/ft^2)	–	–	ft/sec	ft/sec	–
45.00	0.06101	1.11760	536.7860	508.6428	0.94757
47.27	**0.06366**	**1.11810**	**538.8679**	**510.7736**	**0.94786**
51.24	**0.06825**	**1.11898**	**542.1353**	**514.0902**	**0.94827**
60.00	0.07825	1.12093	548.0818	520.0220	0.94880
61.23	**0.07963**	**1.12120**	**548.8039**	**520.7314**	**0.94885**
75.00	0.09489	1.12426	555.5668	527.2274	0.94899
90.00	0.11099	1.12759	561.0073	532.2008	0.94865
105.00	0.12658	1.13092	565.2234	535.8407	0.94802
120.00	0.14167	1.13426	568.6481	538.6201	0.94719
135.00	0.15630	1.13759	571.5315	540.8120	0.94625
150.00	0.17048	1.14092	574.0281	542.5850	0.94522
165.00	0.18424	1.14425	576.2388	544.0486	0.94414
180.00	0.19759	1.14758	578.2320	545.2774	0.94301

Table 2. Flow conditions for the heavy gas R134a properties over various dynamic pressures at the pre-assigned Mach number of 0.95. Wind tunnel conditions for Test No. 600 runs at TDT are indicated in bold characters.

[1] The value implies Reynolds number per a million with characteristic length of 1/12-ft in as one of the CFL3D Version 6.4 input parameters.

Methodology	Flow	Mach No.	Angle of Attack (º)	Dynamic Pressure (psf)	Model Shape
Steady Aerodynamics (Rigid Structure)	Inviscid	0.3-1.5 (18 Cases)	2.0	47.27	With engines
	Viscous				
	Viscous	0.95	-1.5-2.5 (8 Cases)	47.27	With engines
					No engines
Static Aeroelasticity	Inviscid	0.95	1.75	47.27-180.0 (10 Cases)	No engines
	Viscous			47.27-165.0 (9 Cases)	
Dynamic Aeroelasticity	Inviscid	0.95	1.75	47.27-75.0 (3 Cases)	
	Viscous			47.27-120.0 (6 Cases)	

Table 3. The matrix of simulation cases for the S[4]T wind tunnel model using CFL3D version 6.4.

Dynamic Pressure	Flow Speed	Computational Methodology			
		Rigid		Static Aeroelastic	
q (psf)	U_∞ (in/sec)	Inviscid Flow	Viscous Flow	Inviscid Flow	Viscous Flow
47.27	6129.2827	0.9002e-02	0.9094e-02	0.1605e-01	0.1615e-01
61.23	6248.7770	0.8914e-02	0.9919e-02	0.1795e-01	0.1858e-01
75.00	6326.7291	0.8936e-02	0.1064e-01	0.1982e-01	0.2055e-01
90.00	6386.4098	0.8957e-02	0.1109e-01	0.2182e-01	0.2236e-01
105.00	6430.0880	0.9008e-02	0.1140e-01	0.2377e-01	0.2400e-01
120.00	6463.4412	0.9064e-02	0.1163e-01	0.2568e-01	0.2554e-01
135.00	6489.7444	0.9127e-02	0.1181e-01	0.2755e-01	0.2707e-01
150.00	6511.0198	0.9203e-02	0.1194e-01	0.2938e-01	0.2857e-01
165.00	6528.5834	0.9276e-02	0.1204e-01	0.3116e-01	0.2990e-01
180.00	6543.3289	0.9345e-02	0.1212e-01	0.3289e-01	–

Table 4. Lift coefficients computed by static aeroelastic analyses over various dynamic pressures for Mach 0.95 with a 1.75° angle of attack.

Dynamic Pressure	Incidence Angle (°)					
	Inboard (y=8.5-in)		Mid-span (y=18.6-in)		Outboard (y=32.8-in)	
q (psf)	Rigid	Flexible	Rigid	Flexible	Rigid	Flexible
47.27	-0.12465	-0.03088	-0.97179	-0.87180	-1.80392	-1.79599
61.23	-0.12465	-0.00624	-0.97179	-0.84800	-1.80392	-1.80580
75.00	-0.12465	0.01755	-0.97179	-0.82505	-1.80392	-1.81564
90.00	-0.12465	0.04324	-0.97179	-0.79978	-1.80392	-1.82498
105.00	-0.12465	0.06869	-0.97179	-0.77424	-1.80392	-1.83302
120.00	-0.12465	0.09388	-0.97179	-0.74851	-1.80392	-1.84008
135.00	-0.12465	0.11892	-0.97179	-0.72261	-1.80392	-1.84646
150.00	-0.12465	0.14331	-0.97179	-0.69713	-1.80392	-1.85274
165.00	-0.12465	0.16730	-0.97179	-0.67172	-1.80392	-1.85849
180.00	-0.12465	–	-0.97179	–	-1.80392	–

Table 5. The local angles of incidence for inboard, mid-span, and outboard wing portions (about 8.5, 18.6, and 32.8-in of y-positions) resulted from static aeroelastic analyses about viscous flow over various dynamic pressures.
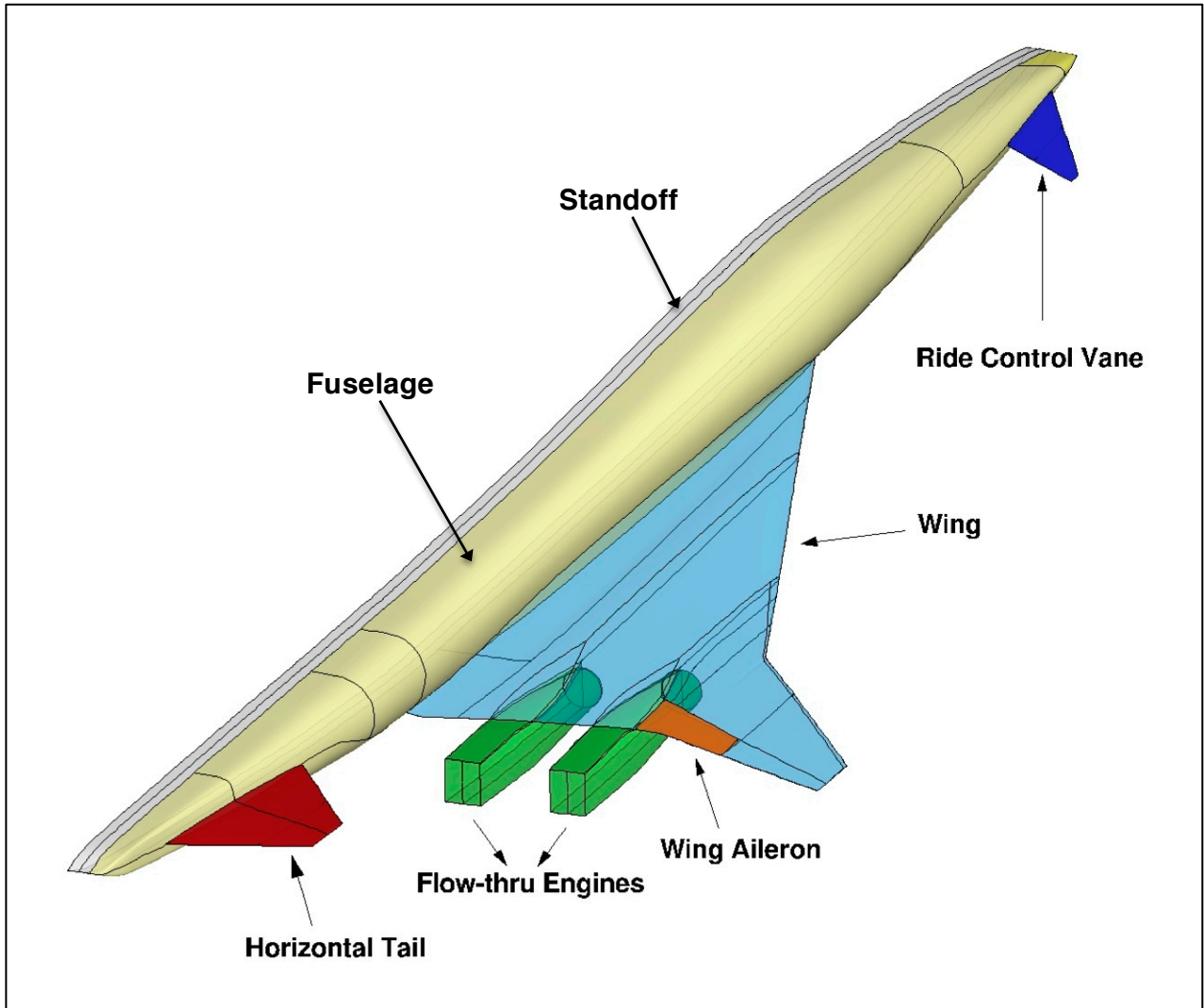
Figure 1. The illustration of <u>S</u>emi<u>S</u>pan <u>S</u>uper<u>S</u>onic <u>T</u>ransport (S⁴T) wind-tunnel model.

Figure 2. The $\underline{S}$emi$\underline{S}$pan $\underline{S}$uper$\underline{S}$onic $\underline{T}$ransport (S^{4}T) wind-tunnel model installed at the NASA Langley Research Center's $\underline{T}$ransonic $\underline{D}$ynamics $\underline{T}$unnel (TDT).
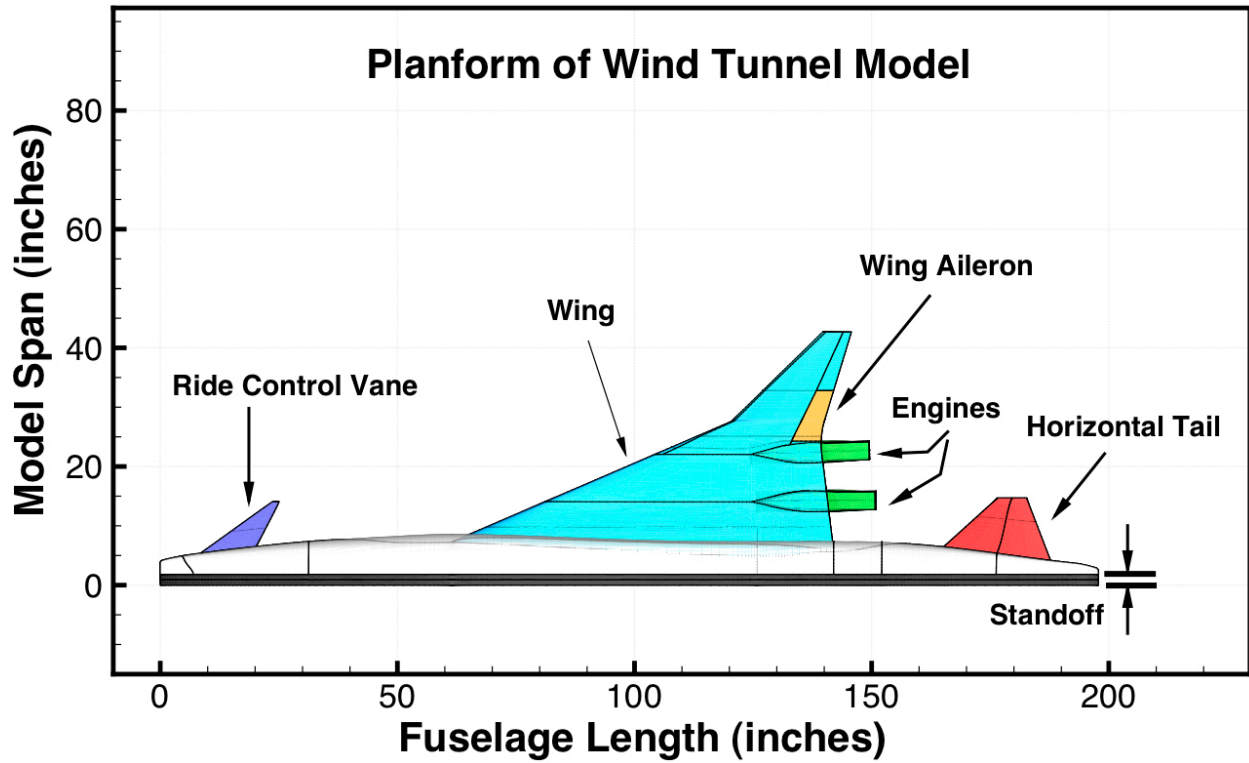
Figure 3. The top view of SemiSpan SuperSonic Transport (S[4]T) wind-tunnel model.

Figure 4. The rear view of SemiSpan SuperSonic Transport (S⁴T) wind-tunnel model.
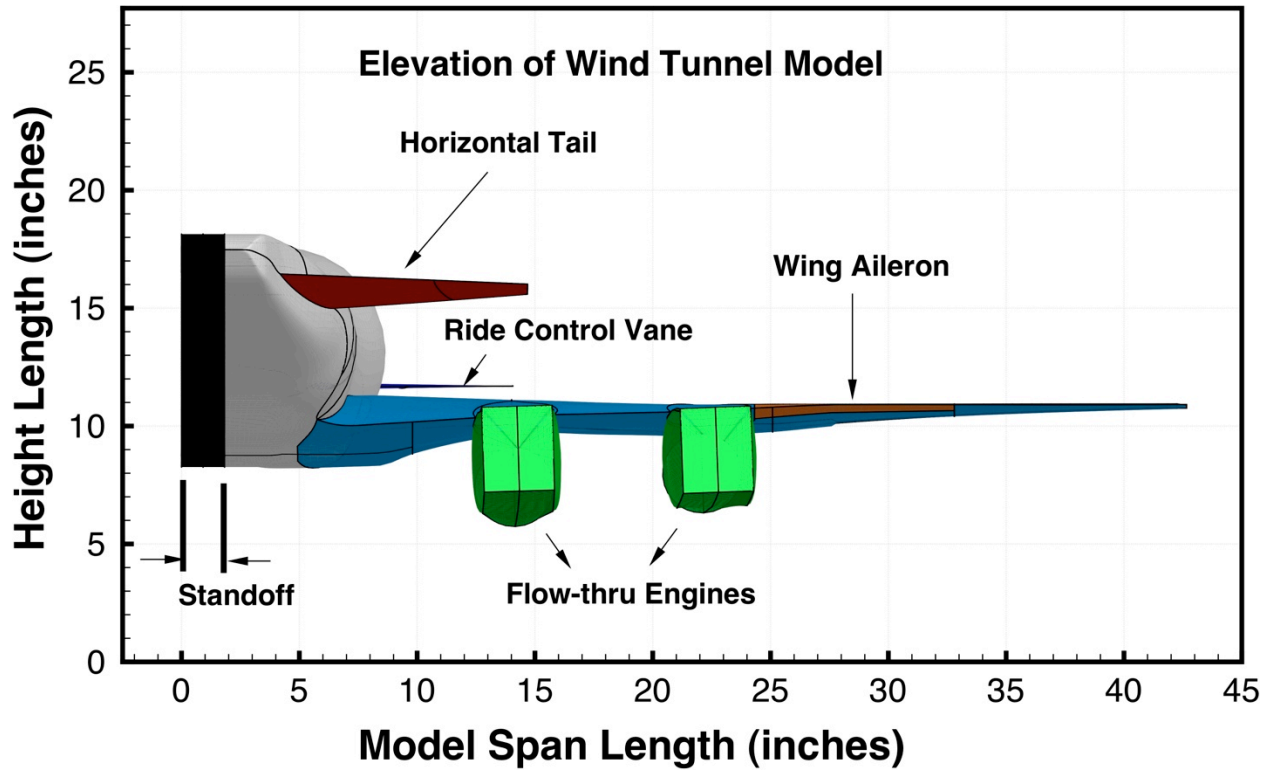
Figure 4. The rear view of $\underline{S}$emi$\underline{S}$pan $\underline{S}$uper$\underline{S}$onic $\underline{T}$ransport (S^{4}T) wind-tunnel model.
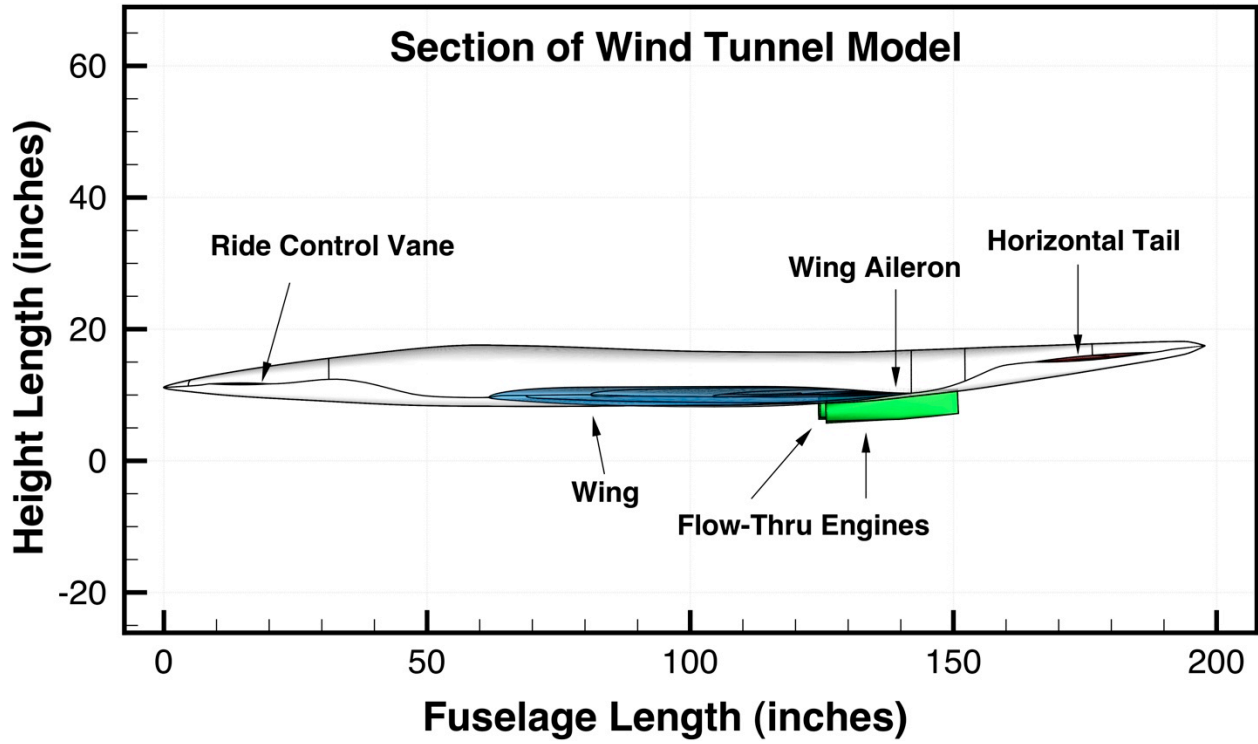
Figure 5. The side view of <u>S</u>emi<u>S</u>pan <u>S</u>uper<u>S</u>onic <u>T</u>ransport (S⁴T) wind-tunnel model.

Figure 6. Photo of S^{4}T wind-tunnel model without fuselage faring.
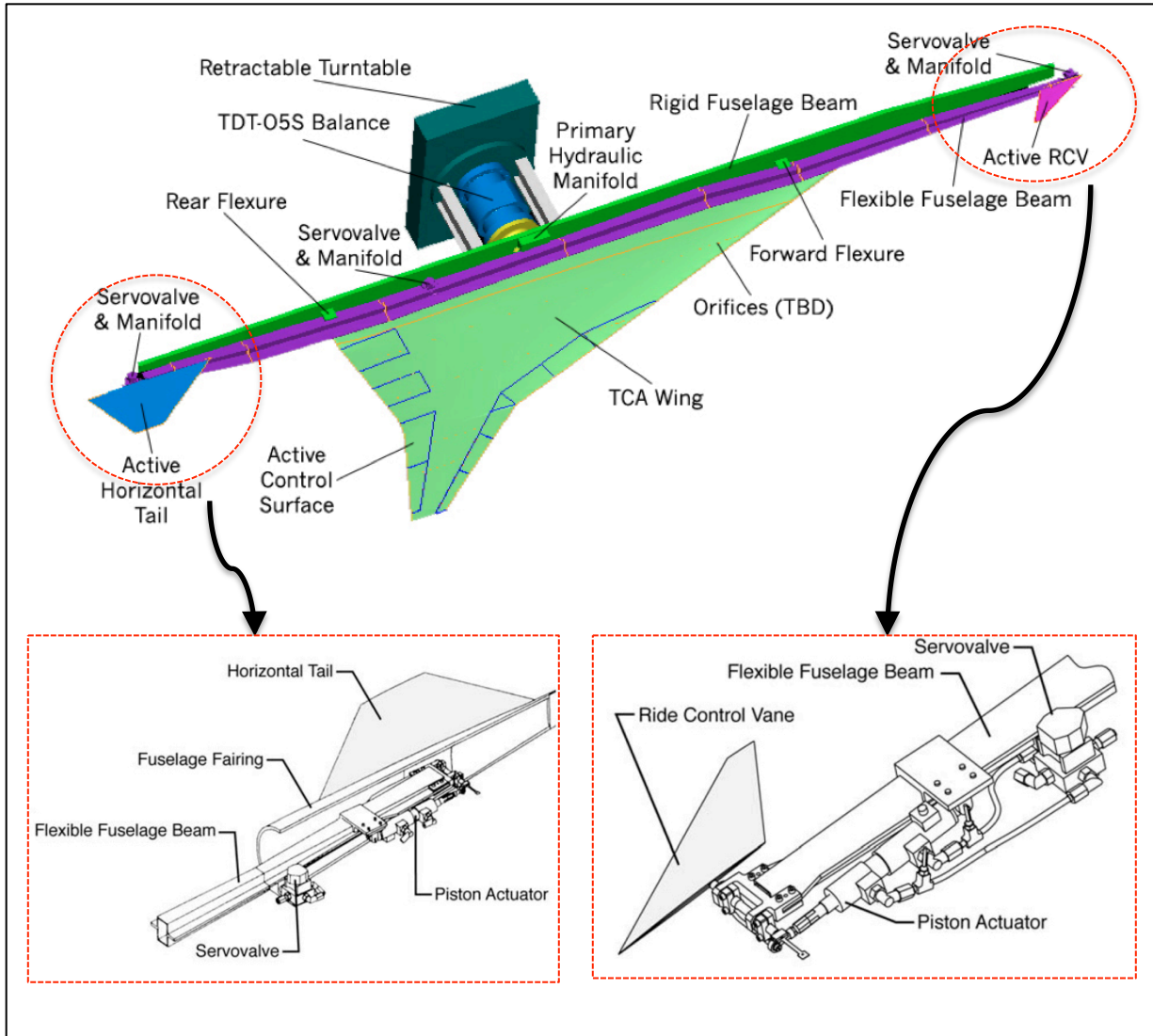
Figure 7. Drawing of S^{4}T wind-tunnel model without fuselage faring.
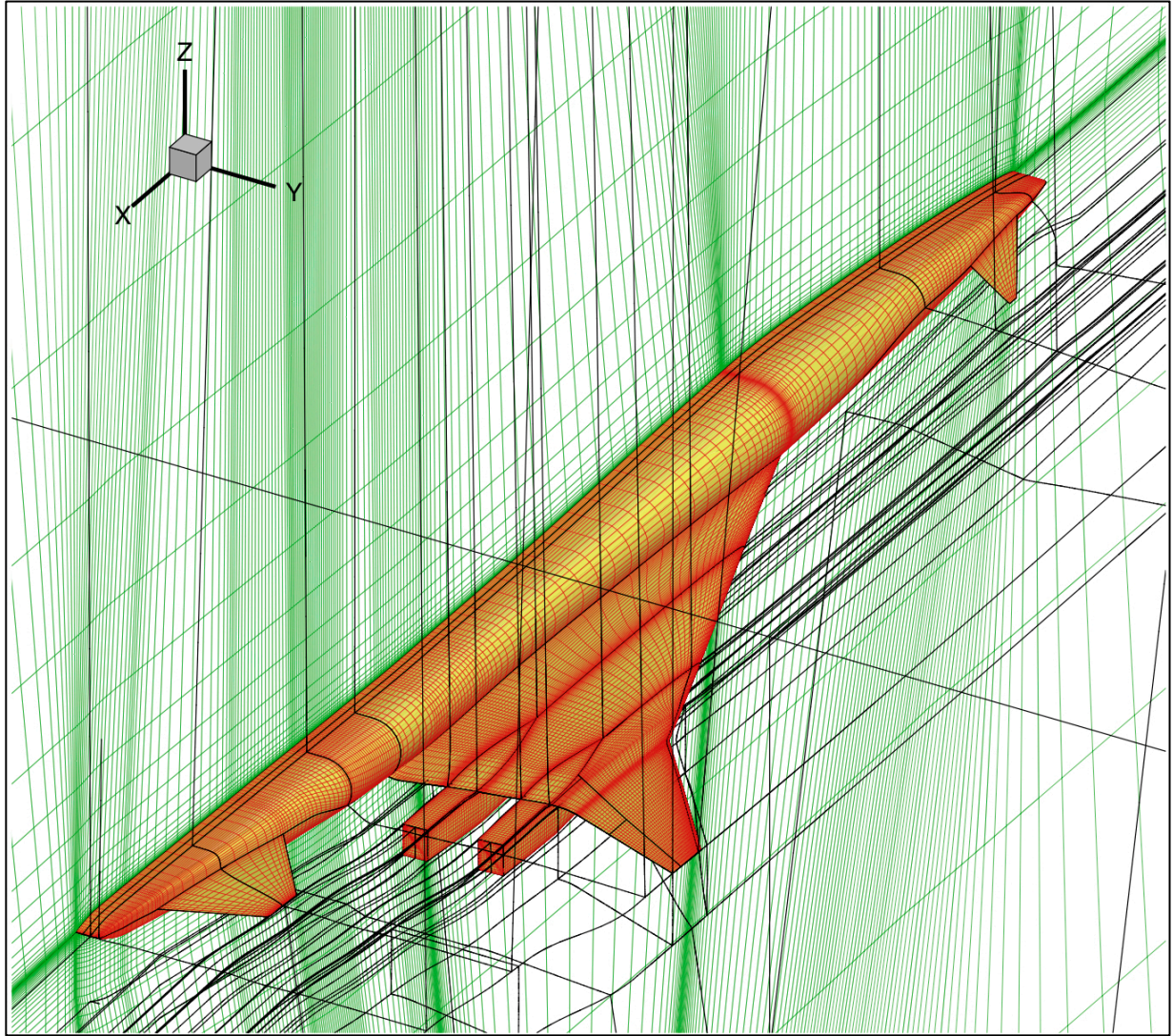
Figure 8.   CFD surface mesh and structured multi-block grid topologies corresponding to the geometry of the S^4T wind tunnel model with engine nacelles (viscous grid with a total of 101 grid blocks).
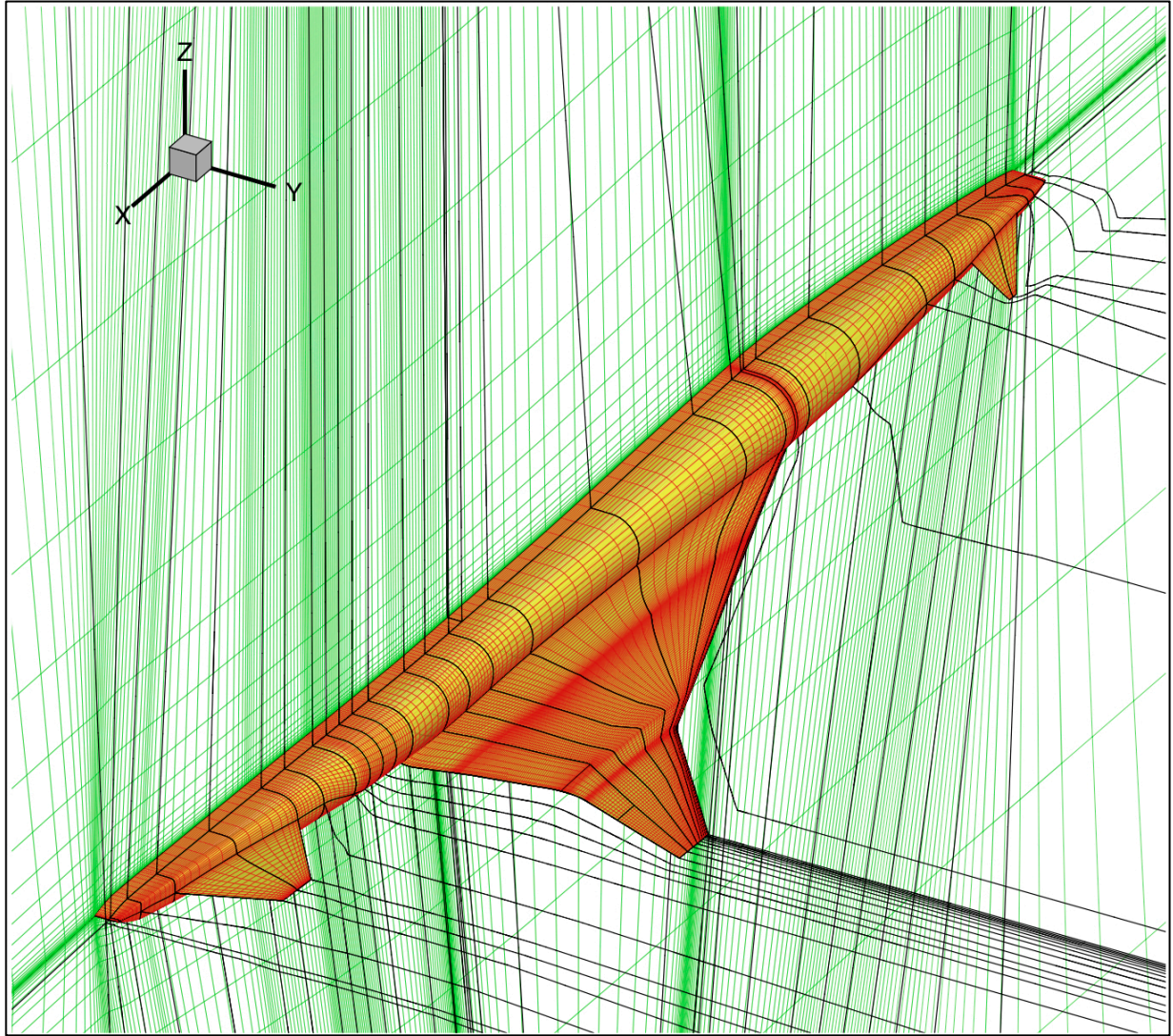
Figure 9.   CFD surface mesh and structured multi-block grid topologies corresponding to the geometry of the S^4T wind tunnel model without engine nacelles (viscous grid with a total of 73 grid blocks).

Grid Quantities

Blocks	101
Nodes	7095585
Cells	6414848

Wind Tunnel Flow Direction

1000 inches

2198 inches

2000 inches
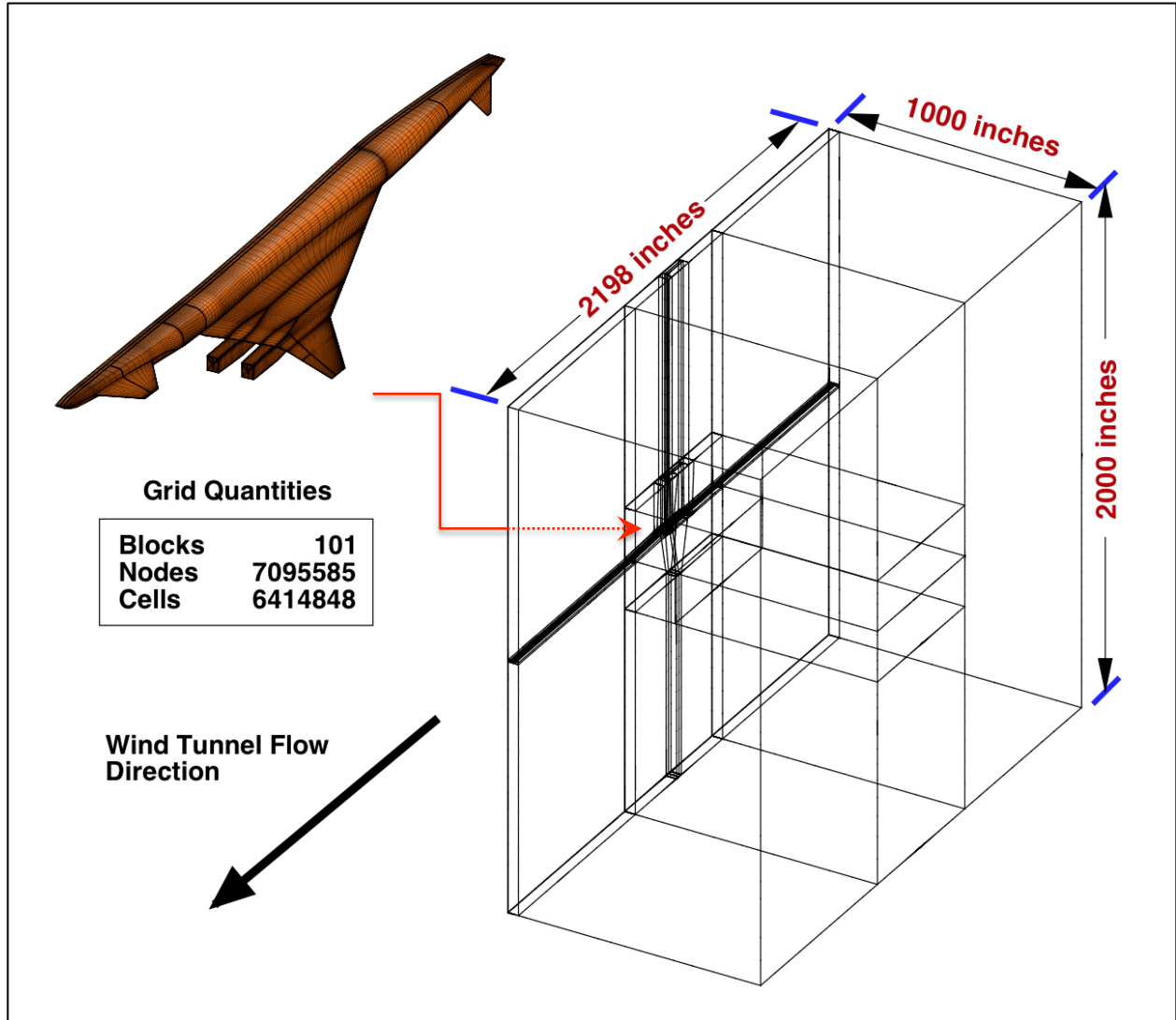
Figure 10. Structured multi-block grid topologies of the computational domain for the geometry of the S^{4}T wind tunnel model with engine nacelles (viscous grid with a total of 101 grid blocks).
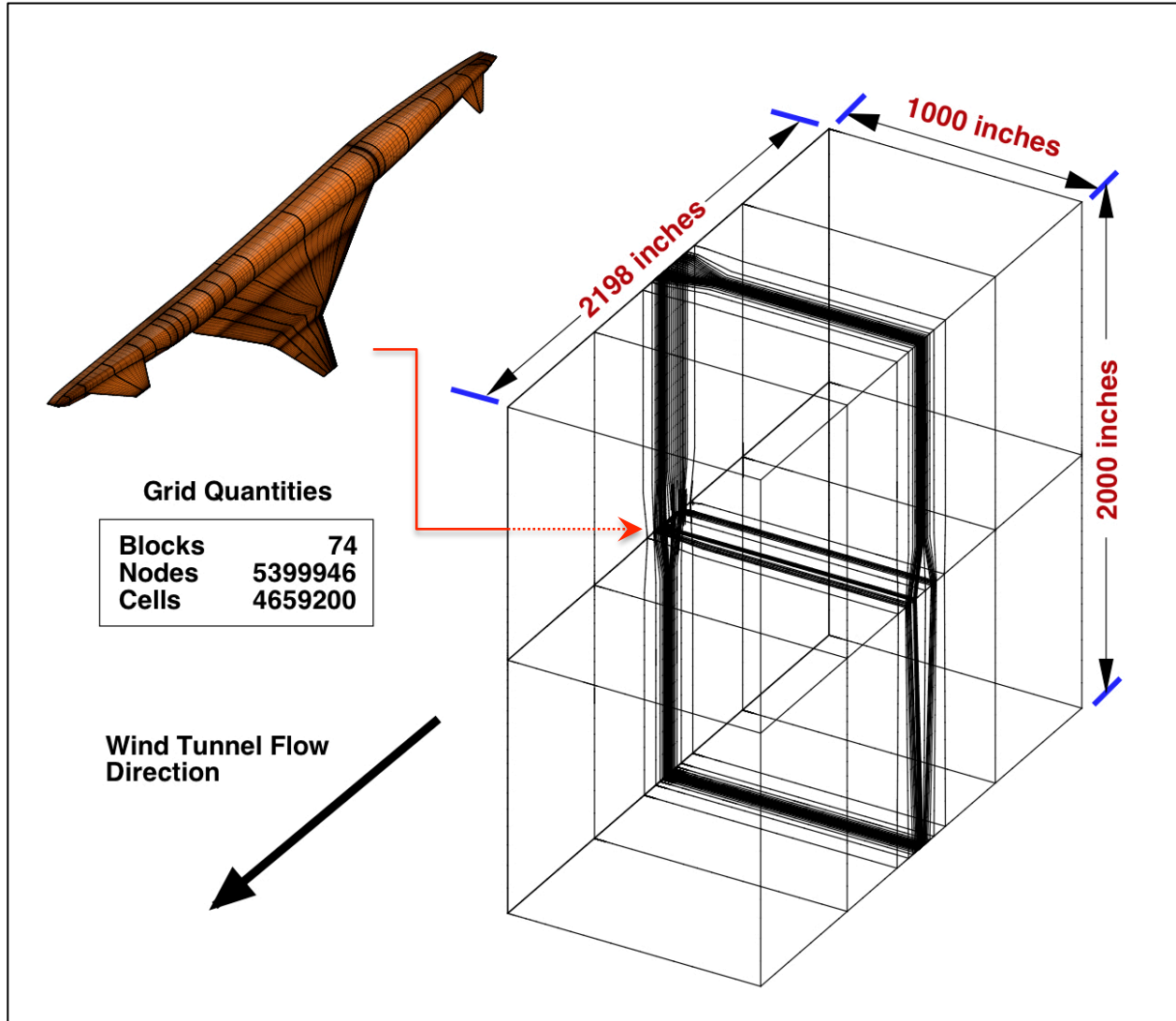
Figure 11.   Structured multi-block grid topologies of the computational domain for the geometry of the S^{4}T wind tunnel model without engine nacelles (viscous grid with a total of 74 grid blocks).

27

Total pressure ratio (p_t/p_∞), total temperature ratio (T_t/T_∞), Mach number (M_∞), and flow directions are specified.

Engine Intlet

Engine Outlet

Pressure ratio (p/p_∞) is specified.
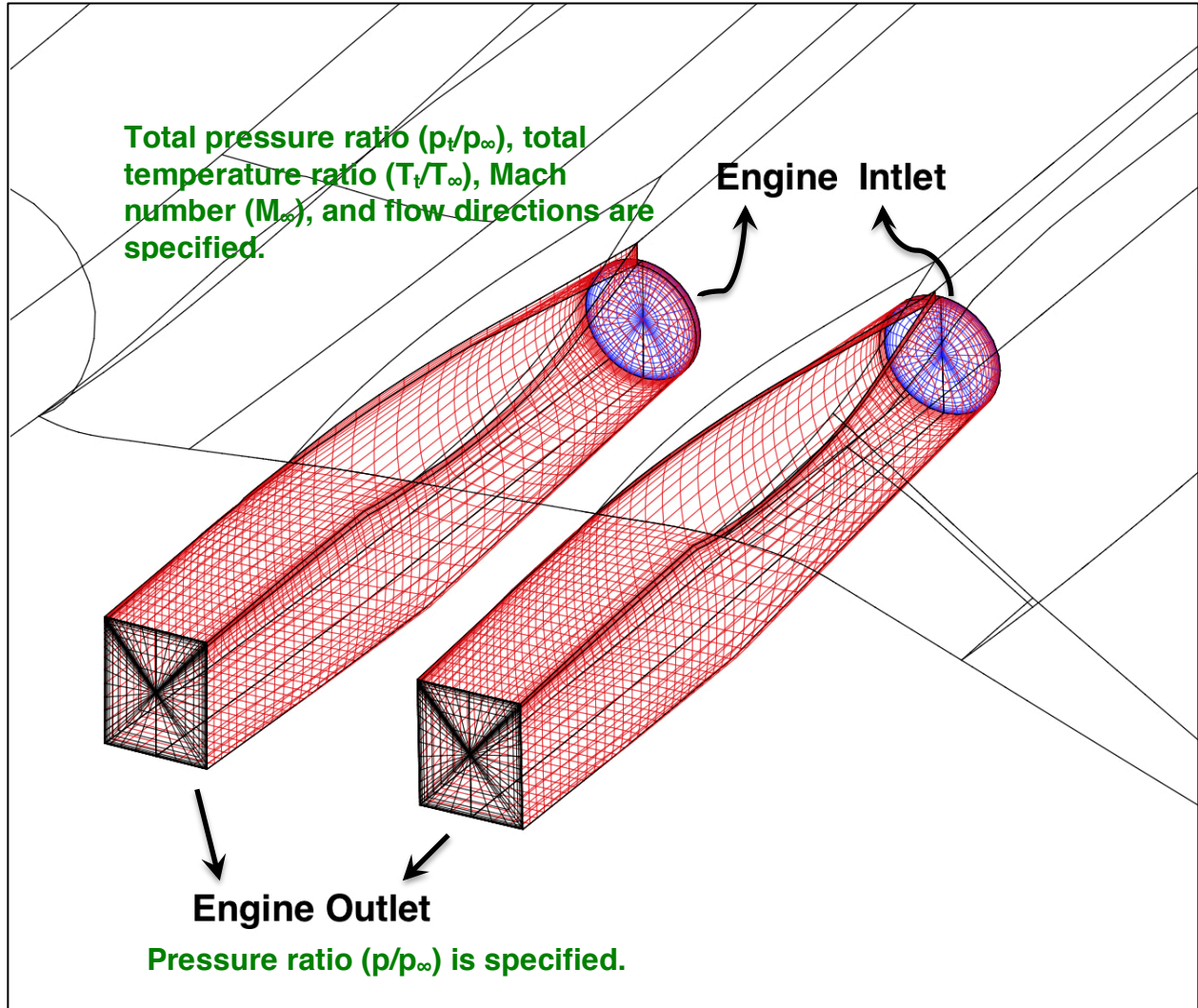
Figure 12.   Structured surface grids of the computational domain for the geometry of the engines.
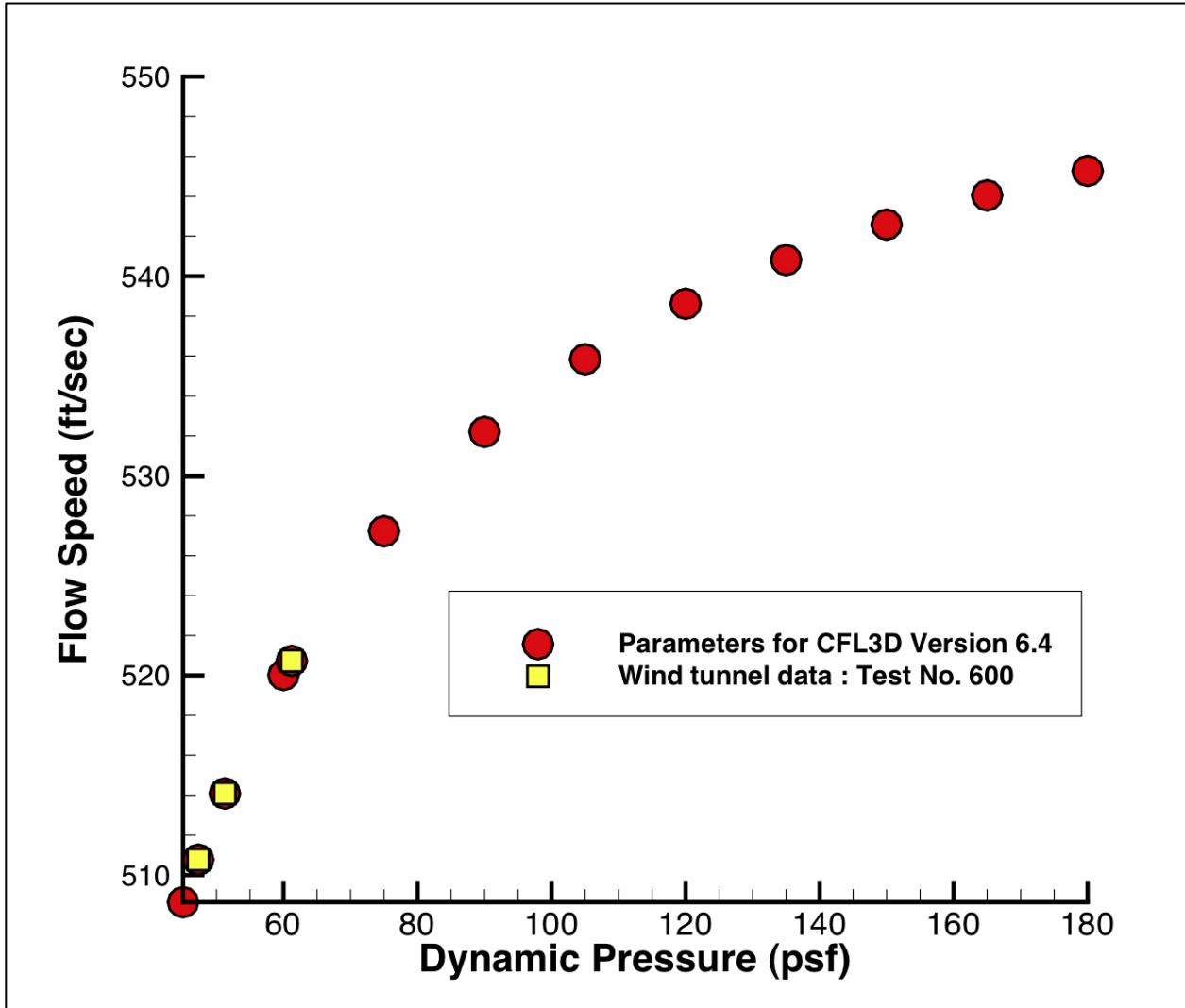
Figure 13. Relationship between dynamic pressure and flow speed at Mach 0.95 for the NASA Langley Research Center's Transonic Dynamics Tunnel (TDT)'s test medium (R-134a).
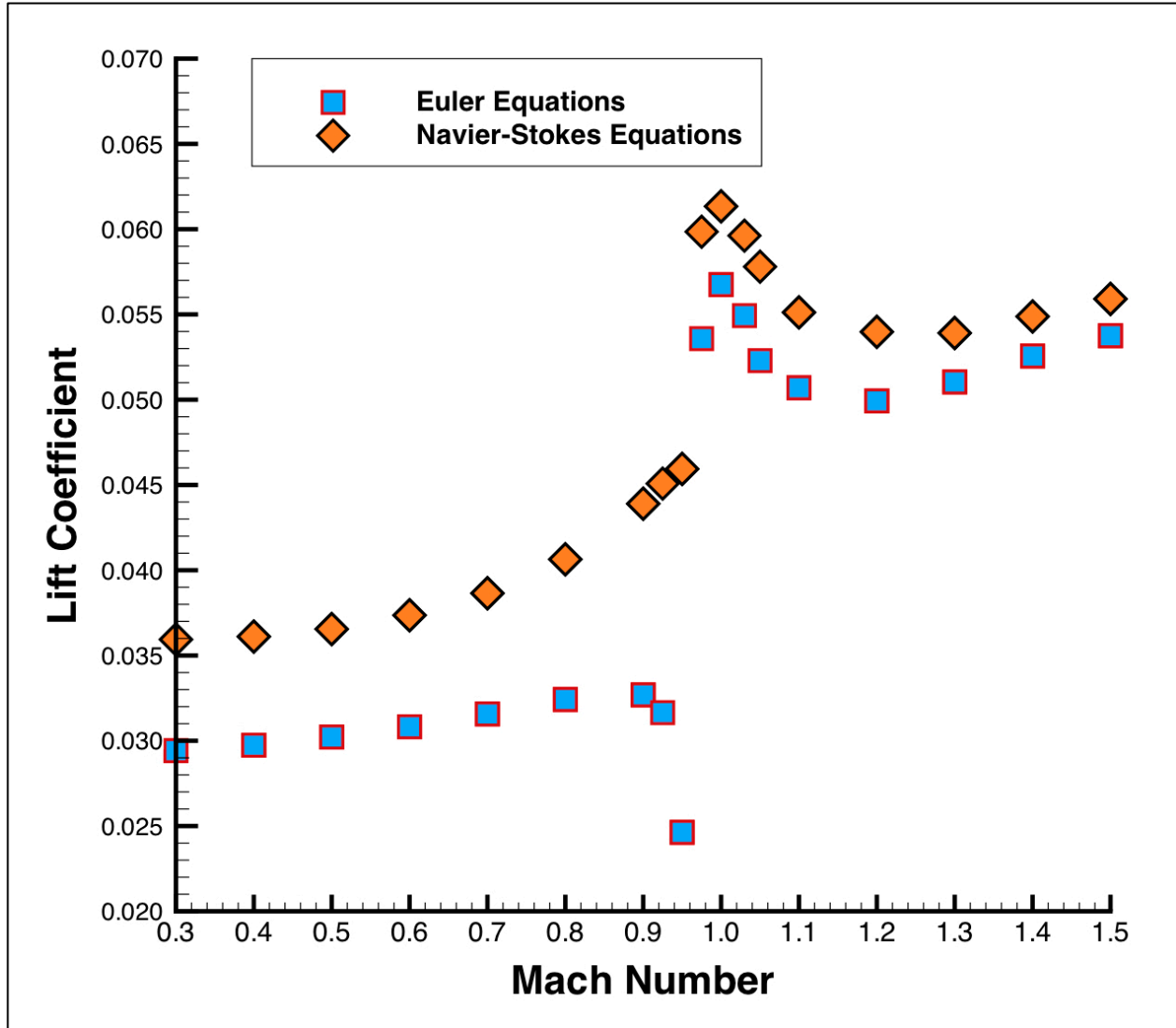
Figure 14. Lift coefficient vs. Mach number for 2° angle of attack. The original configuration of the S[4]T wind tunnel model with engine nacelles was applied.
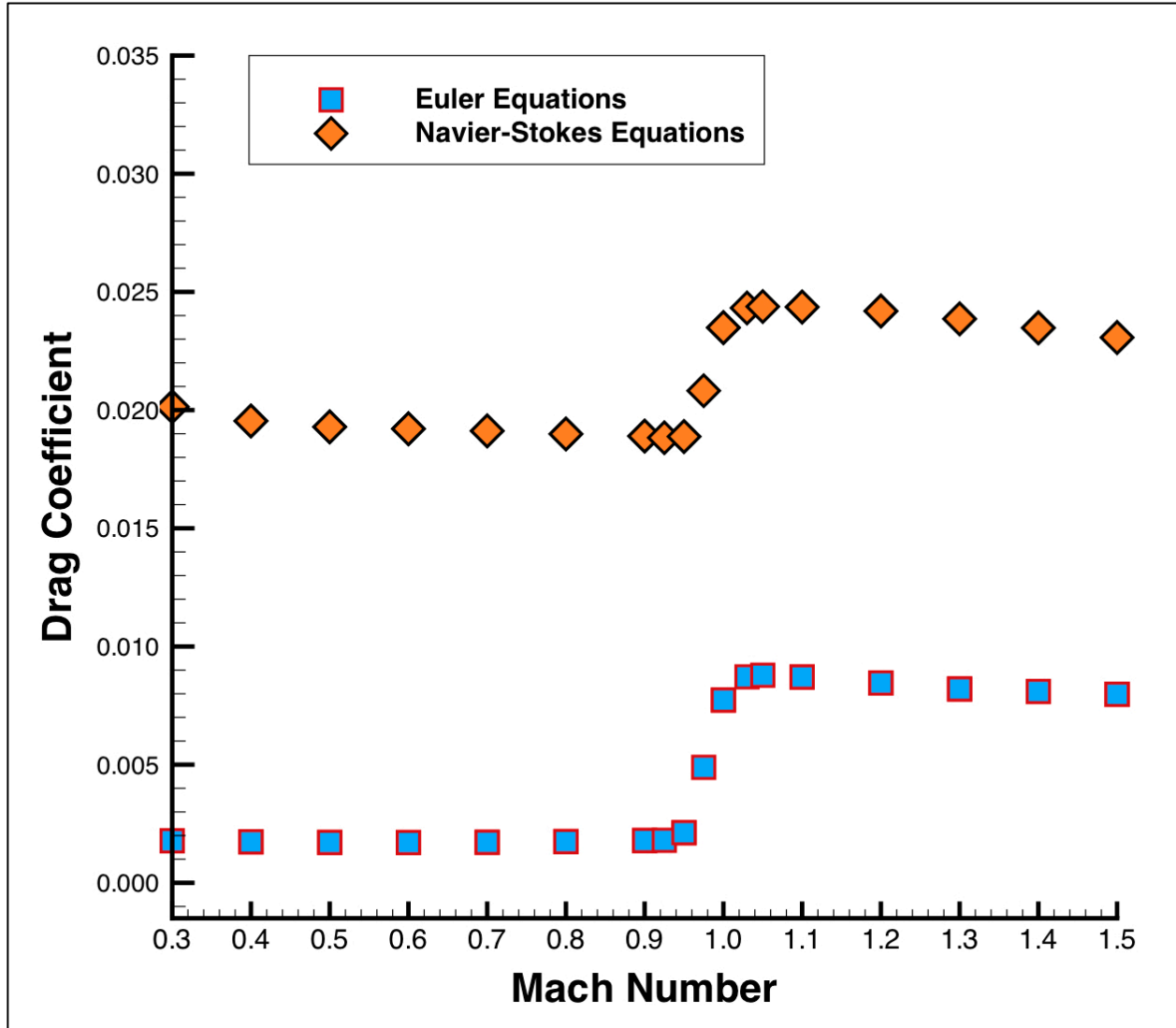
Figure 15. Drag coefficient vs. Mach number for 2° angle of attack. The original configuration of the S^{4}T wind tunnel model with engine nacelles was applied.
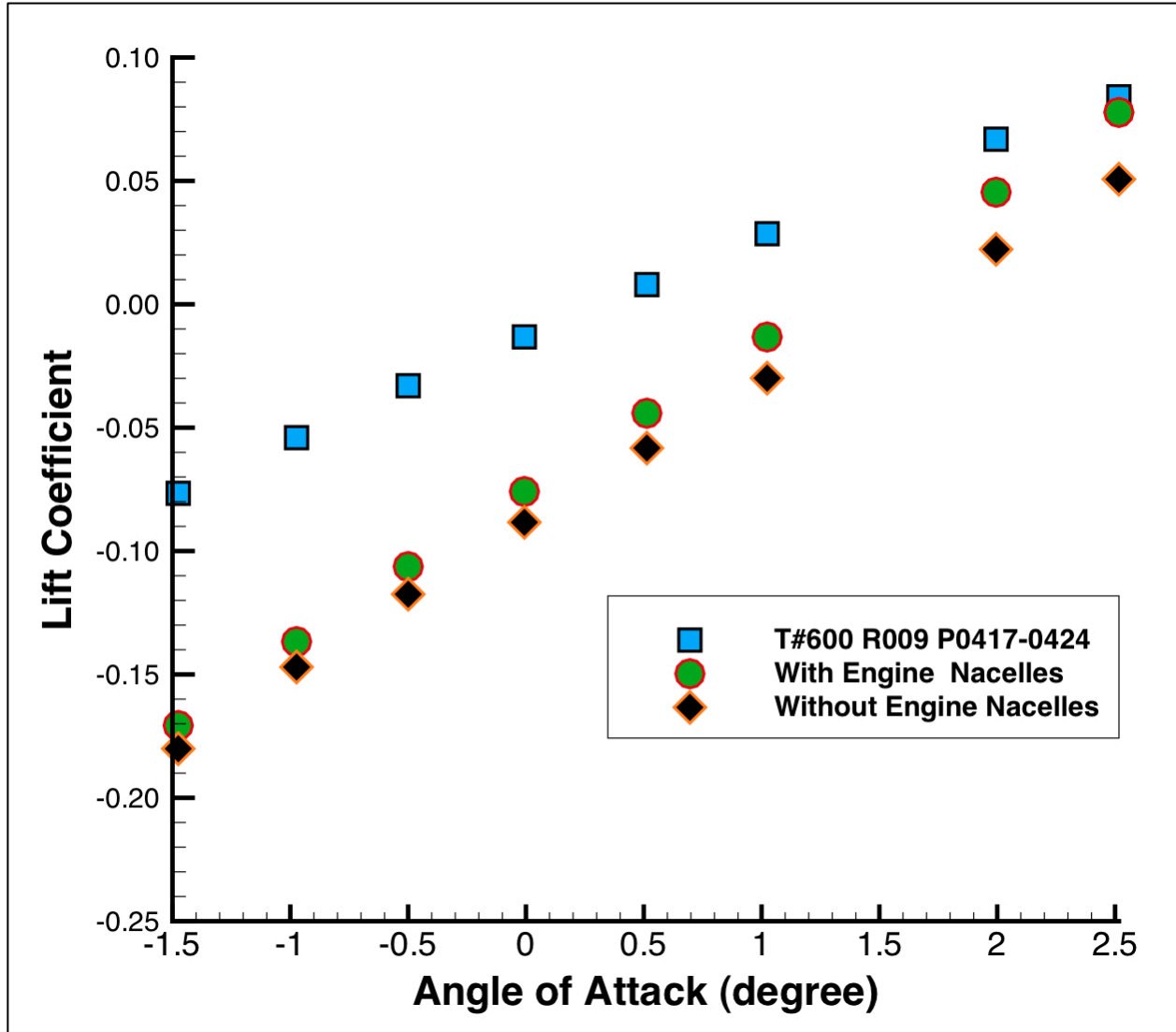
Figure 16. Lift coefficient vs. angle of attack for Mach 0.95. Results from the Navier-Stokes simulations about the S^{4}T wind tunnel model (with/without engine nacelles) are compared to data from Run No. 009 at TDT Test No. 600.
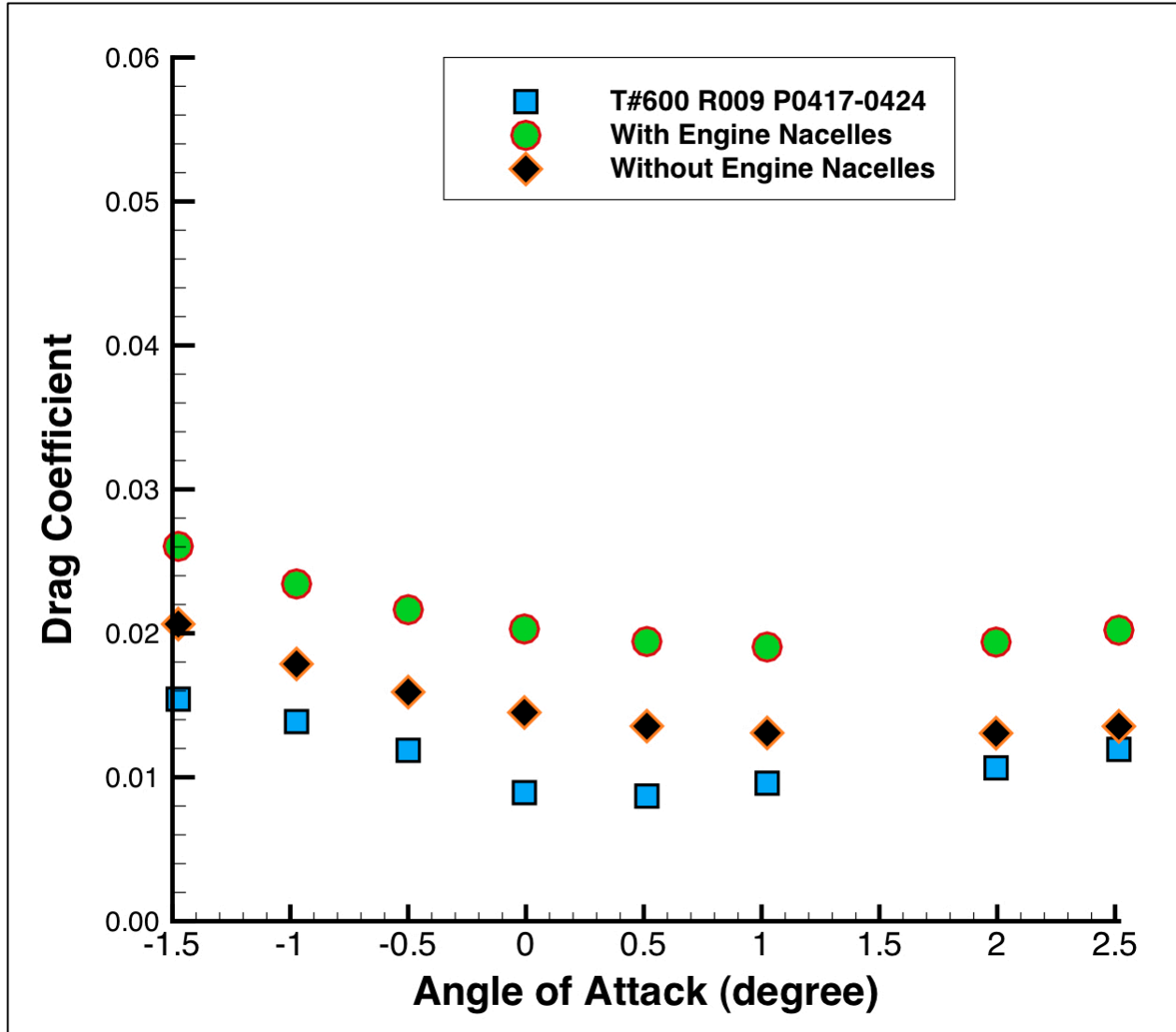
Figure 17. Drag coefficient vs. angle of attack for Mach 0.95. Results from the Navier-Stokes simulations about the S^4T wind tunnel model (with/without engine nacelles) are compared to data from Run No. 009 at TDT Test No. 600.
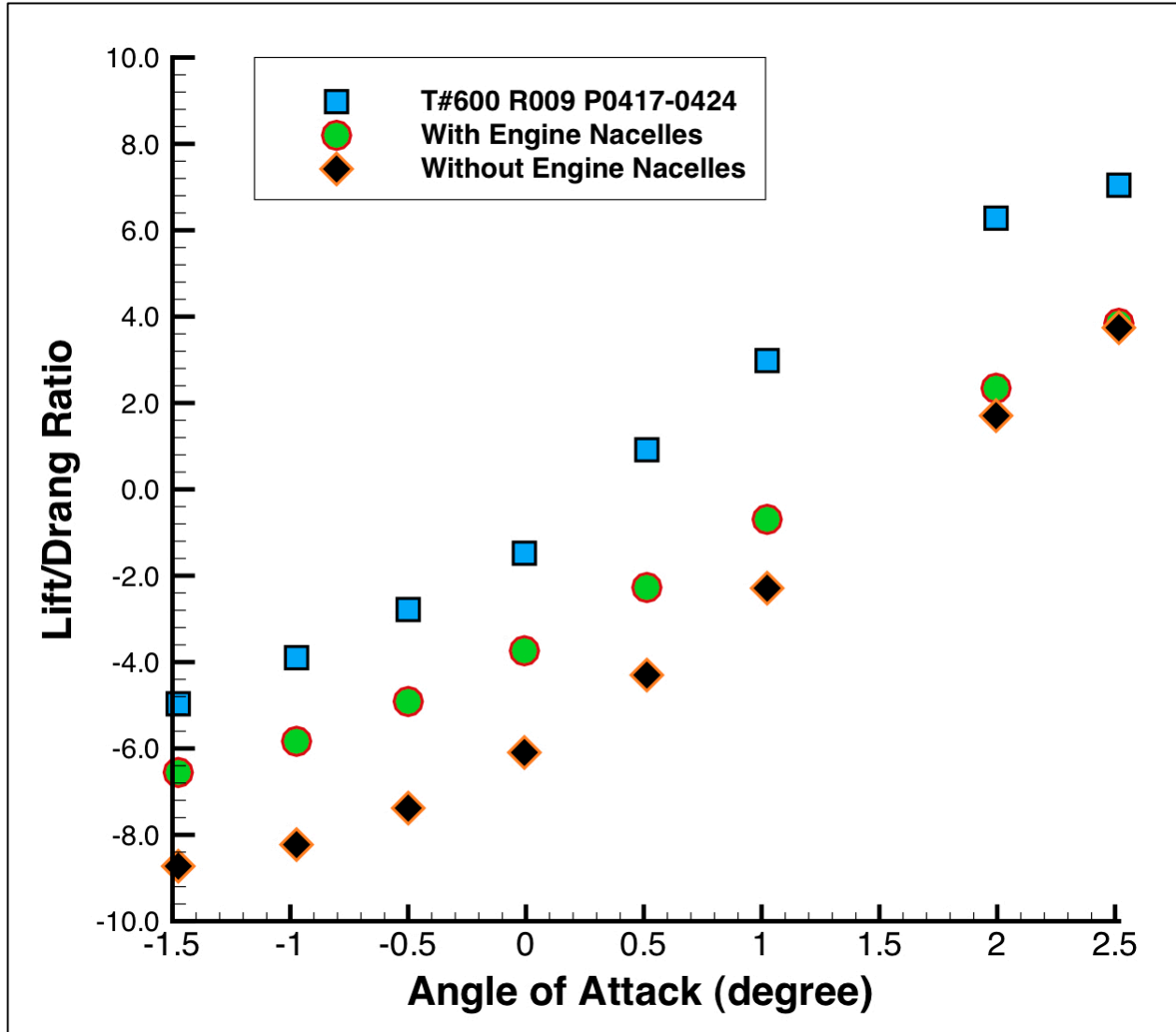
Figure 18. Lift /drag ratio vs. angle of attack for Mach 0.95. Results from the Navier Stokes simulations about the S^{4}T wind tunnel model (with/without engine nacelles) are compared to data from Run No. 009 at TDT Test No. 600.
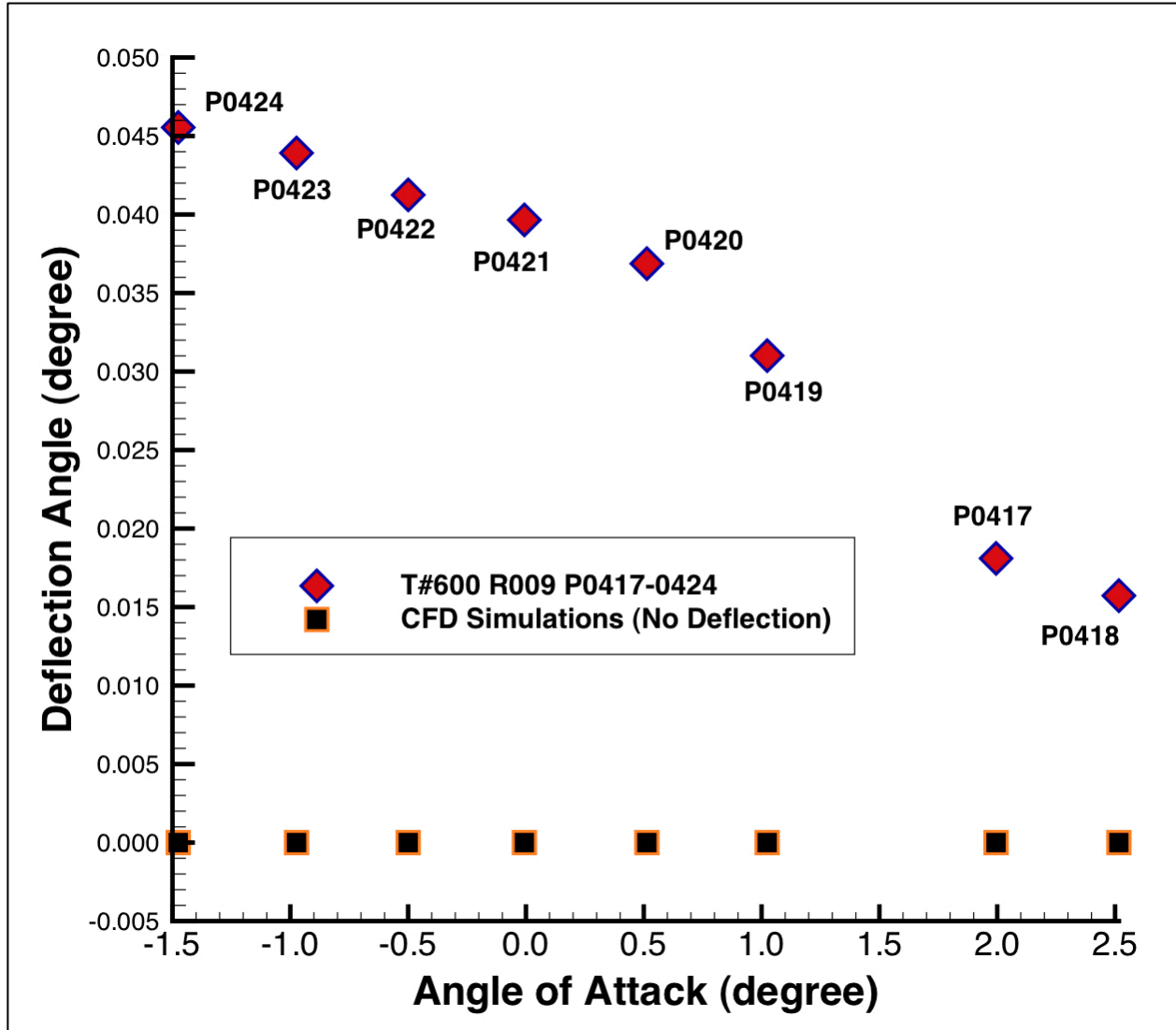
Figure 19. Fluctuated positions of wing flap. Results from Run No. 009 at TDT Test No. 600.
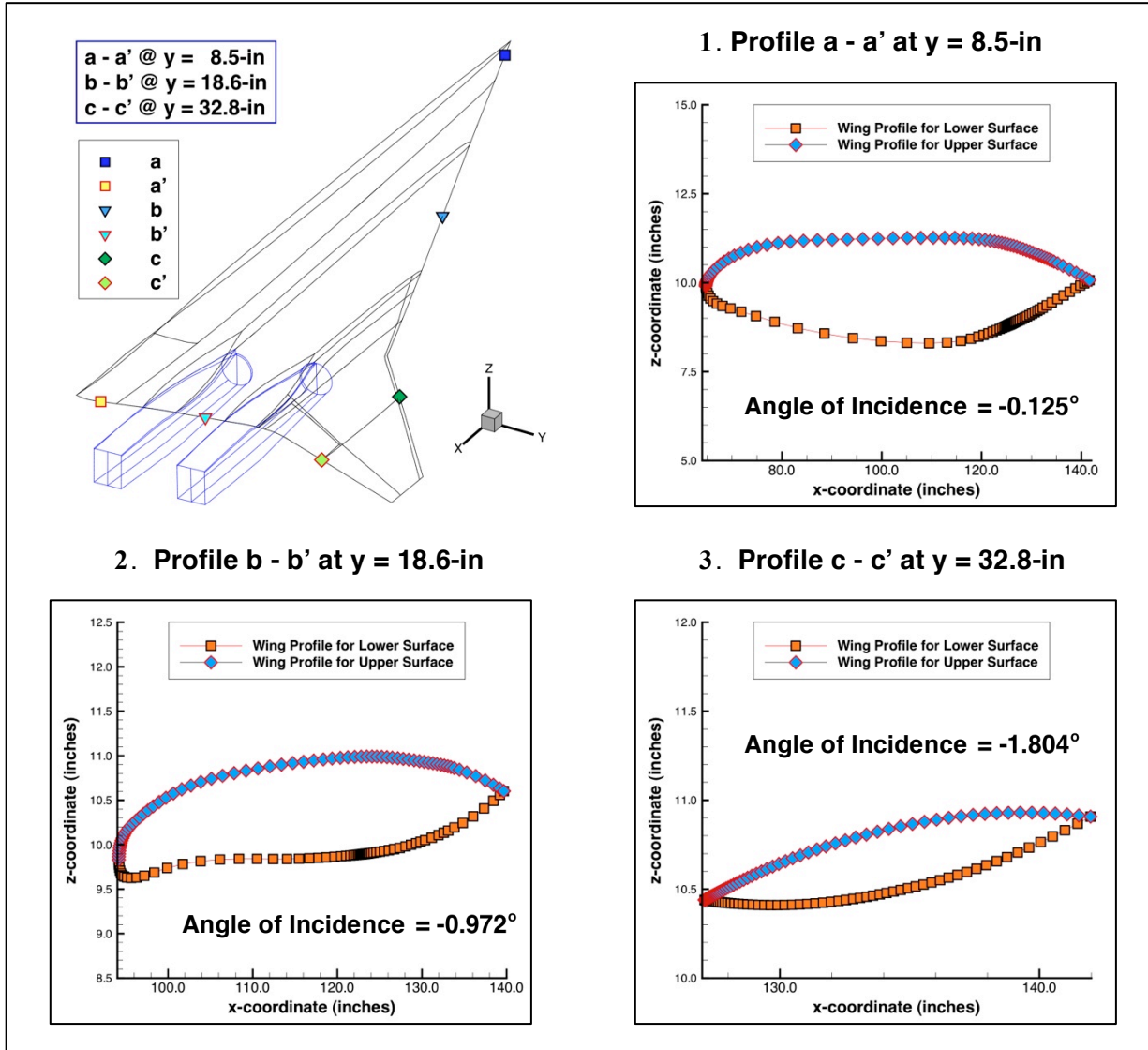
Figure 20. The selected wing profile shapes for inboard, mid-span, and outboard wing portions that form the basis of the pressure coefficients plots.

36
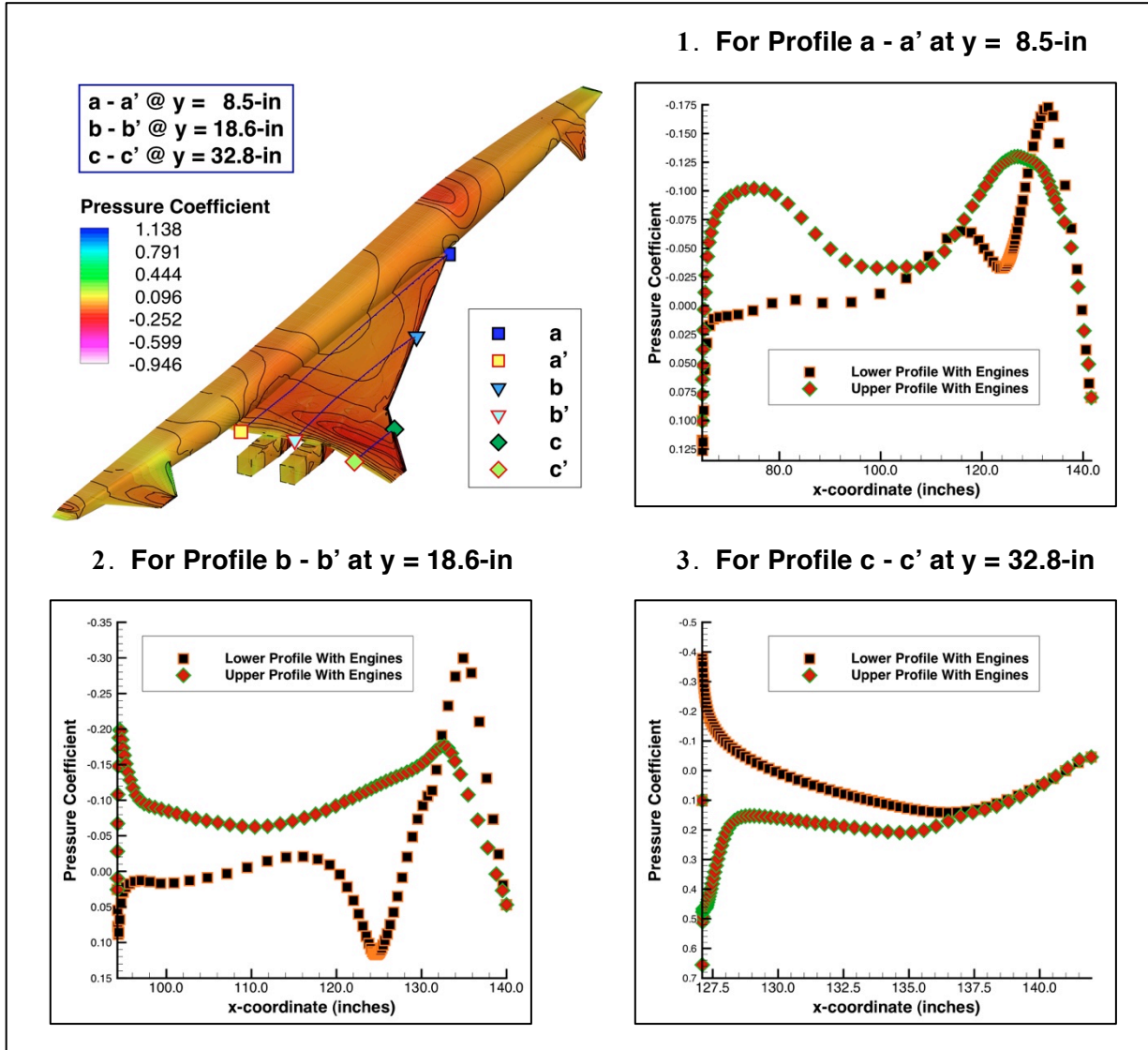
Figure 21. Numerically obtained pressure coefficient contours and plots on wing profiles at an angle of attack of 2º measured at selected lateral-positions for the S^{4}T wind tunnel model shape with engines.
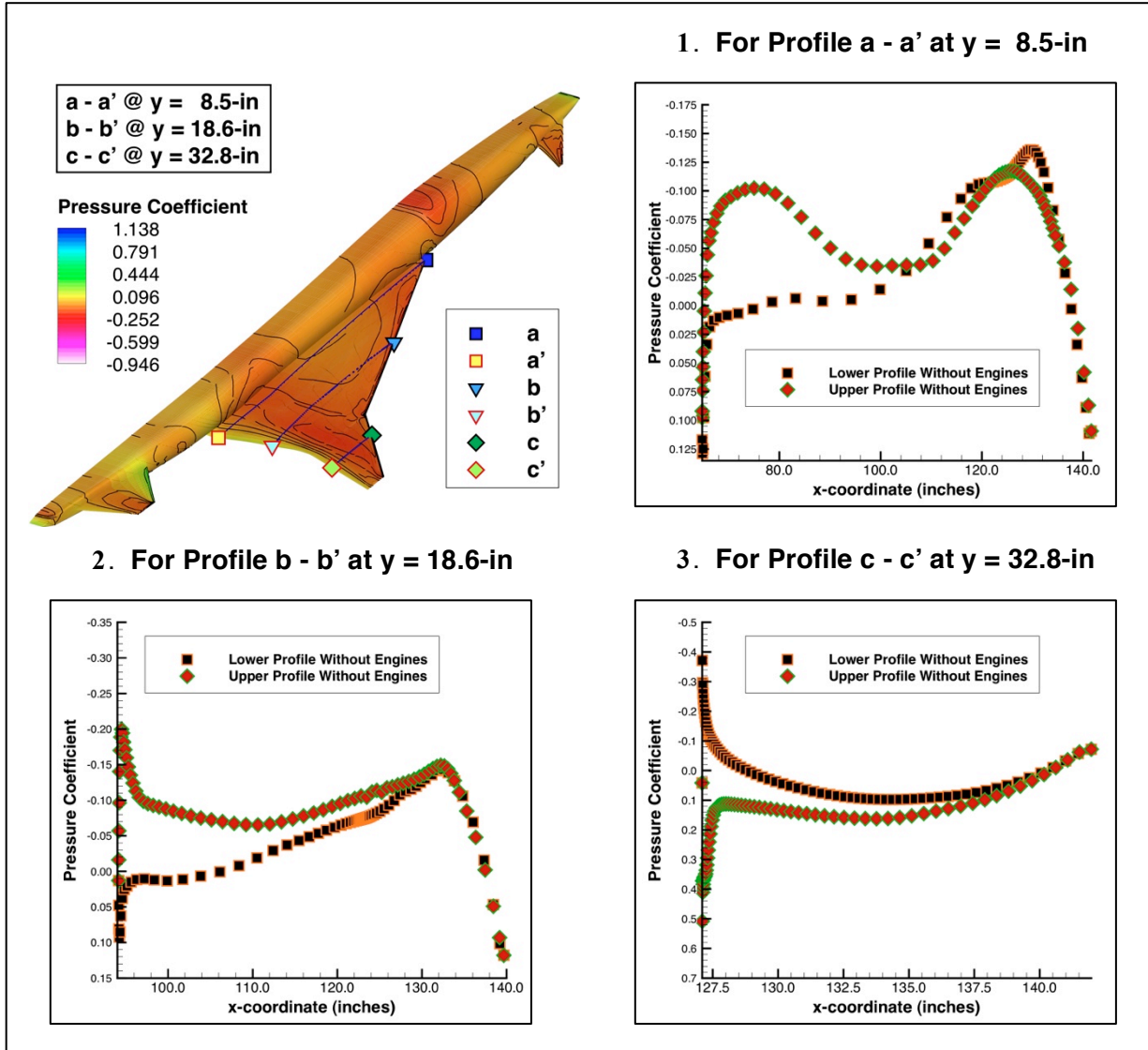
Figure 22. Numerically obtained pressure coefficient contours and plots on wing profiles at an angle of attack of 2º measured at selected lateral positions for the S^{4}T wind tunnel model shape without engines.
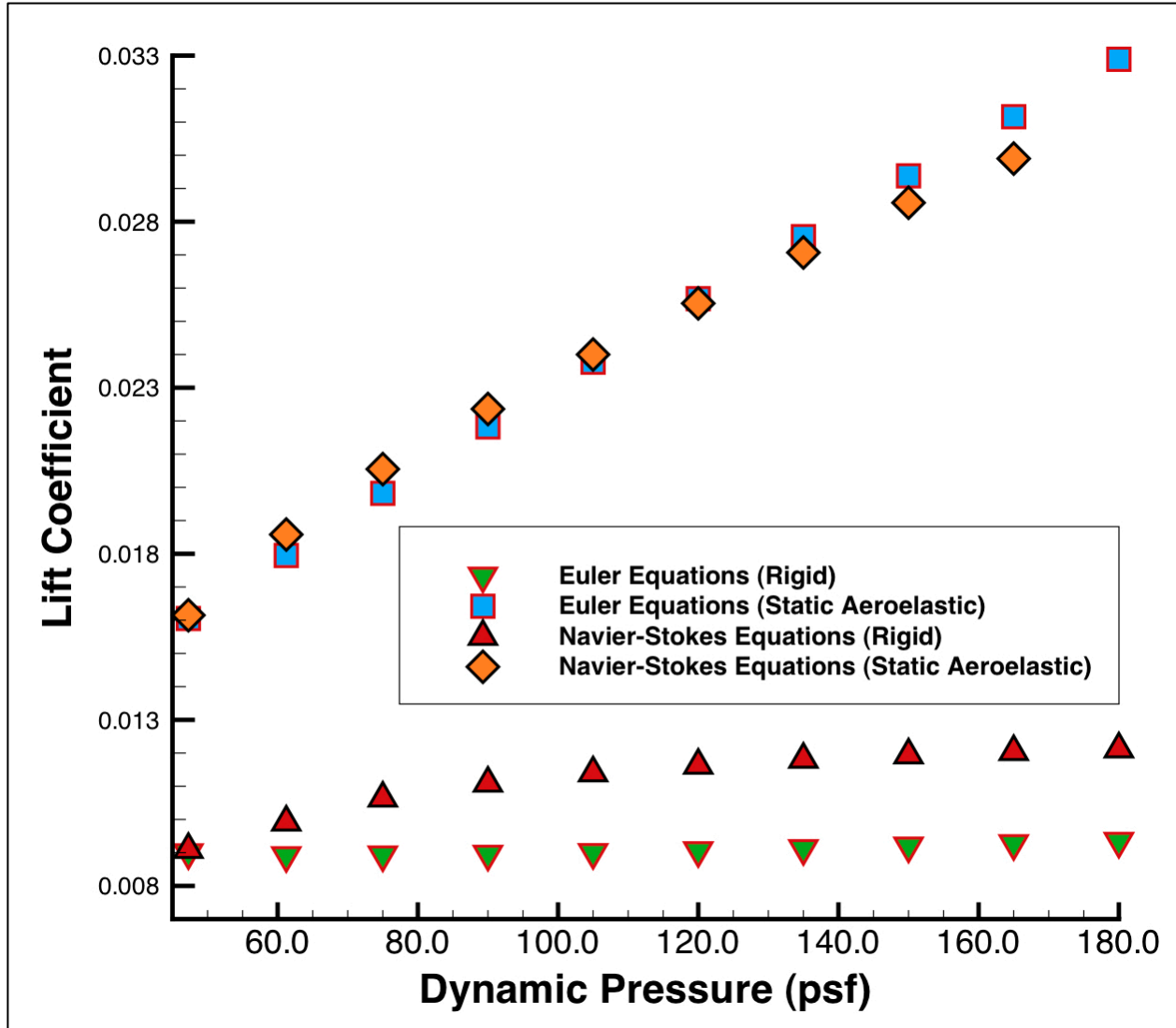
Figure 23. Lift coefficients obtained from rigid and static aeroelastic simulations using both the Euler and Navier-Stokes equations for the heavy gas R-134a, Mach 0.95 with a fixed 1.75° angle of attack.
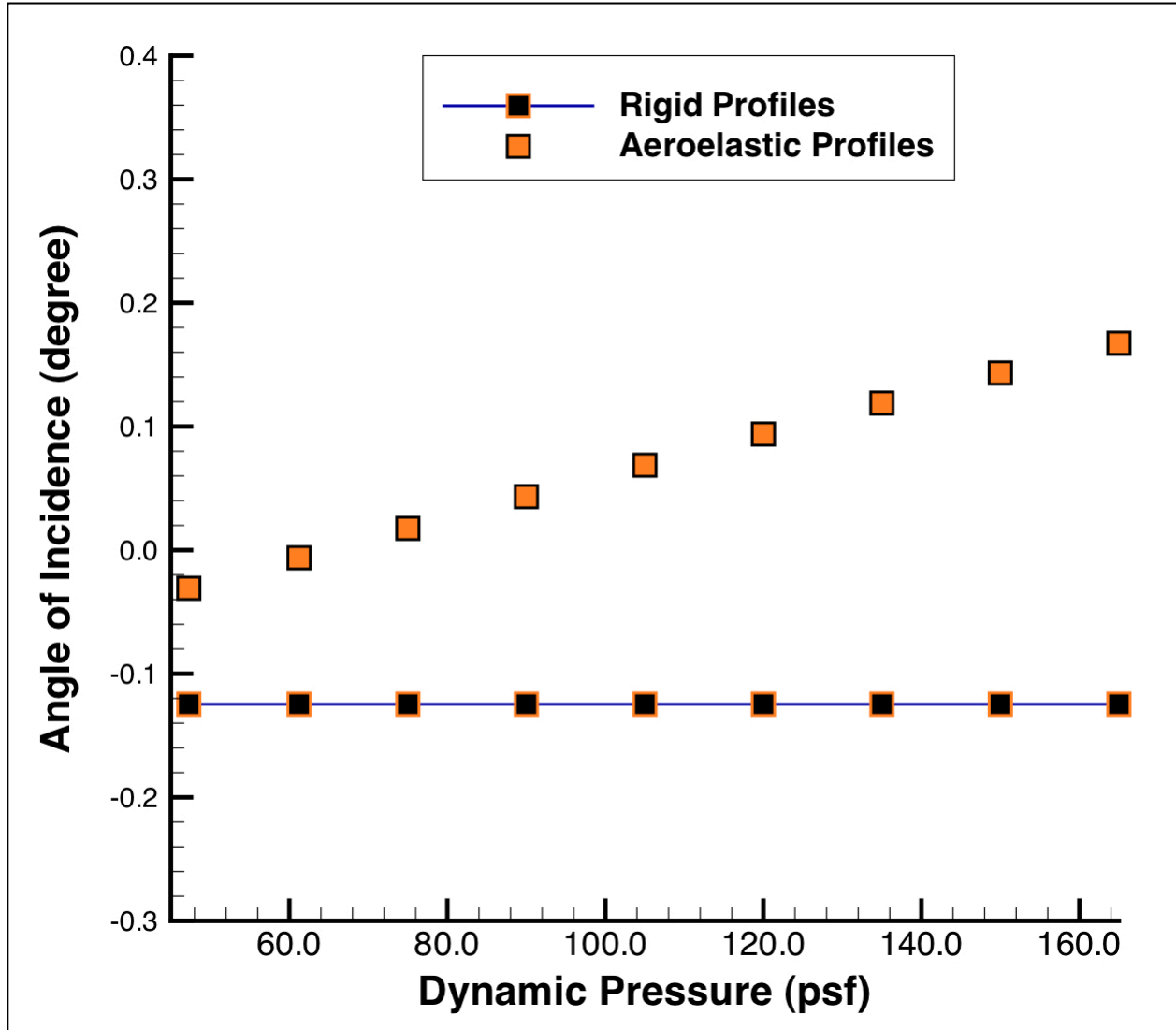
Figure 24. Angles of incidence for inboard wing portion (about 8.5-in of *y*-position) resulted from static aeroelastic analyses over various dynamic pressures.
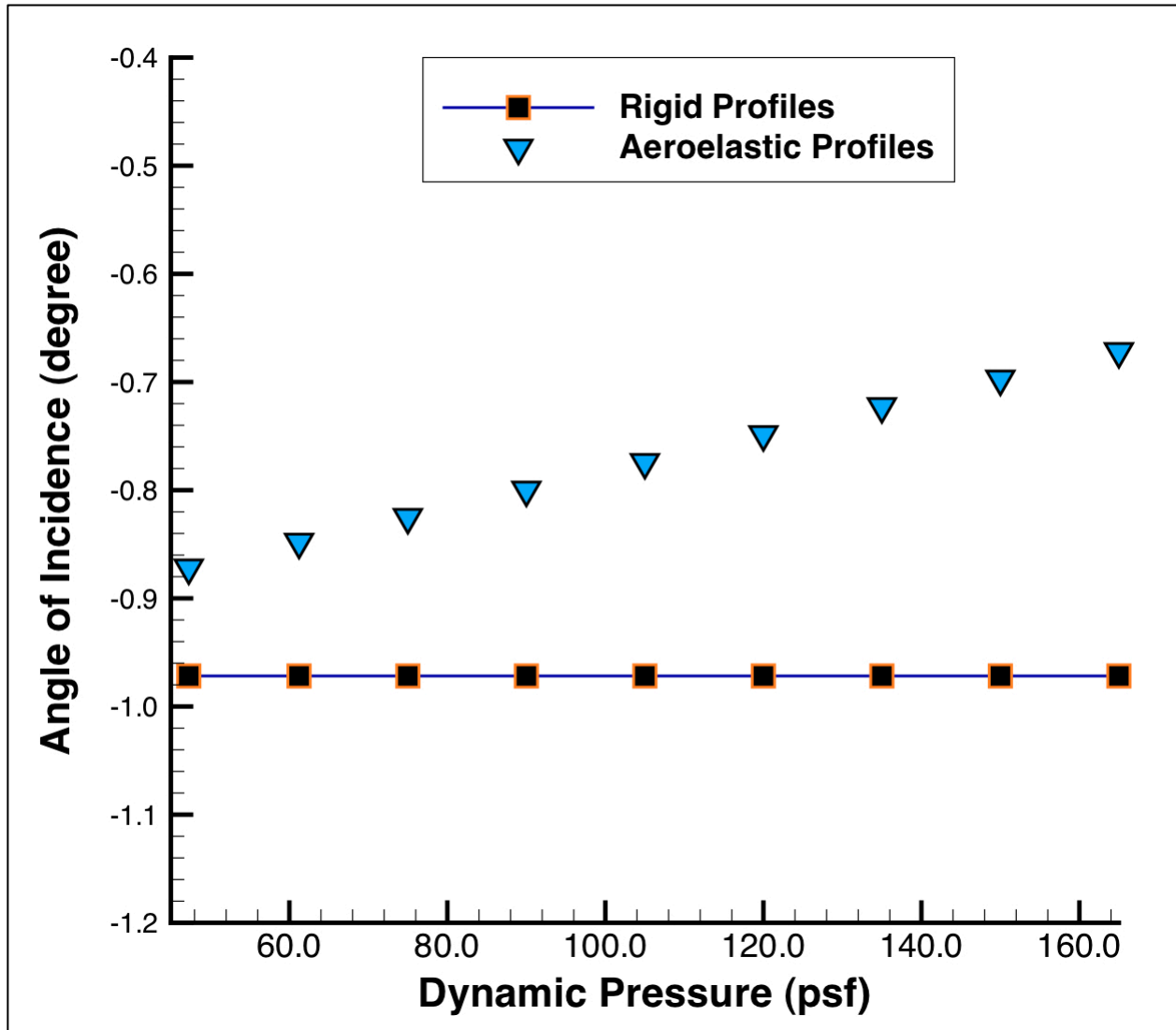
Figure 25. Angles of incidence for mid-span wing portion (about 18.6-in of *y*-position) resulted from static aeroelastic analyses over various dynamic pressures.
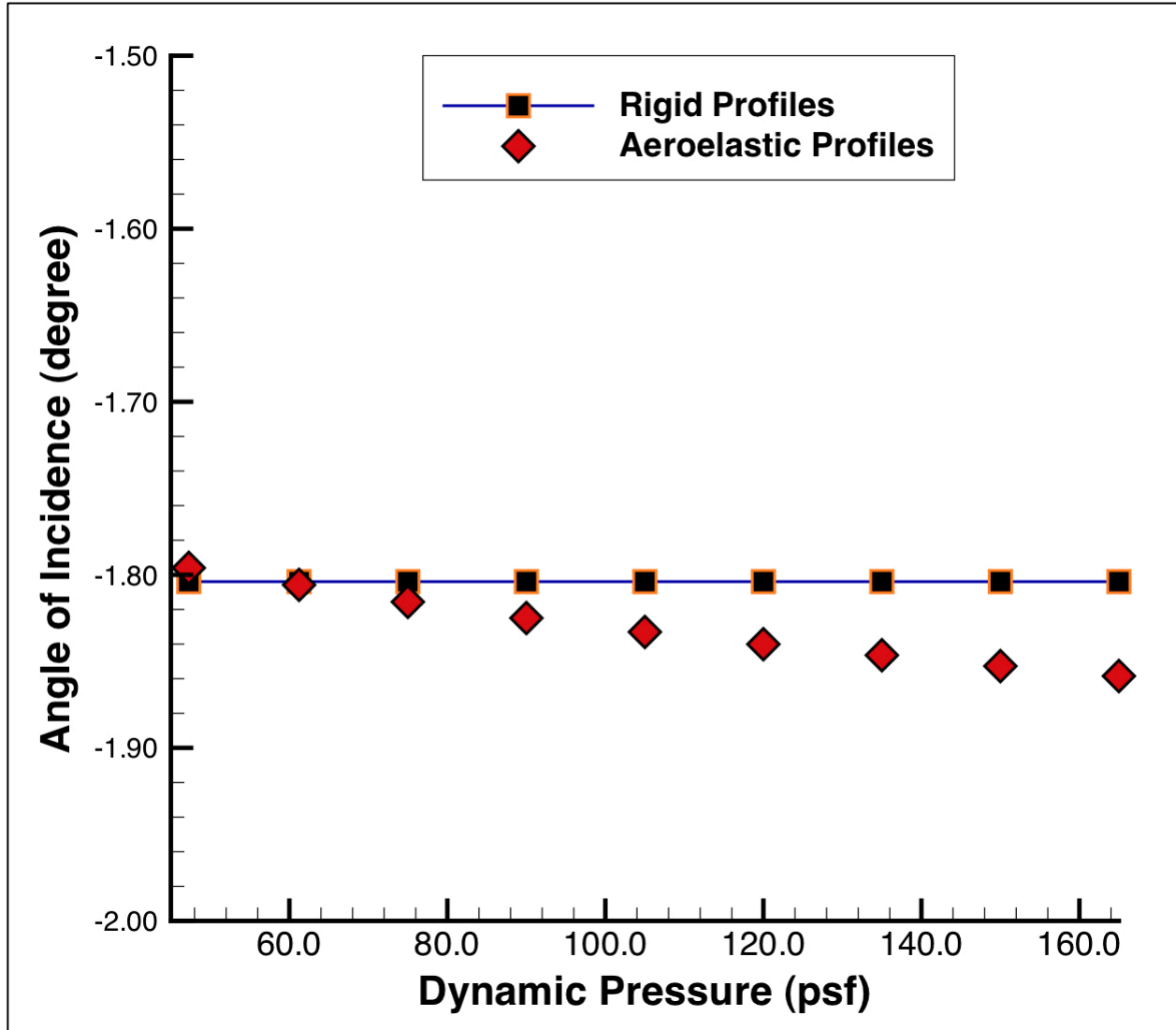
Figure 26. Angles of incidence for inboard wing portion (about 32.8-in of *y*-position) resulted from static aeroelastic analyses over various dynamic pressures.
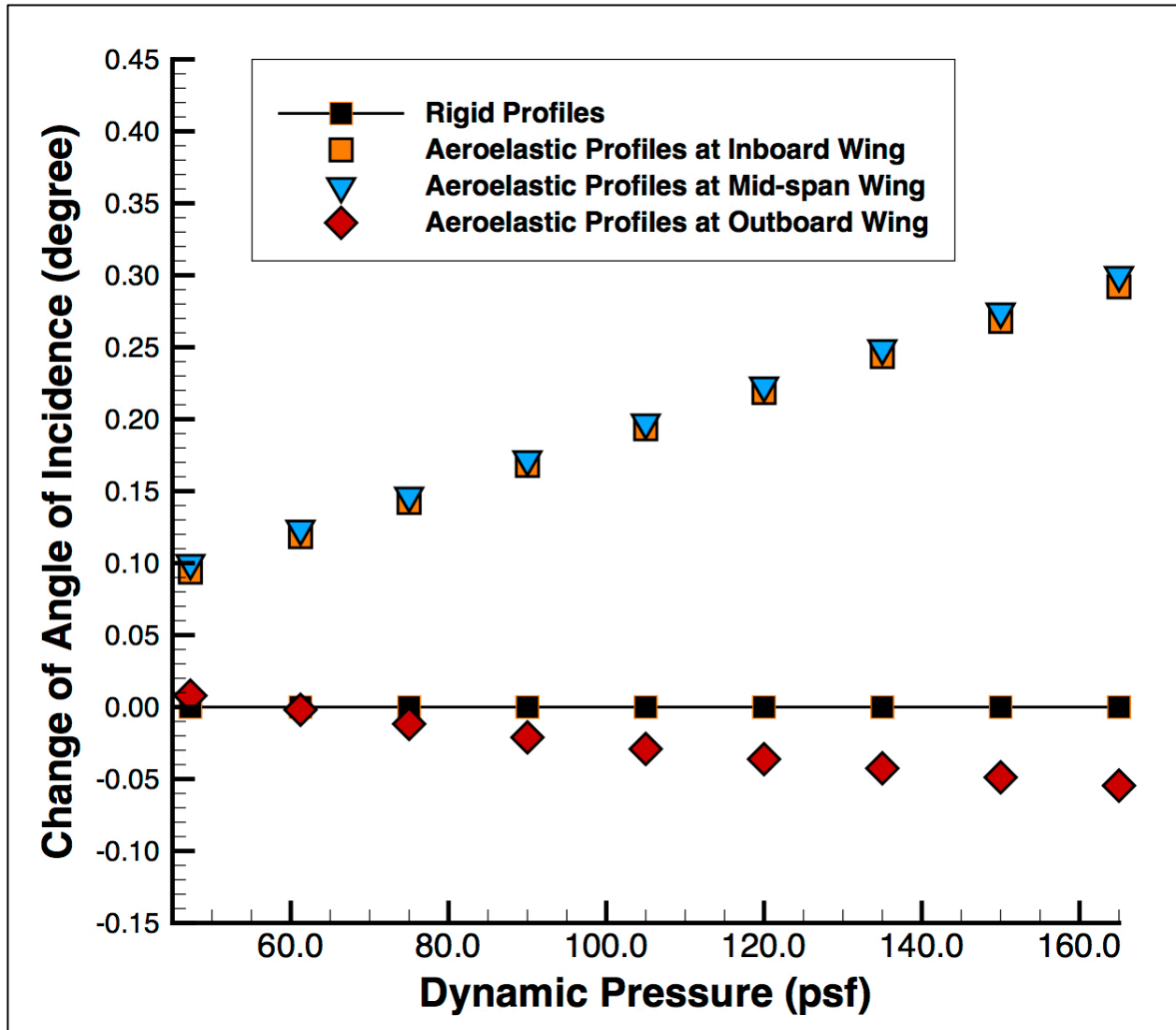
Figure 27. Increased/decreased amount of the local angles of incidence for inboard, mid-span, and outboard wing portions (about 8.5, 18.6, and 32.8-in of *y*-positions) resulted from static aeroelastic analyses over various dynamic pressures.
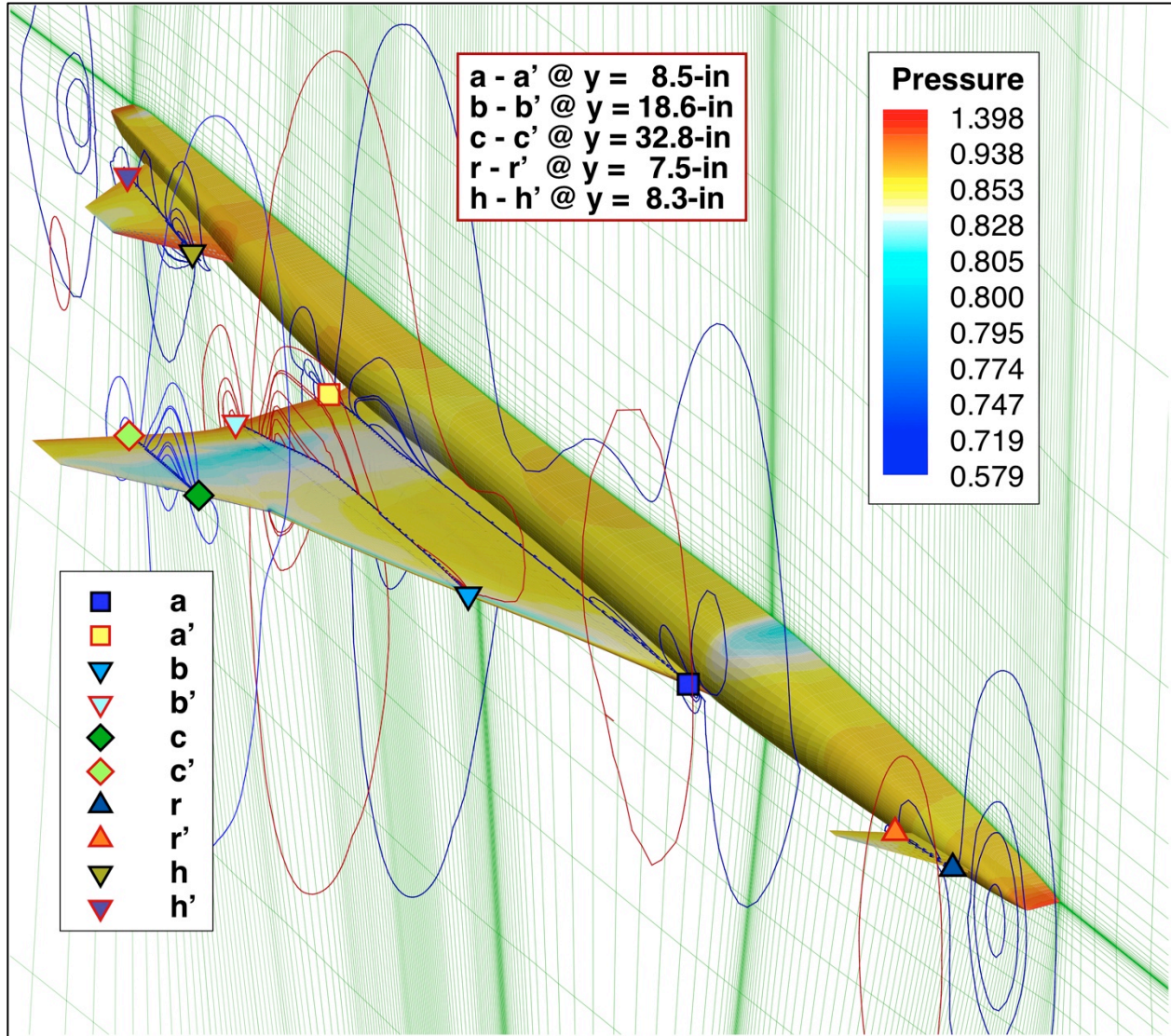
Figure 28. Pressure (non-dimensional) contours on the S^{4}T wind tunnel model obtained by static aeroelastic calculations at a dynamic pressure of 90.0-psf using the Navier-Stokes equations. The section surfaces for contours cut the model shape through wing at 8.50, 18.6, and 32.8-in respectively and RCV and HT at 7.47 and 8.32-in respectively.
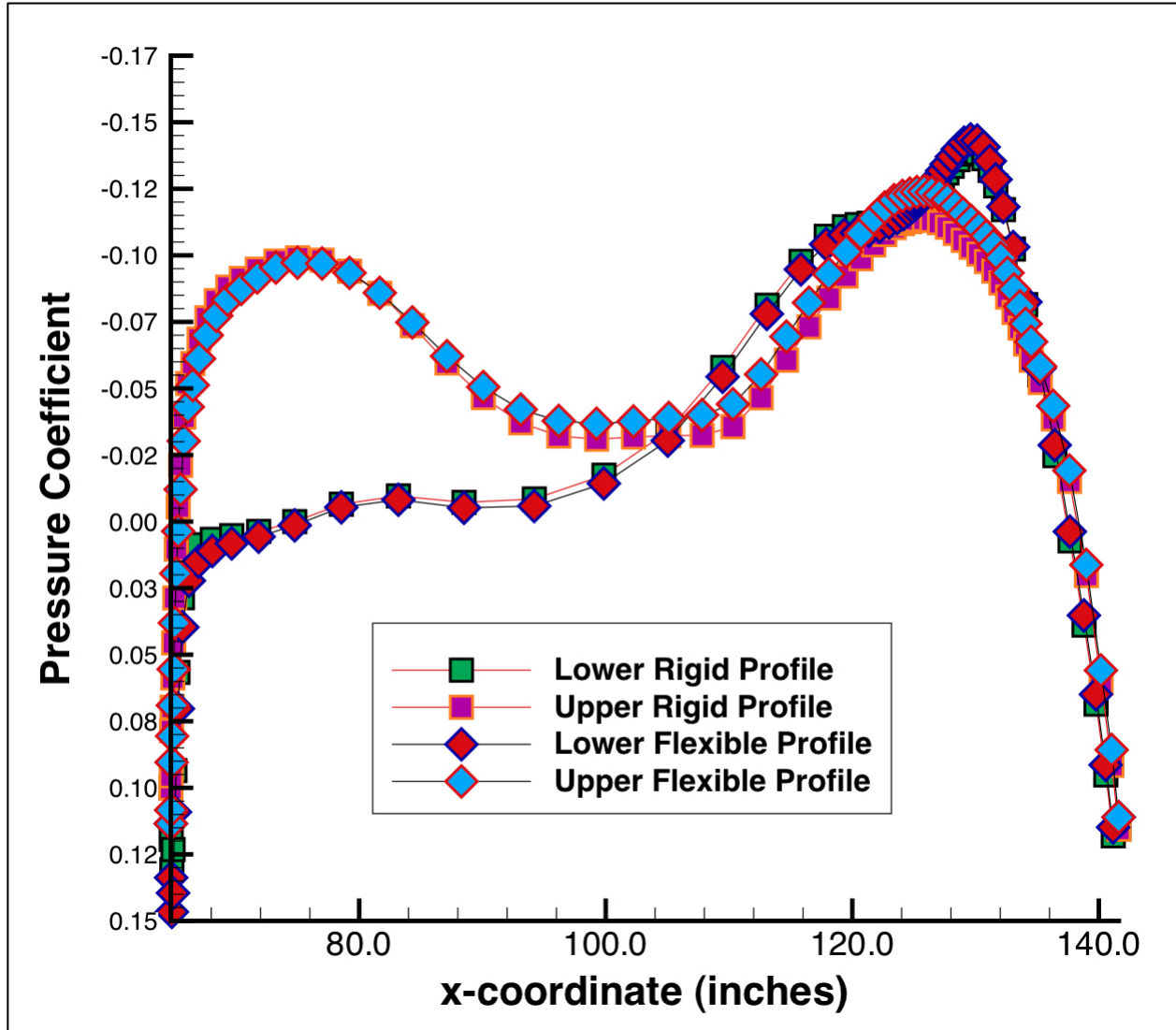
Figure 29. Plot for the comparison of pressure coefficient on the selected wing profile at 8.50-in in *y*-position for the inboard wing portion obtained by aerodynamic and aeroelastic calculations at a dynamic pressure of 90.0-psf using the Navier-Stokes equations.
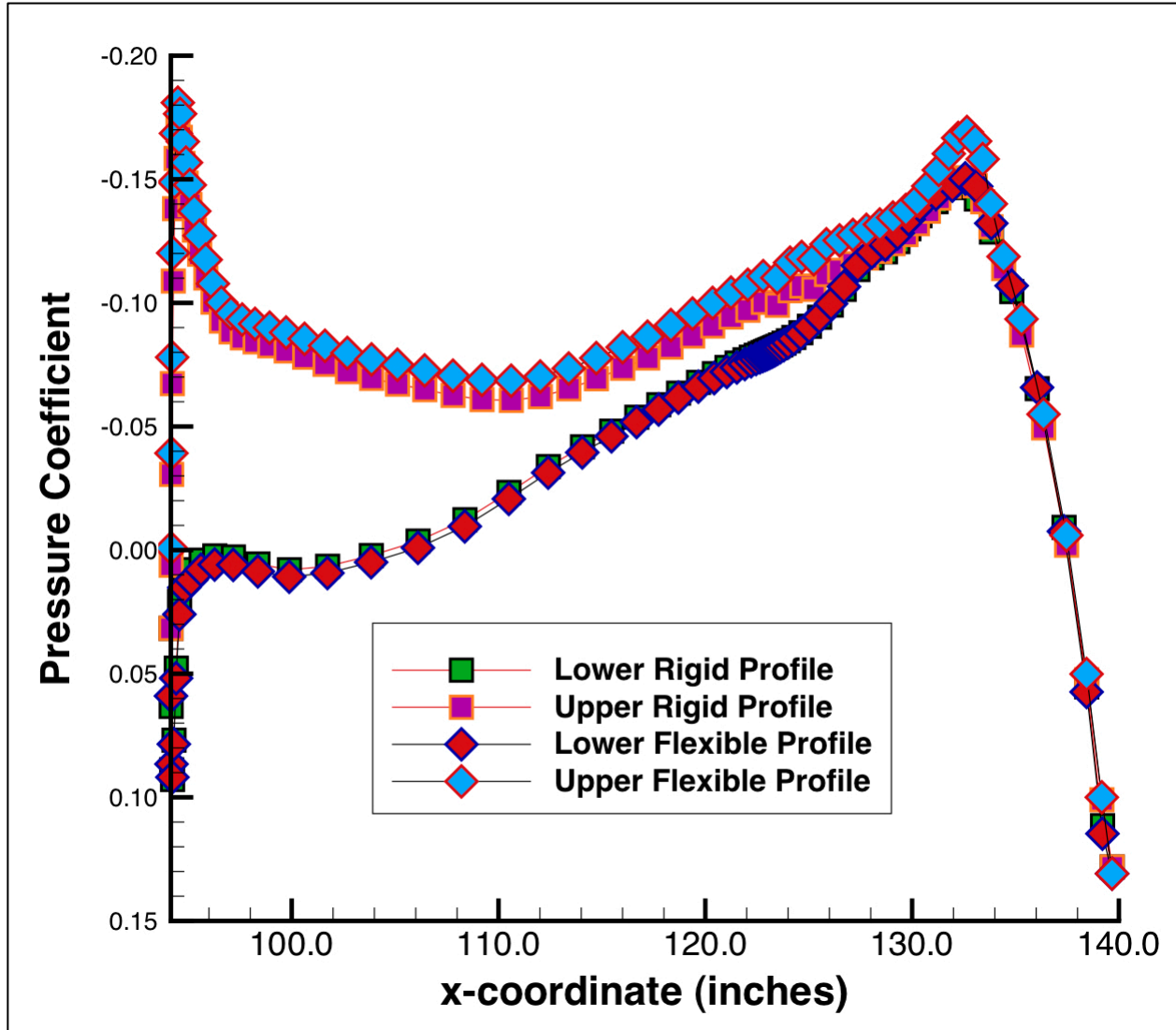
Figure 30. Plot for the comparison of pressure coefficient on the selected wing profile at 18.6-in in *y*-position for the mid-span wing portion obtained by aerodynamic and aeroelastic calculations at a dynamic pressure of 90.0-psf using the Navier-Stokes equations.
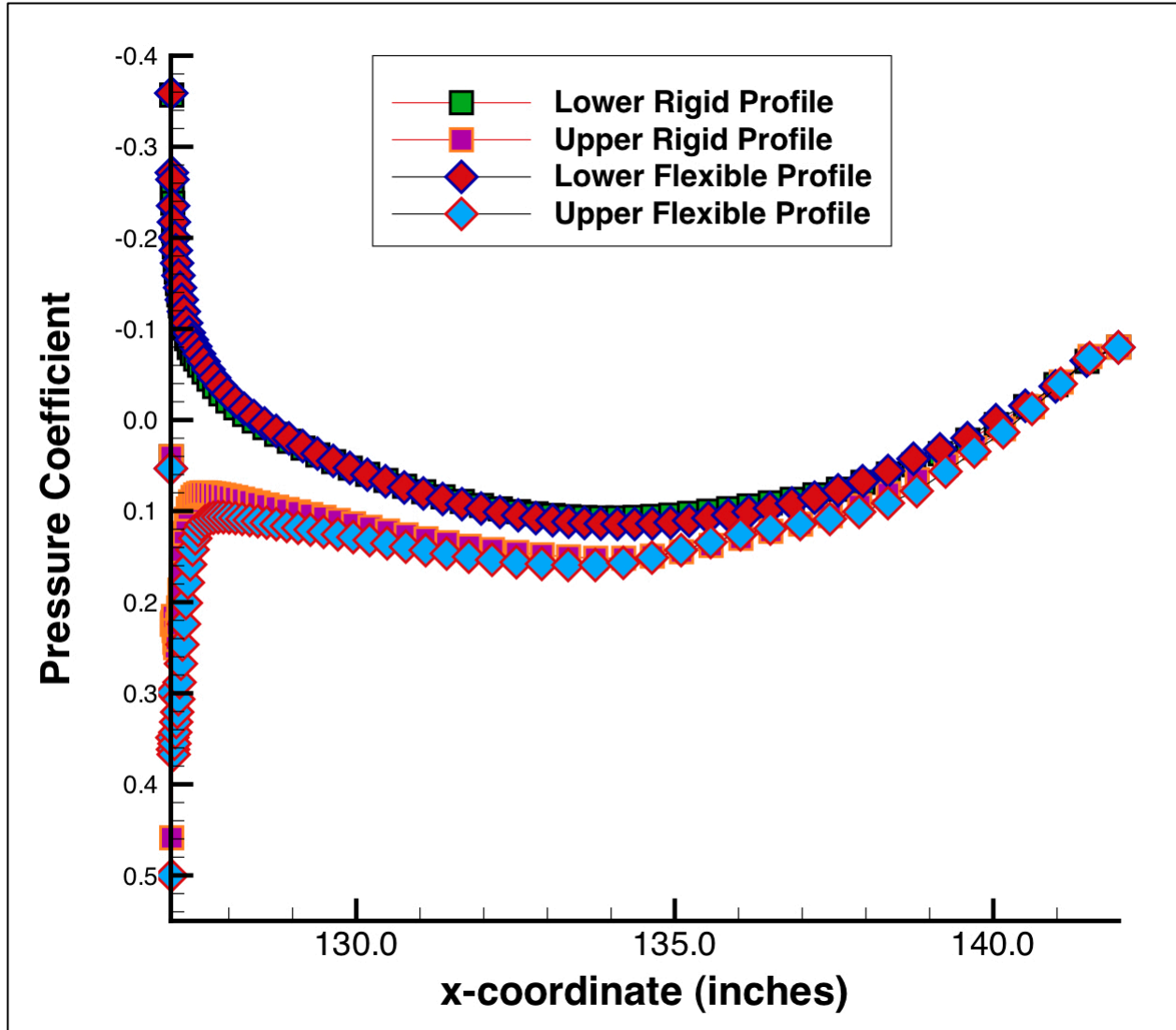
Figure 31. Plot for the comparison of pressure coefficient on the selected wing profile at 32.8-in in *y*-position for the outboard wing portion obtained by aerodynamic and aeroelastic calculations at a dynamic pressure of 90.0-psf using the Navier-Stokes equations.
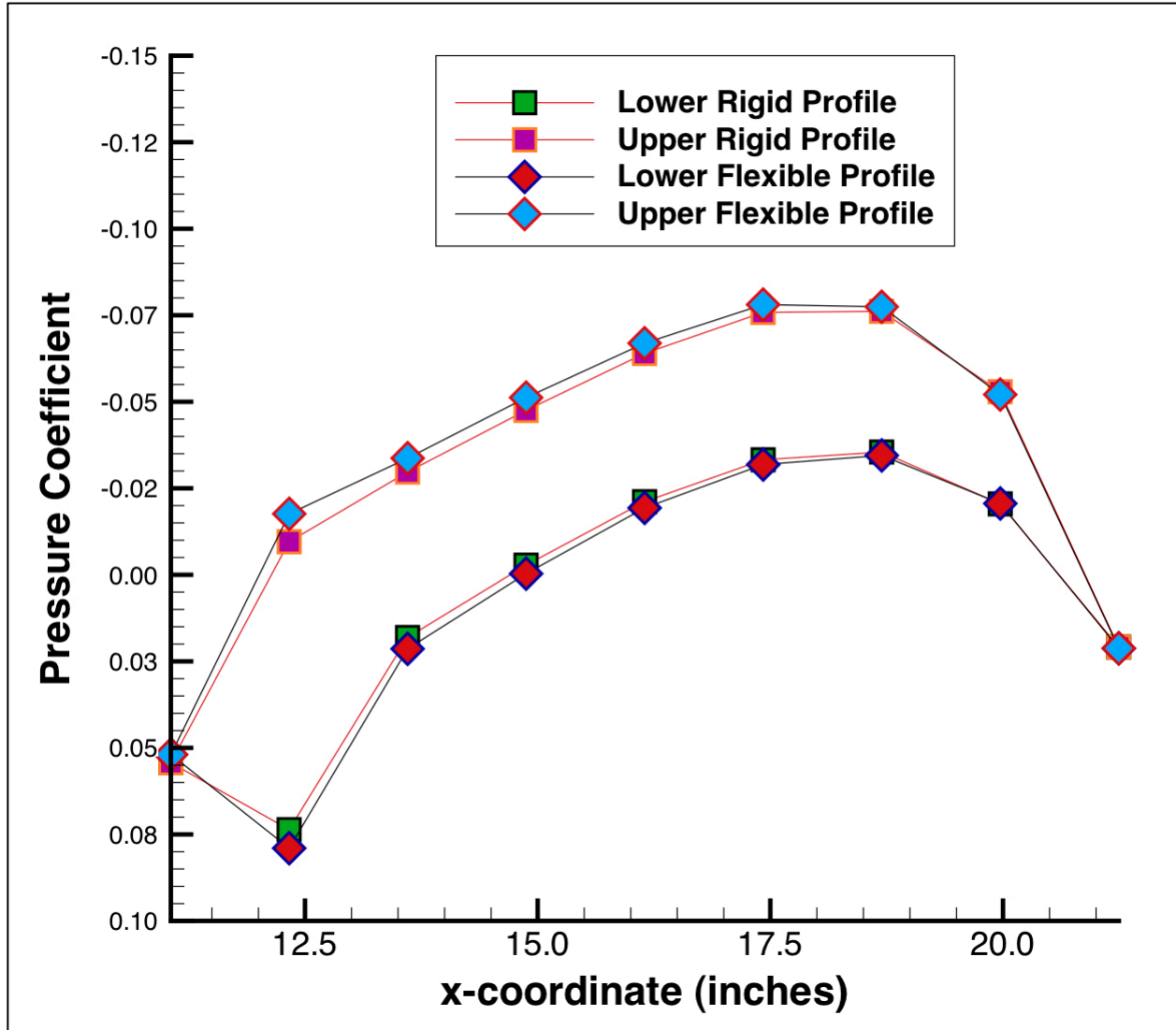
Figure 32. Plot for the comparison of pressure coefficient on the selected RCV profile at 7.47-in in *y*-position obtained by aerodynamic and aeroelastic calculations at a dynamic pressure of 90.0-psf using the Navier-Stokes equations.
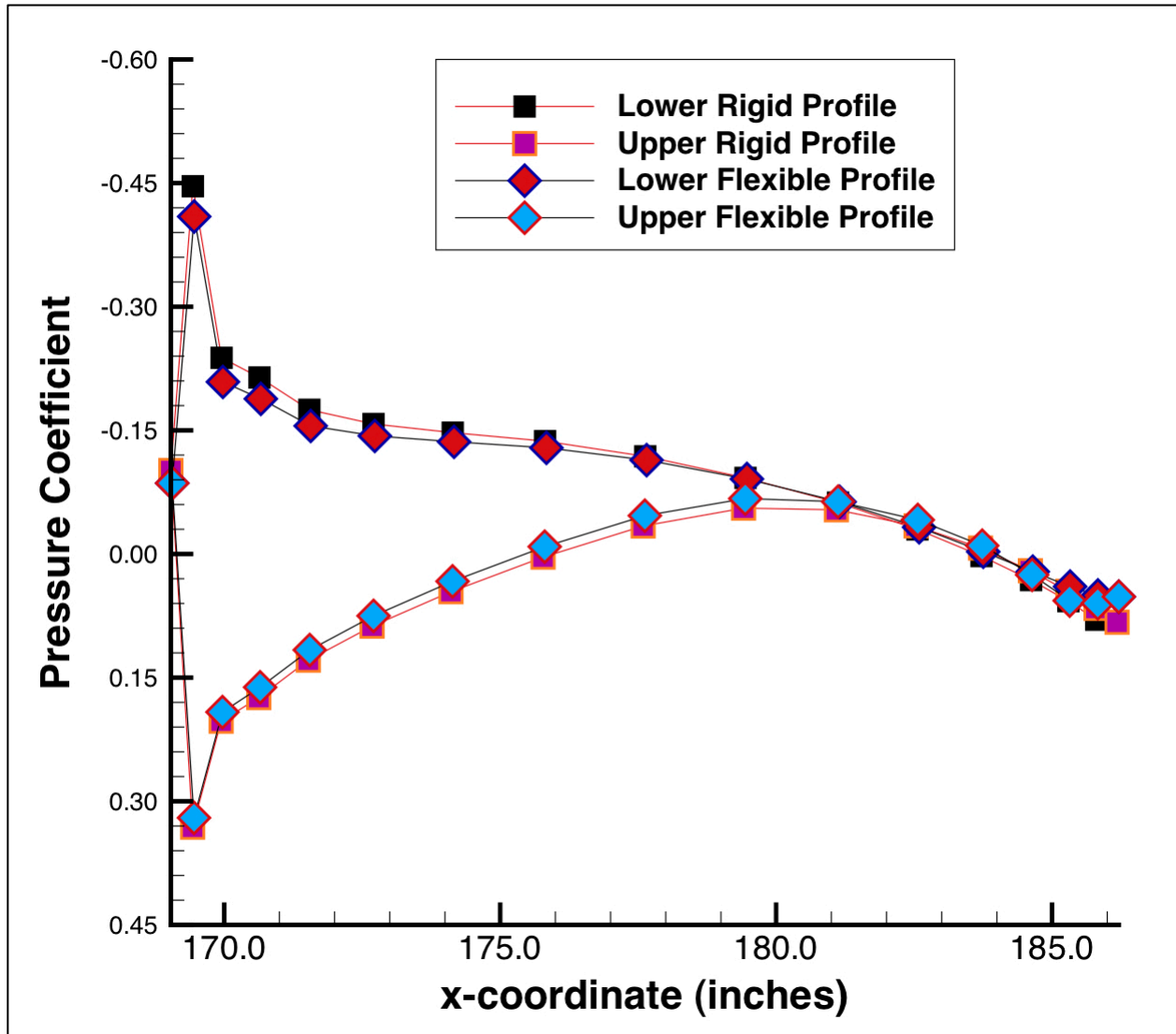
Figure 33. Plot for the comparison of pressure coefficient on the selected horizontal tail profile at 8.32-in
in *y*-position obtained by aerodynamic and aeroelastic calculations at a dynamic pressure of 90.0-psf
using the Navier-Stokes equations.
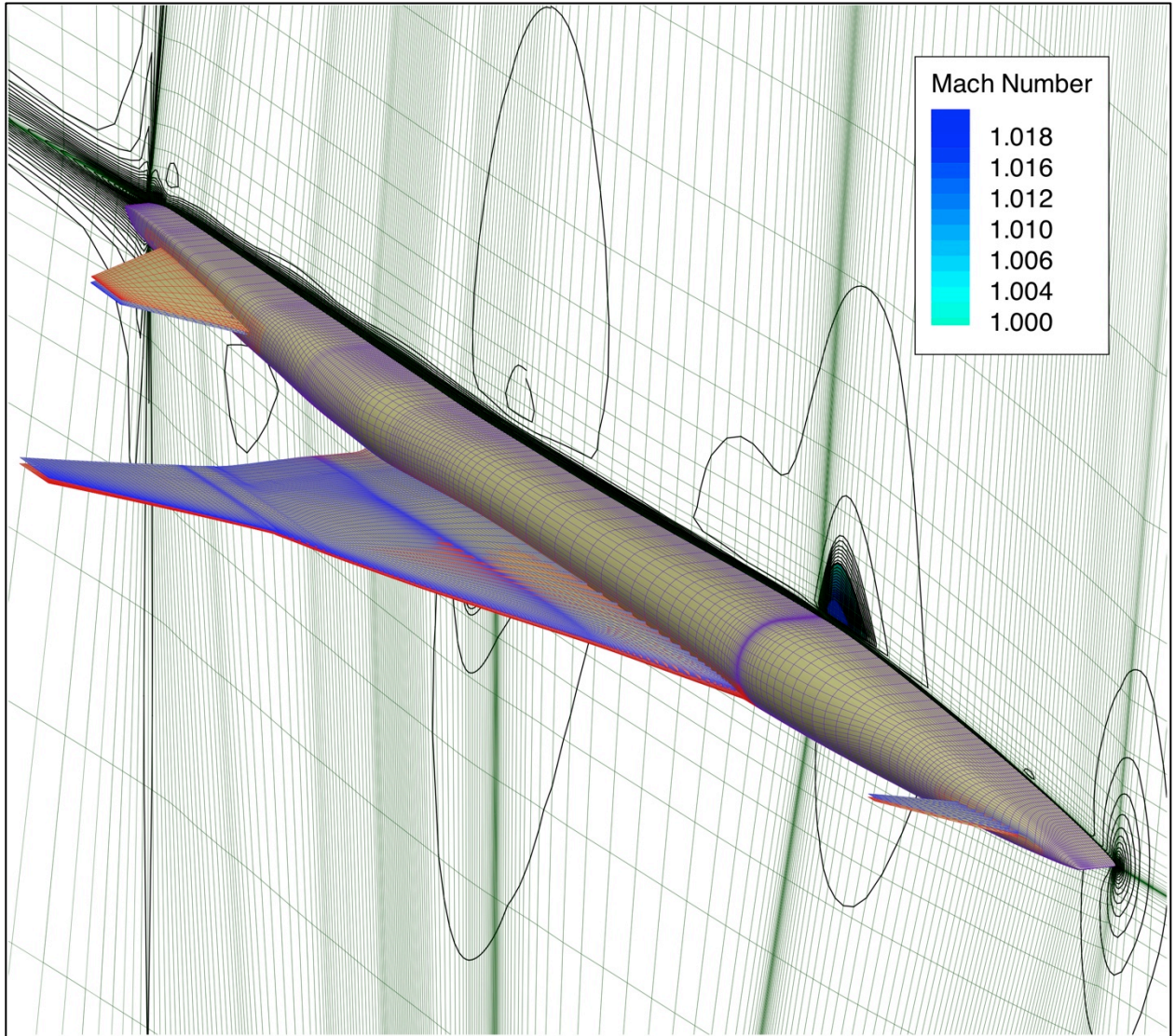
Figure 34. Configurations of the S[4]T wind tunnel model before/after deformation. The blue mesh lines are for the deformed shape. Mach number contour lines are shown at the symmetry plane, which was obtained by static aeroelastic calculations at a dynamic pressure of 150.0-psf using the Navier-Stokes equations.
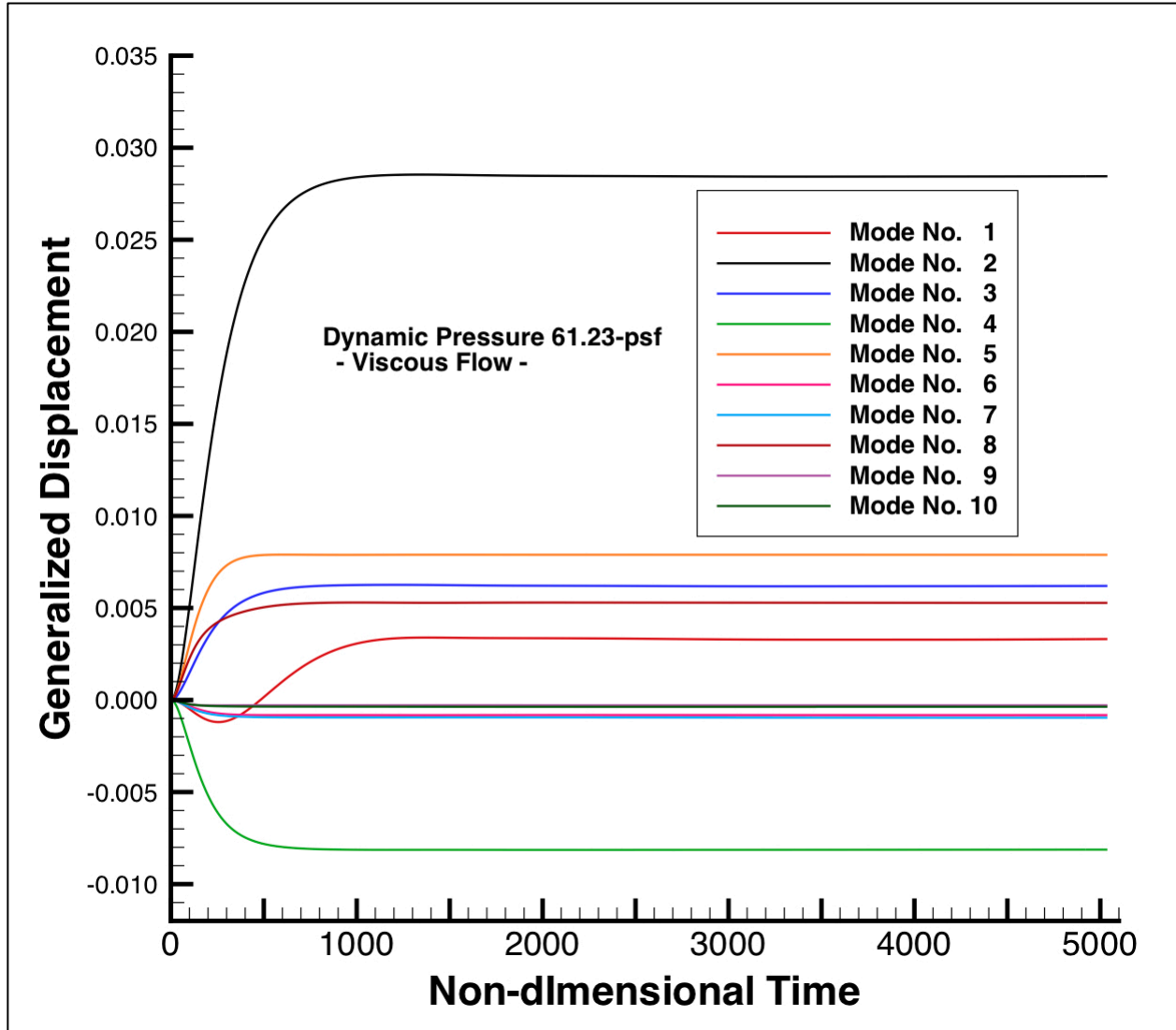
Figure 35. History of generalized displacements for the first ten modes. These results were obtained using the Navier-Stokes equations for aerodynamics at a dynamic pressure of 61.23-psf.

51
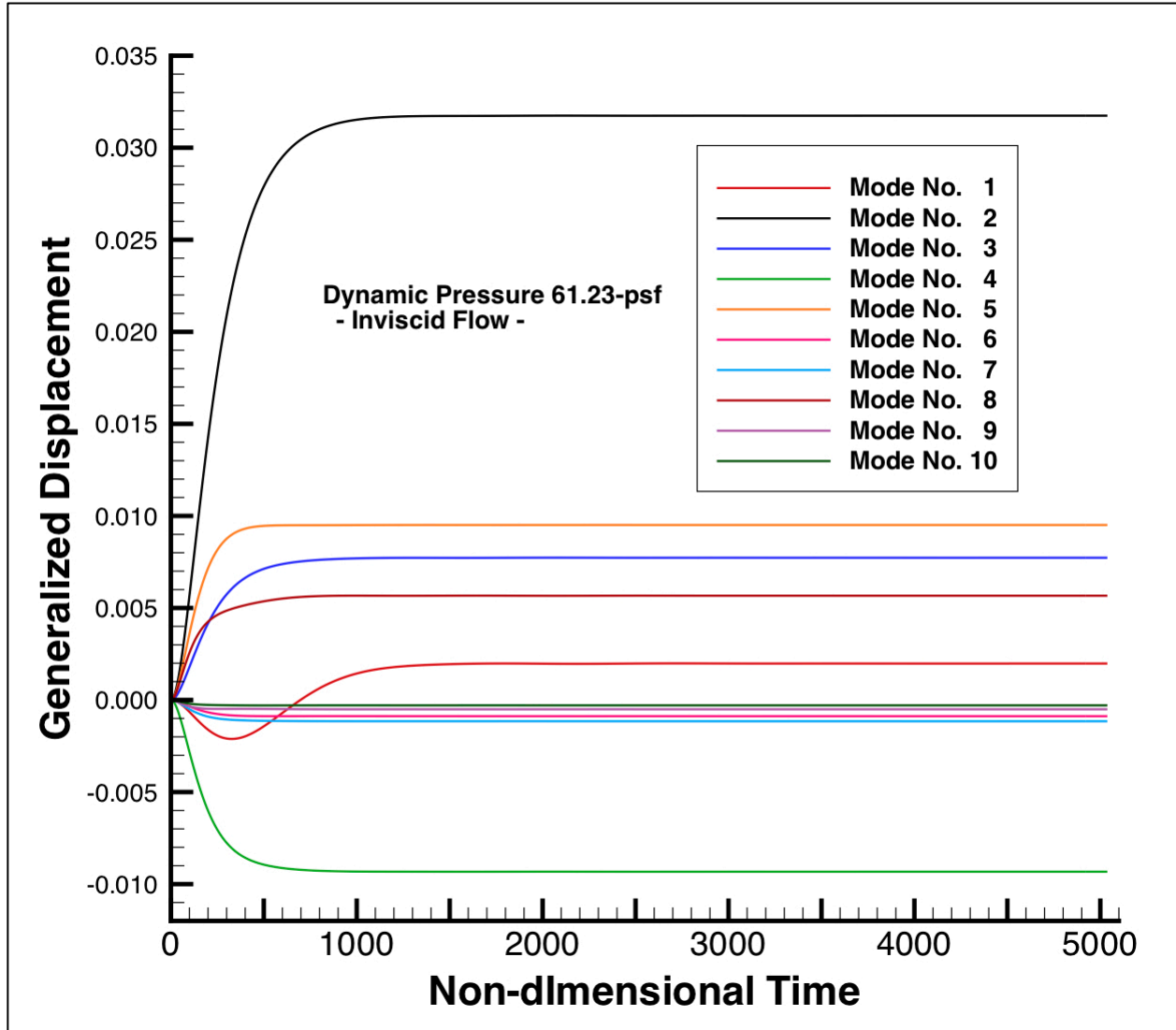
Figure 36. History of generalized displacements for the first ten modes. These results were obtained using the Euler equations for aerodynamics at a dynamic pressure of 61.23-psf.
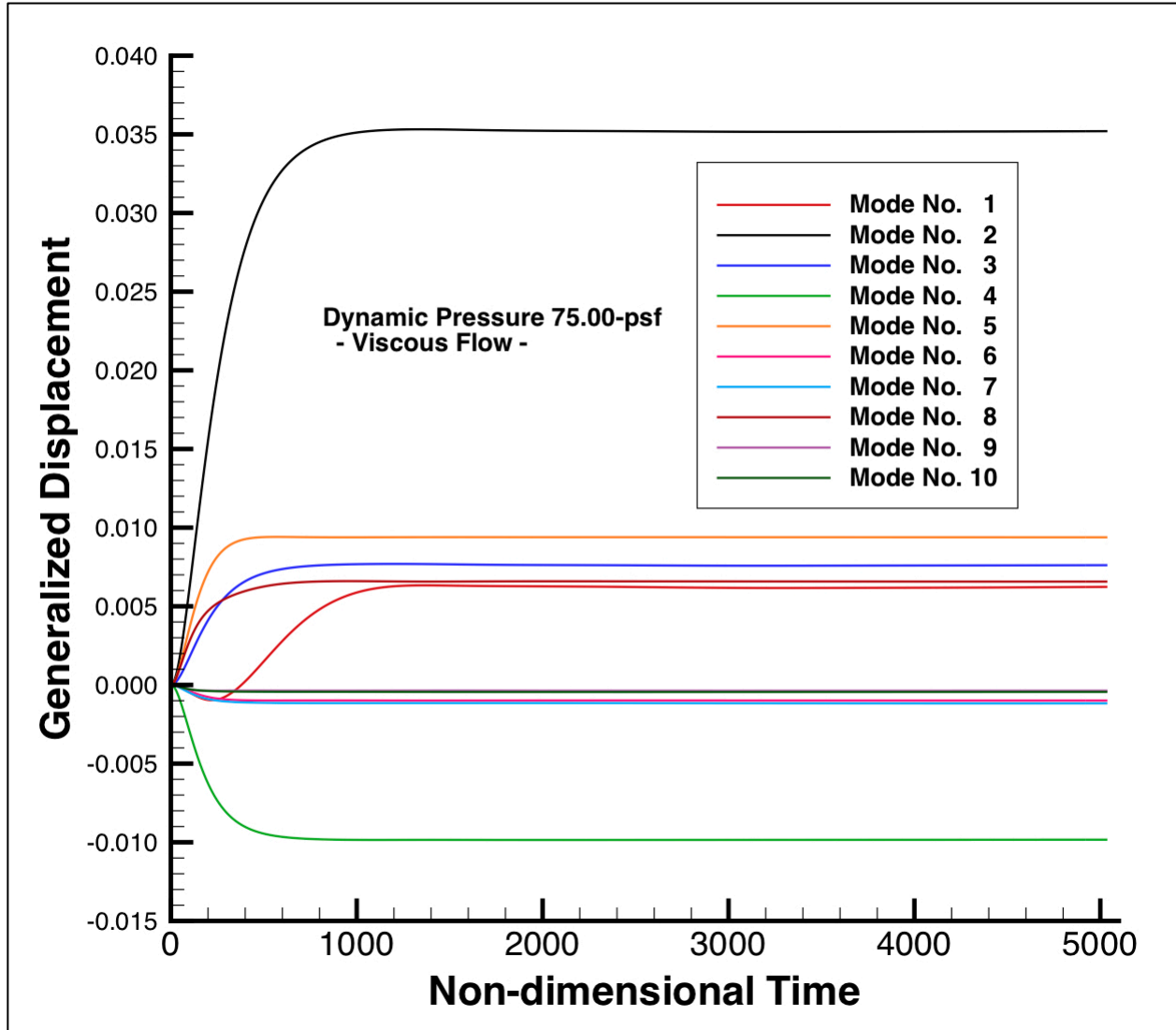
Figure 37. History of generalized displacements for the first ten modes. These results were obtained using the Navier-Stokes equations for aerodynamics at a dynamic pressure of 75.0-psf.
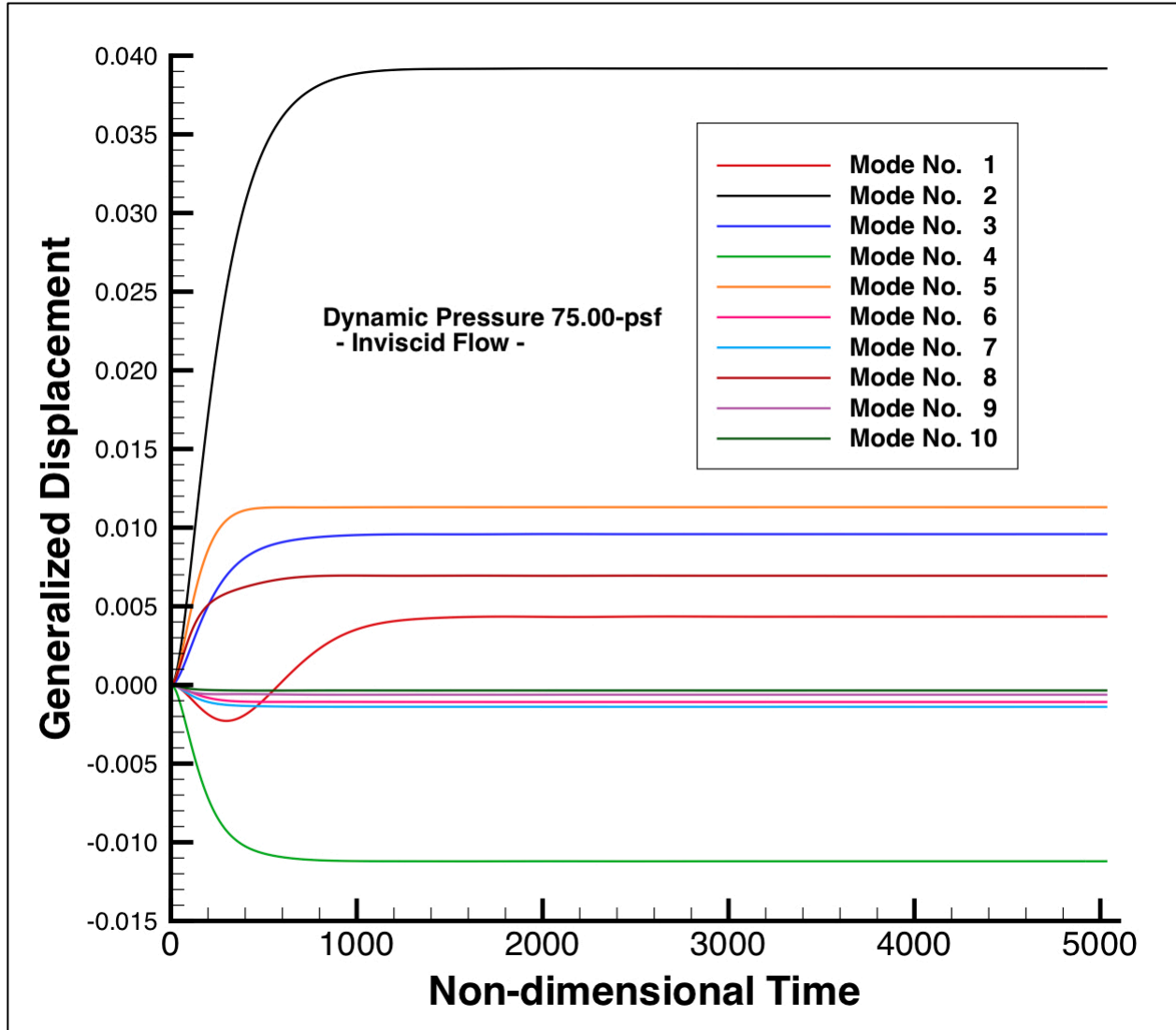
Figure 38. History of generalized displacements for the first ten modes. These results were obtained using the Euler equations for aerodynamics at a dynamic pressure of 75.0-psf.
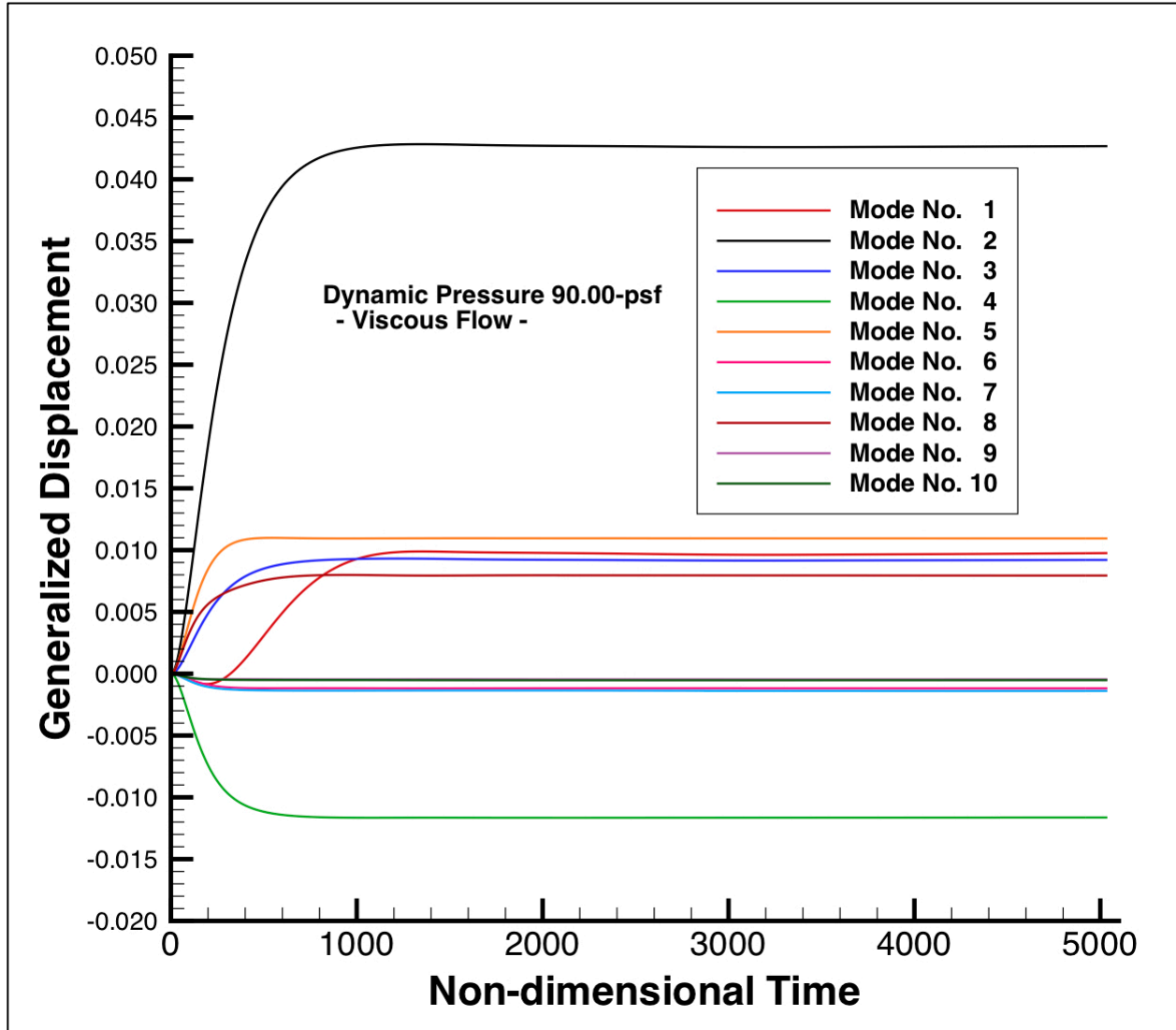
Figure 39. History of generalized displacements for the first ten modes. These results were obtained using the Navier-Stokes equations for aerodynamics at a dynamic pressure of 90.0-psf.

55
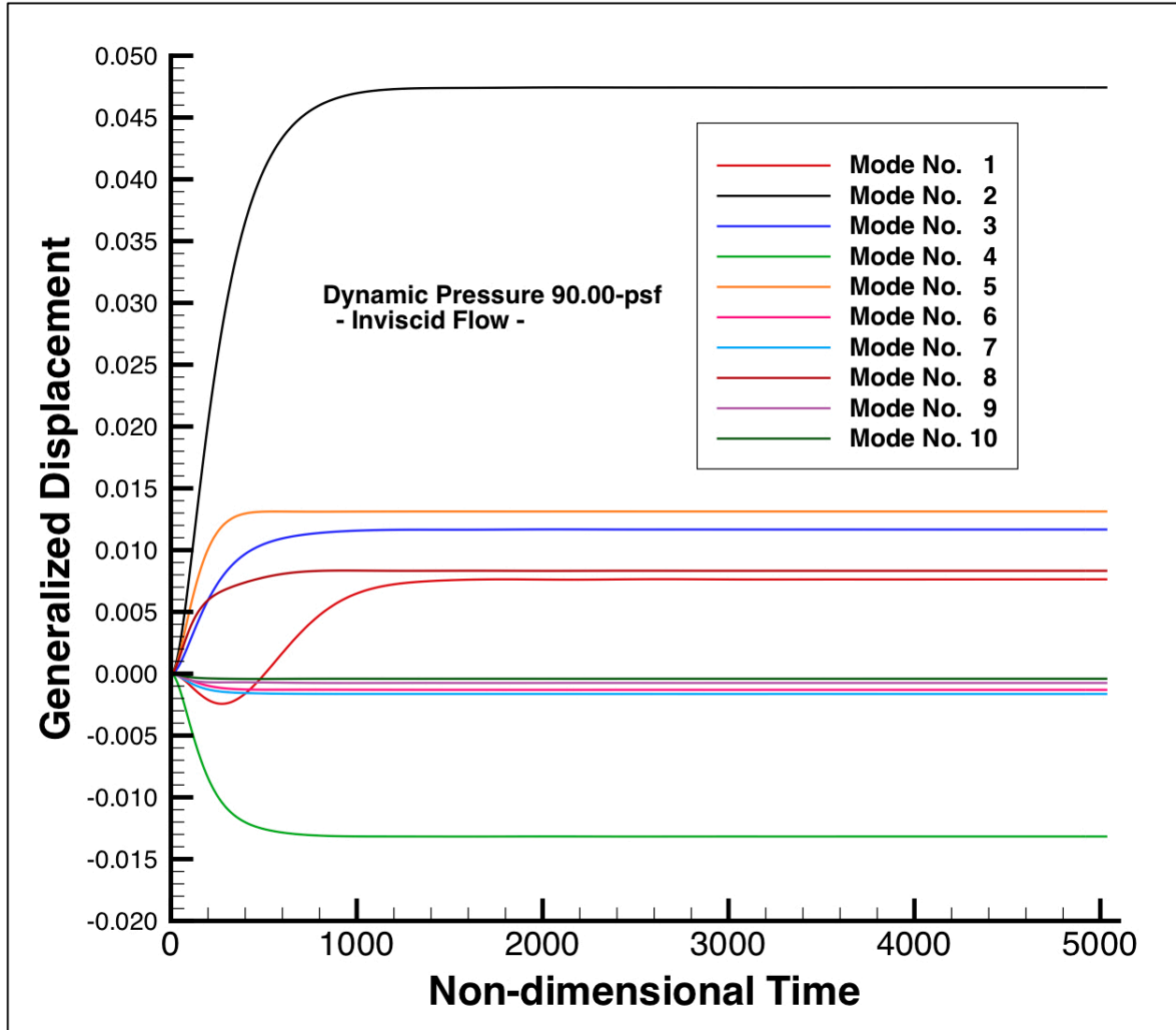
Figure 40. History of generalized displacements for the first ten modes. These results were obtained using the Euler equations for aerodynamics at a dynamic pressure of 90.0-psf.

56
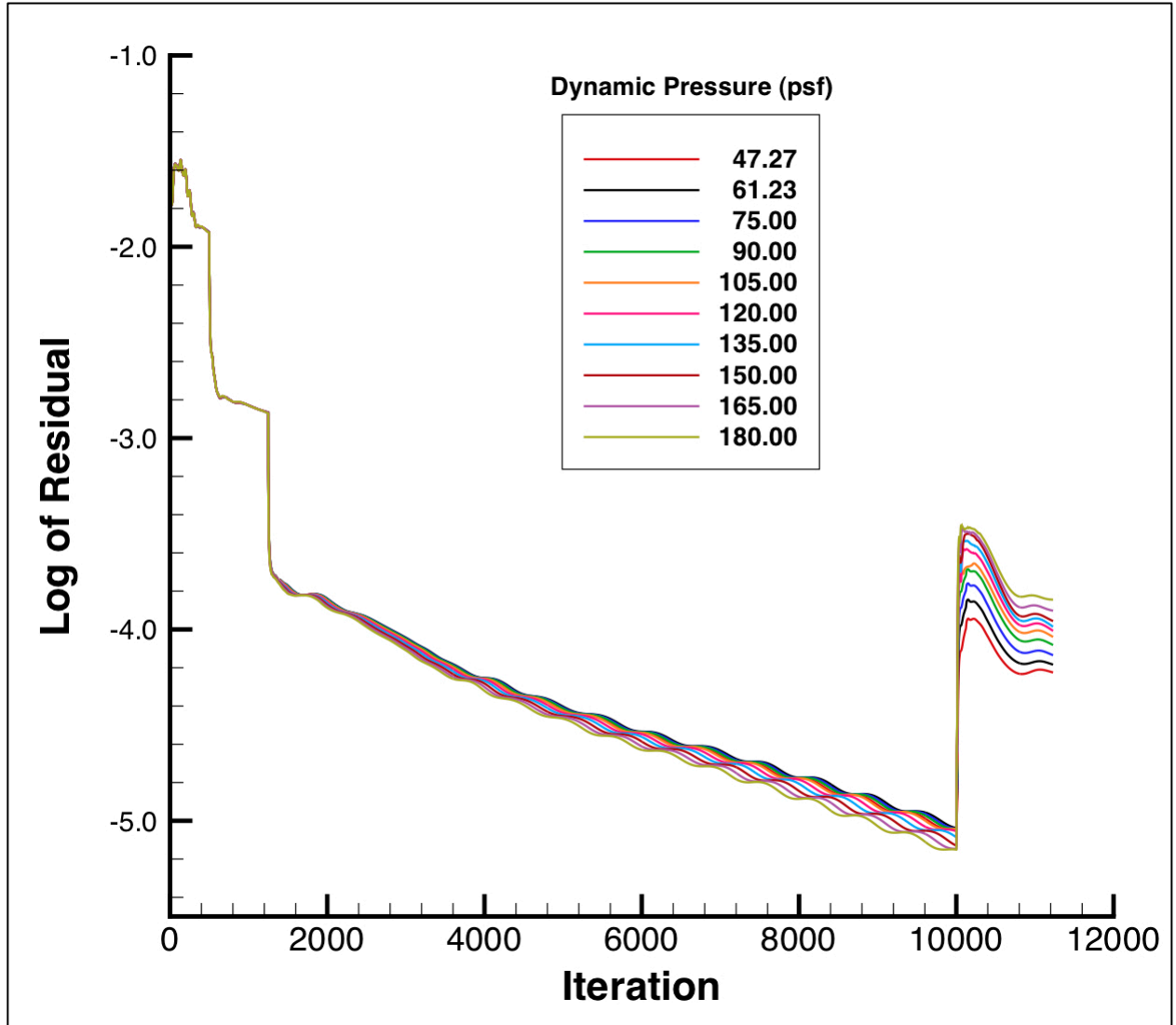
Figure 41. Residual histories at various dynamic pressures for static aeroelastic simulations using the Euler equations. The aeroelastic calculations were started from the rigid solutions at iteration no. 1001.
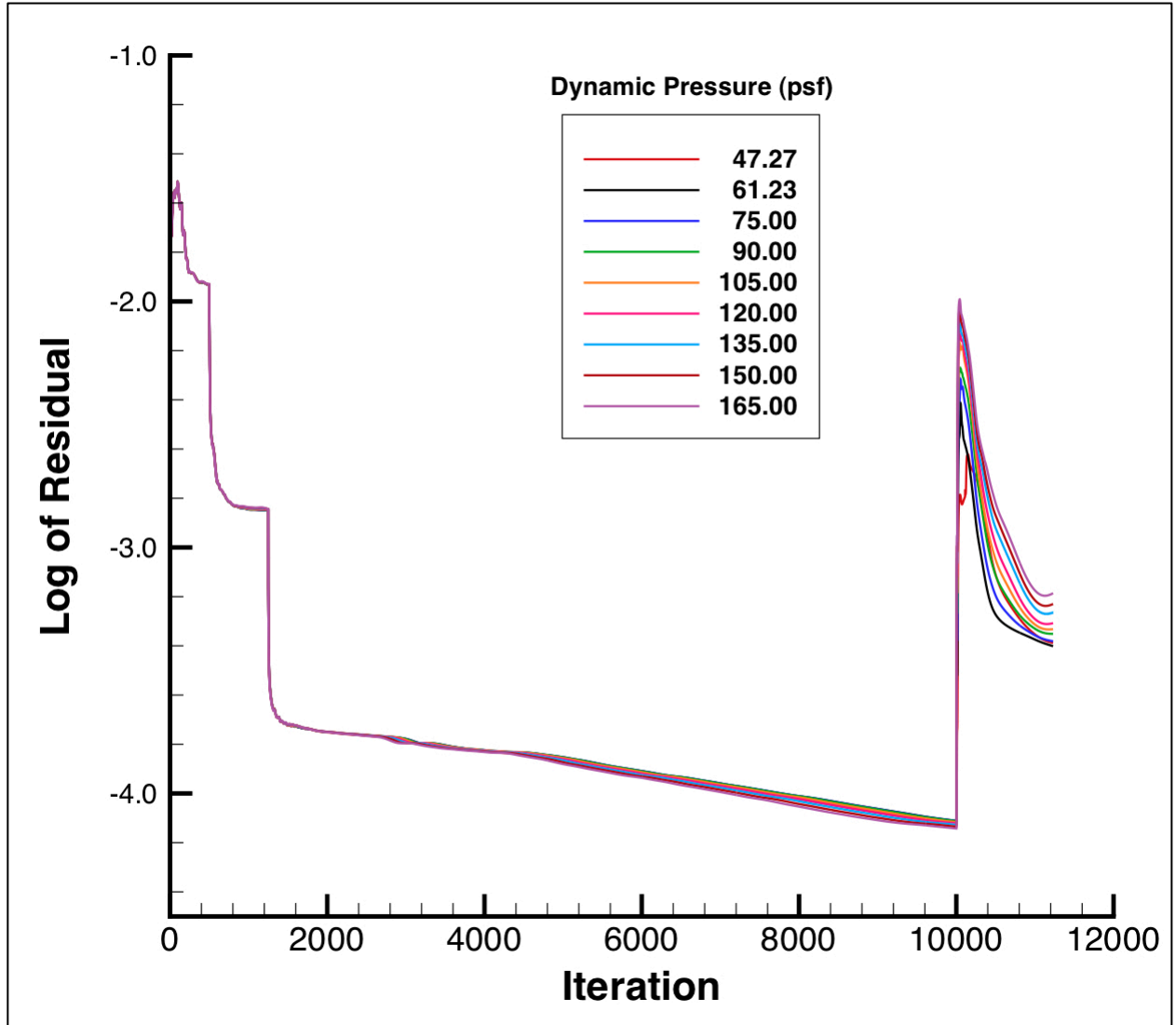
Figure 42. Residual histories at various dynamic pressures for static aeroelastic simulations using the Navier-Stokes equations. The aeroelastic calculations were started from the rigid solutions at iteration no. 1001.
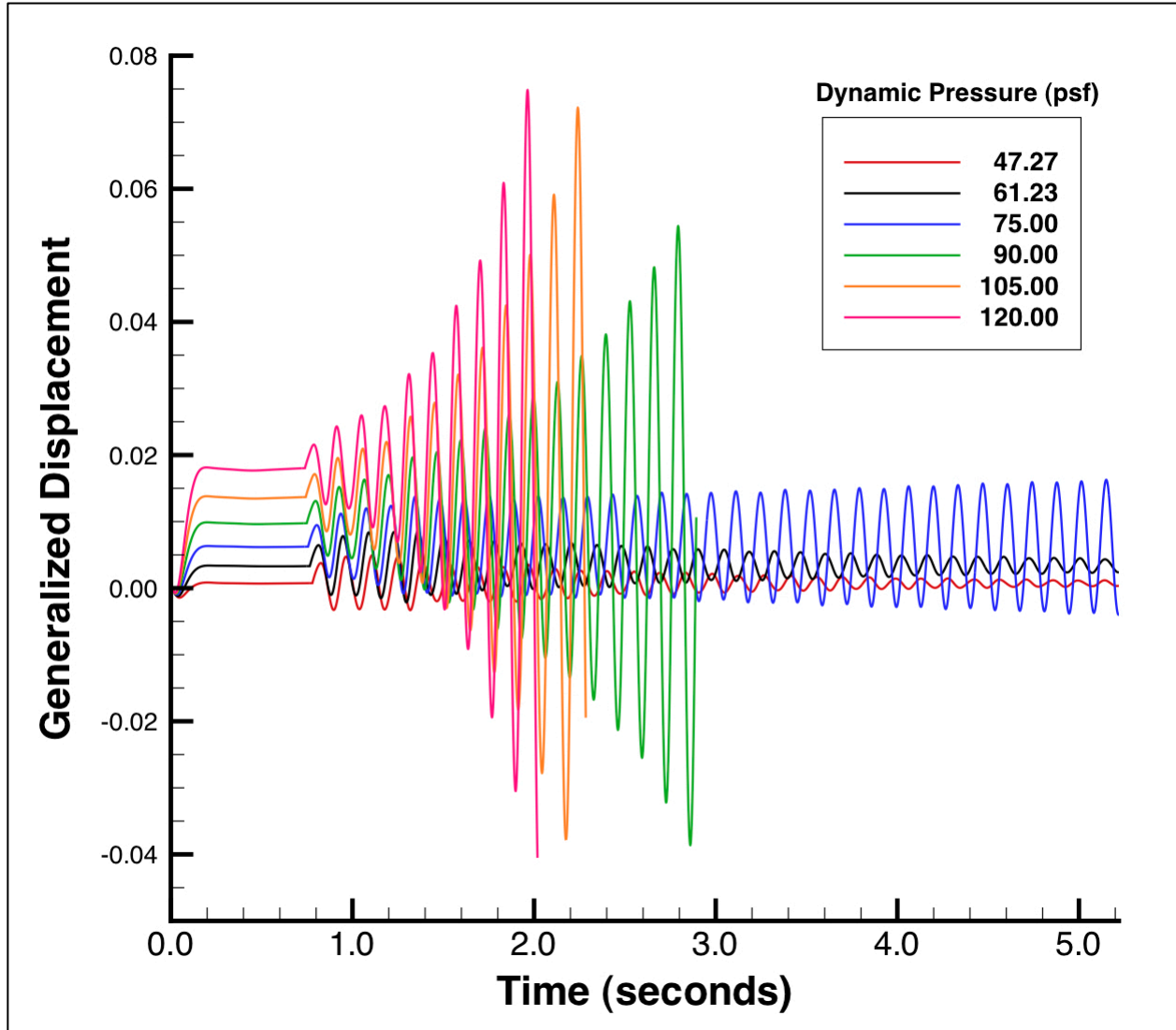
Figure 43. History of generalized displacements for the first mode at various dynamic pressures (47.27-120.0-psf), Mach 0.95 and a fixed 1.75° angle of attack. The results were obtained using the Navier-Stokes equations.
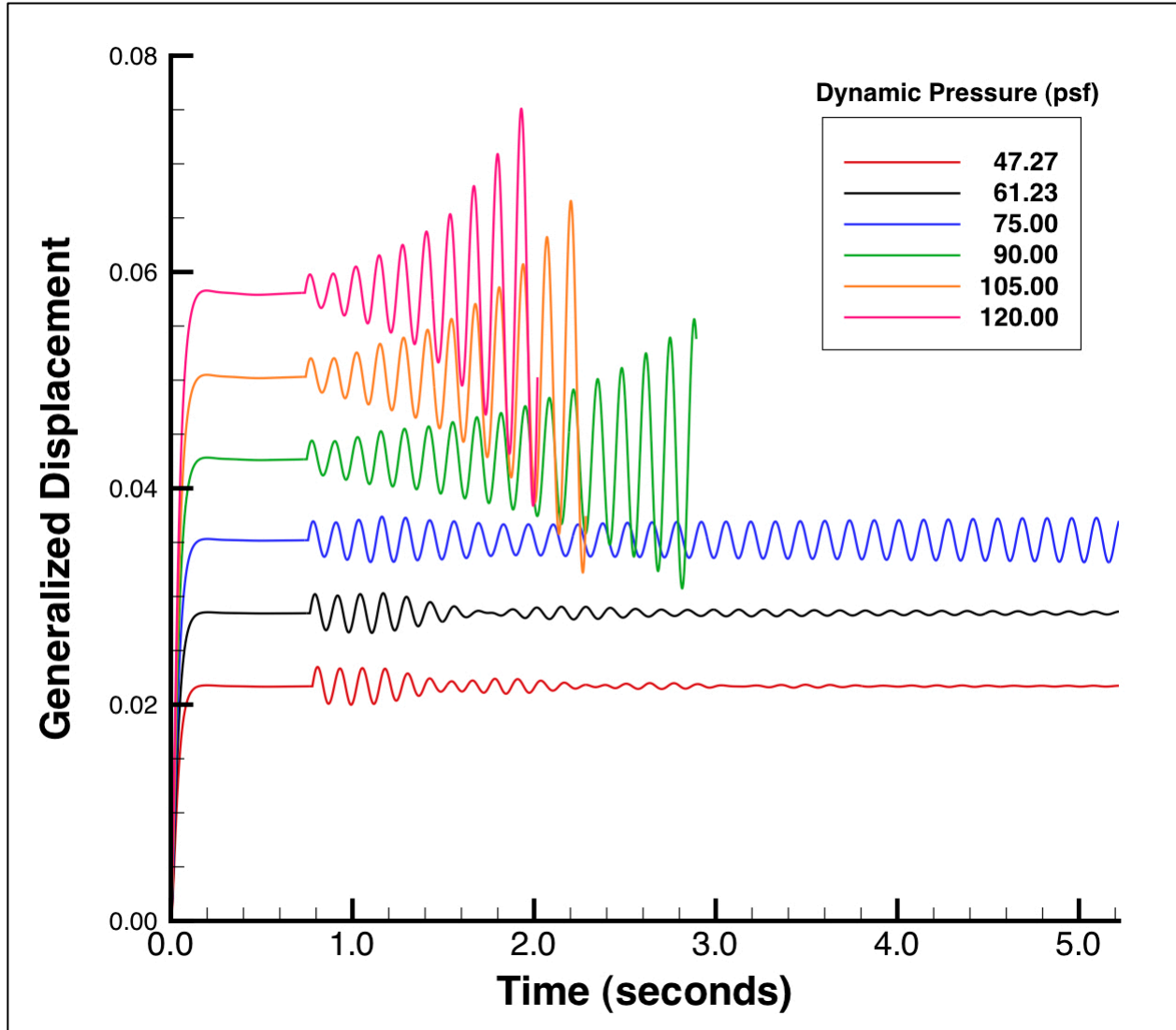
Figure 44. History of generalized displacements for the second mode at various dynamic pressures (47.27-120.0-psf), Mach 0.95 and a fixed 1.75° angle of attack. The results were obtained using the Navier-Stokes equations.
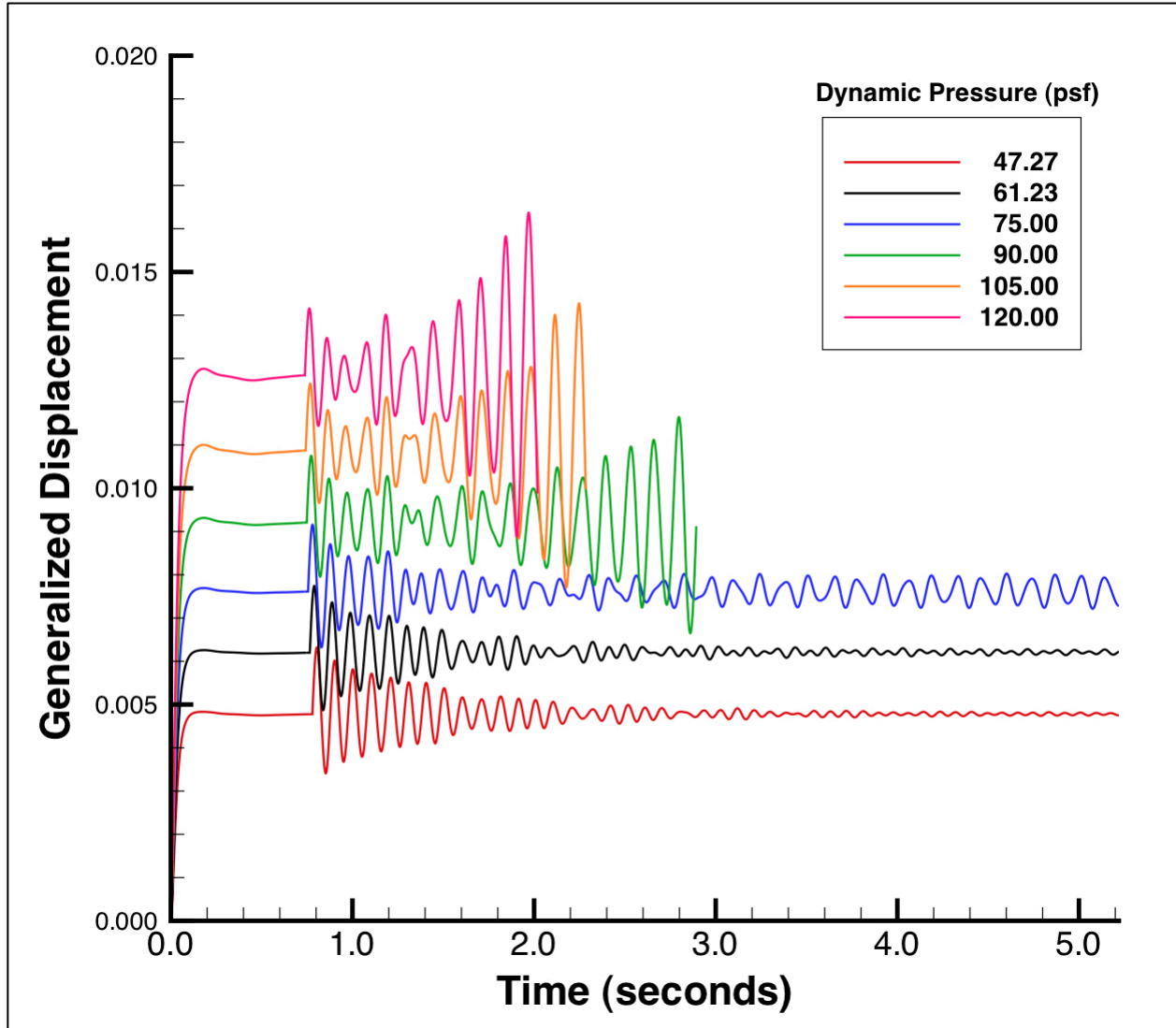
Figure 45. History of generalized displacements for the third mode at various dynamic pressures (47.27-120.0-psf), Mach 0.95 and a fixed 1.75° angle of attack. The results were obtained using the Navier-Stokes equations.
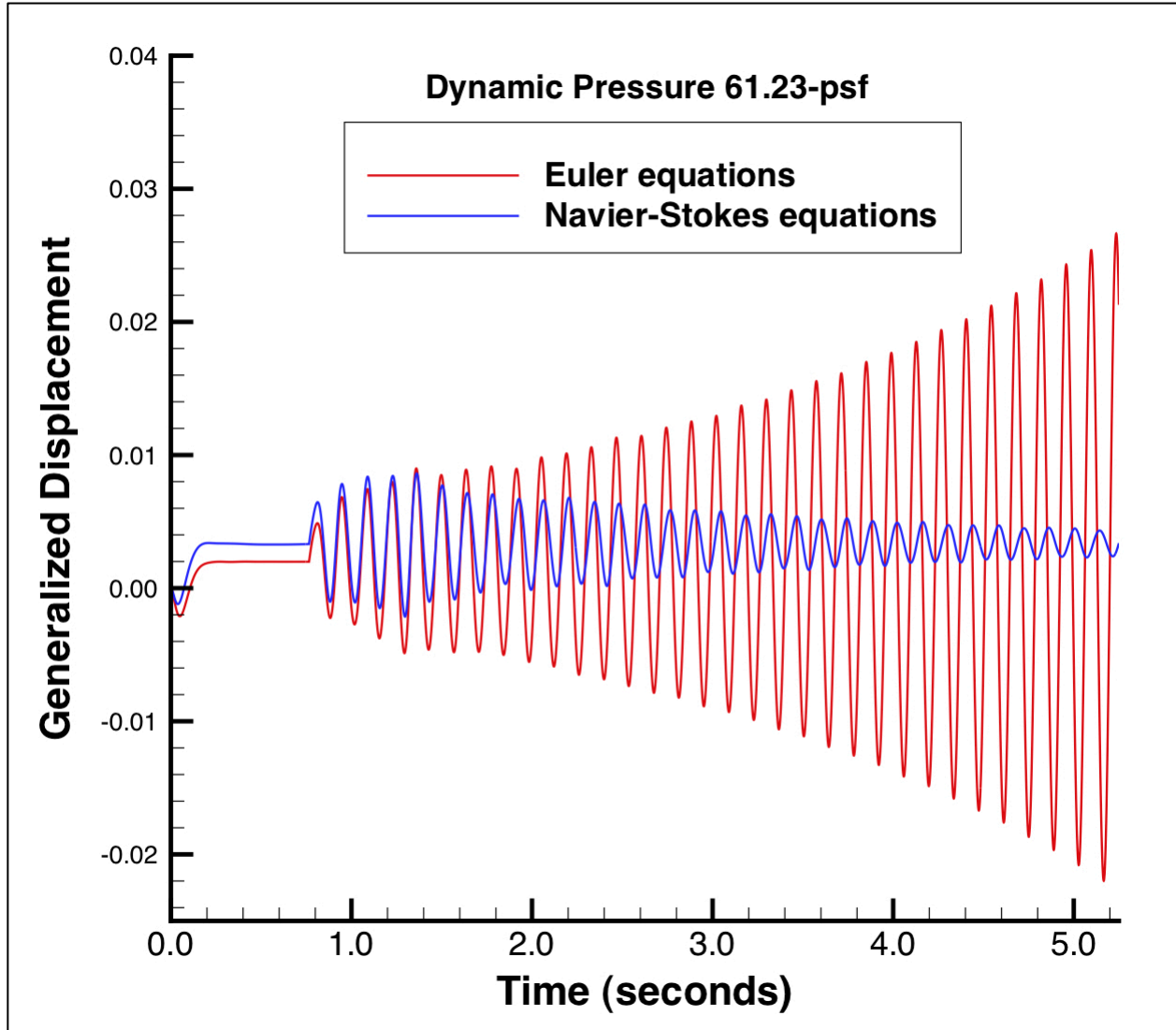
Figure 46. History of generalized displacements for the first mode at a dynamic pressure of 61.23-psf, Mach 0.95 and a fixed 1.75° angle of attack for both the Euler and Navier-Stokes simulations.
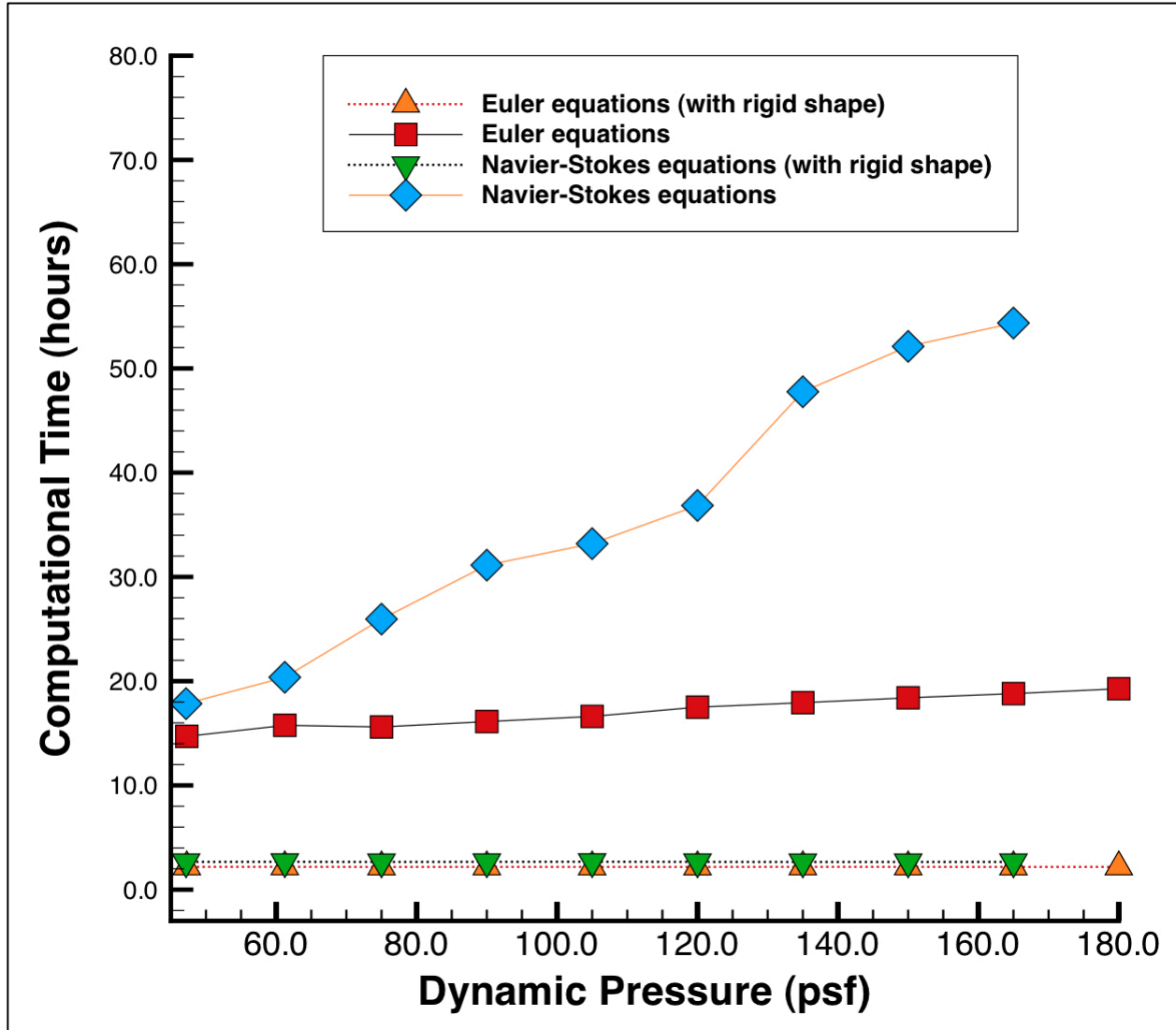
Figure 47. The comparison of computational performance in terms of wall-clock time usage for rigid and static aeroelastic simulations using both the Euler and Navier-Stokes equations.
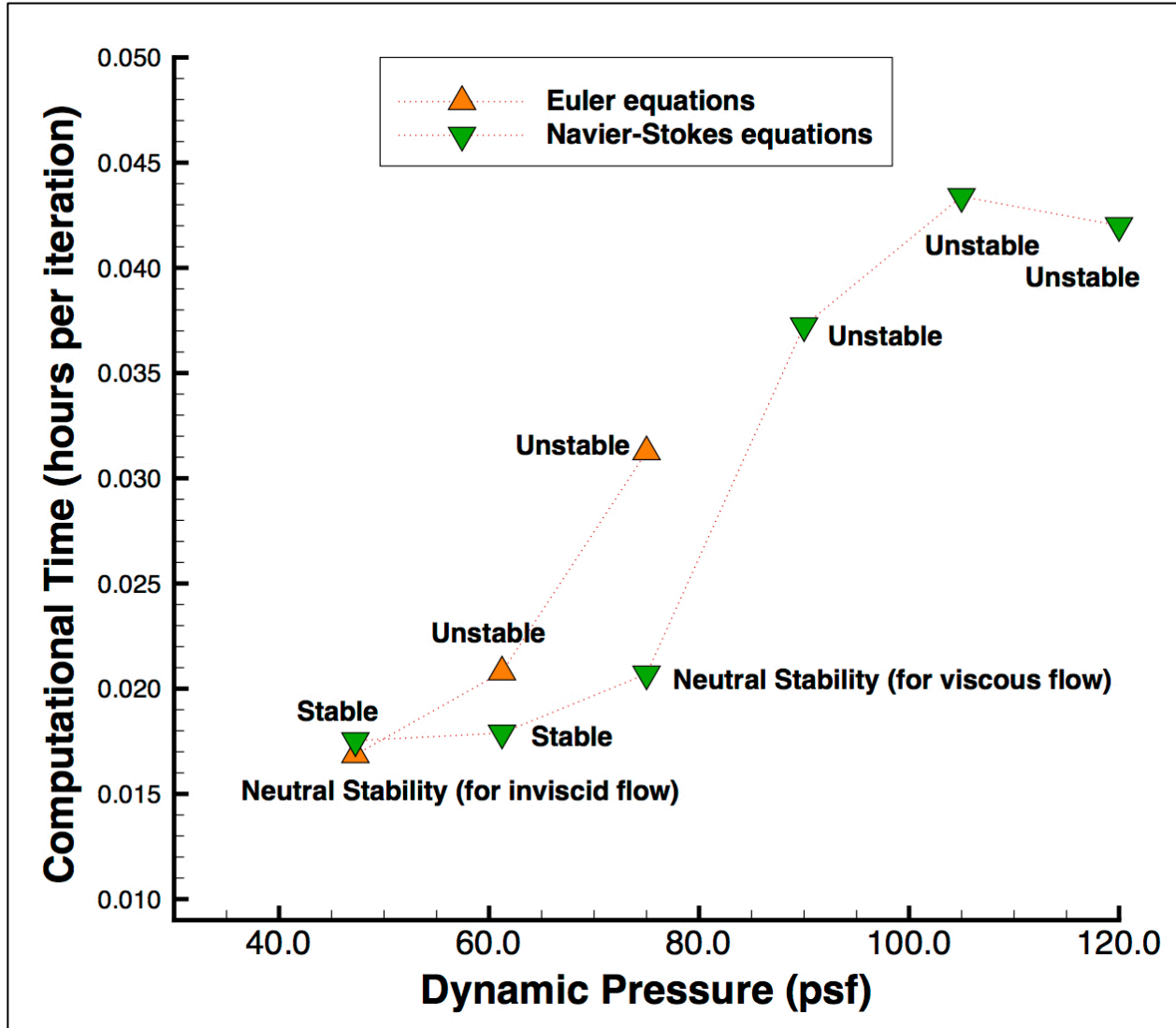
Figure 48. The comparison of computational performance in terms of wall-clock time usage for dynamic aeroelastic simulations using both the Euler and Navier-Stokes equations.

REPORT DOCUMENTATION PAGE

Form Approved
OMB No. 0704-0188

The public reporting burden for this collection of information is estimated to average 1 hour per response, including the time for reviewing instructions, searching existing data sources, gathering and maintaining the data needed, and completing and reviewing the collection of information. Send comments regarding this burden estimate or any other aspect of this collection of information, including suggestions for reducing this burden, to Department of Defense, Washington Headquarters Services, Directorate for Information Operations and Reports (0704-0188), 1215 Jefferson Davis Highway, Suite 1204, Arlington, VA 22202-4302. Respondents should be aware that notwithstanding any other provision of law, no person shall be subject to any penalty for failing to comply with a collection of information if it does not display a currently valid OMB control number.
PLEASE DO NOT RETURN YOUR FORM TO THE ABOVE ADDRESS.

1. REPORT DATE *(DD-MM-YYYY)*	2. REPORT TYPE	3. DATES COVERED *(From - To)*
01- 07 - 2014	Contractor Report	

4. TITLE AND SUBTITLE

Aeroelastic Analyses of the SemiSpan SuperSonic Transport (S4T) Wind Tunnel Model at Mach 0.95

5a. CONTRACT NUMBER

NNL12AA09C

5b. GRANT NUMBER

5c. PROGRAM ELEMENT NUMBER

6. AUTHOR(S)

Hur, Jiyoung

5d. PROJECT NUMBER

5e. TASK NUMBER

5f. WORK UNIT NUMBER

475122.02.07.07.01

7. PERFORMING ORGANIZATION NAME(S) AND ADDRESS(ES)

NASA Langley Research Center
Hampton, Virginia 23681

8. PERFORMING ORGANIZATION REPORT NUMBER

9. SPONSORING/MONITORING AGENCY NAME(S) AND ADDRESS(ES)

National Aeronautics and Space Administration
Washington, DC 20546-0001

10. SPONSOR/MONITOR'S ACRONYM(S)

NASA

11. SPONSOR/MONITOR'S REPORT NUMBER(S)

NASA/CR-2014-218287

12. DISTRIBUTION/AVAILABILITY STATEMENT

Unclassified - Unlimited
Subject Category 01
Availability: NASA CASI (443) 757-5802

13. SUPPLEMENTARY NOTES

Langley Technical Monitor: Walter A. Silva

14. ABSTRACT

Detailed aeroelastic analyses of the SemiSpan SuperSonic Transport (S4T) wind tunnel model at Mach 0.95 with a 1.75° fixed angle of attack are presented. First, a numerical procedure using the Computational Fluids Laboratory 3-Dimensional (CFL3D) Version 6.4 flow solver is investigated. The mesh update method for structured multi-block grids was successfully applied to the Navier-Stokes simulations. Second, the steady aerodynamic analyses with a rigid structure of the S4T wind tunnel model are reviewed in transonic flow. Third, the static analyses were performed for both the Euler and Navier-Stokes equations. Both the Euler and Navier-Stokes equations predicted a significant increase of lift forces, compared to the results from the rigid structure of the S4T wind-tunnel model, over various dynamic pressures. Finally, dynamic aeroelastic analyses were performed to investigate the flutter condition of the S4T wind tunnel model at the transonic Mach number. The condition of flutter was observed at a dynamic pressure of approximately 75.0-psf for the Navier-Stokes simulations. However, it was observed that the flutter condition occurred a dynamic pressure of approximately 47.27-psf for the Euler simulations. Also, the computational efficiency of the aeroelastic analyses for the S4T wind tunnel model has been assessed.

15. SUBJECT TERMS

Aeroelasticity; Dynamic pressure; Flutter; Grid deformation; Heavy gas; SemiSpan; SuperSonic

16. SECURITY CLASSIFICATION OF:			17. LIMITATION OF ABSTRACT	18. NUMBER OF PAGES	19a. NAME OF RESPONSIBLE PERSON
a. REPORT	b. ABSTRACT	c. THIS PAGE			STI Help Desk (email: help@sti.nasa.gov)
U	U	U	UU	69	19b. TELEPHONE NUMBER *(Include area code)* (443) 757-5802

Standard Form 298 (Rev. 8-98)
Prescribed by ANSI Std. Z39.18